Environment-Dependent Surface Dynamics of Supported Gold Nanoparticles Studied by High-Resolution Transmission Electron Microscopy

Liu, Pei

Publication date:
2017

Document Version
Publisher's PDF, also known as Version of record

Environment-Dependent Surface Dynamics of Supported Gold Nanoparticles Studied by High-Resolution Transmission Electron Microscopy

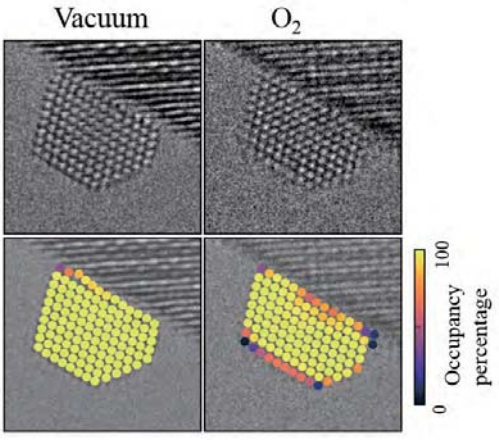

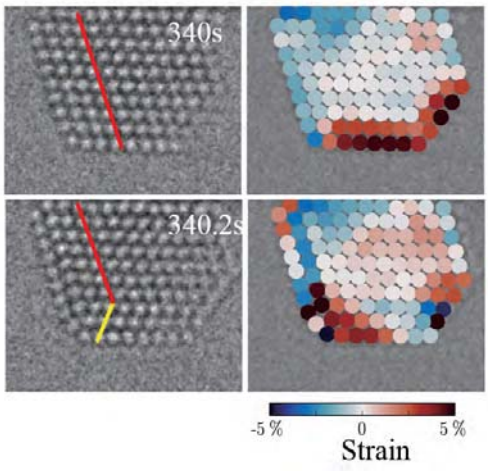

Pei Liu, October 2017

DTU Cen
Center for Elektronnanoskopi

Abstract

Nanostructured heterogeneous catalysts play an increasingly important role in contemporary society. Understanding their behavior under operational conditions has been the primary focus of many research groups over the past decades. This thesis presents time-resolved investigations of the dynamics of surfaces and interfaces of cerium dioxide supported gold nanoparticles under a variety of atmospheric conditions, at the atomic scale which is are of great importance to reveal the catalytic mechanisms. High-resolution transmission electron microscopy has the capability to image structures with sub-Ångstöm resolution and sub-second temporal resolution. Combined with environmental transmission electron microscopy, atomic surface dynamics such as column diffusion can be observed in the presence of gases.

The effect of the electron beam current on the surface dynamics of the sample has been evaluated by occupancy fluctuation of surface columns under a range of electron flux densities. The internal energy of the nanoparticles which most contributes to the kinetic energy of the diffusing atoms increases with both the electron flux density and the total time of exposure.

The surface and interface dynamics on the scale from sub-Ångström to nanometers on a model system of gold on cerium dioxide have been systematically investigated. Surface atom diffusion is observed under most conditions and normally reversible. Under some conditions the diffusing atoms on the surface move in a concerted manner, suggesting there is a variety of configurations which can be considered as local minima in potential energies in configurational space.

The relations between particles and substrate have been studied. Particle motion on the substrates are in three manners, such as rigid sliding, movement via mass transport and rigid rotation. Nanoparticles have two preferential crystallographic orientations with respect to the substrate, and they can transform between these two orientations under gas exposure.

Chemical environments and temperature influences the dynamics of supported nanoparticles. Firstly, the shape of the nanoparticle changes under exposure to different gases, and the surfaces are more active in oxygen than in hydrogen. Secondly, thermally activated layer appearance-disappearance fluctuations have been observed in different gases. In hydrogen and carbon monoxide the (100) facet fluctuates, while in oxygen the fluctuation is mainly on the (111) facet.

In the last part of the thesis, the reversibility and local strain field variation of the twinning-detwinning processes suggest twins play an important role in the catalytic reaction.

Resumé

Nanostrukturerede heterogene katalysatorer spiller en stadigt større rolle I vores samfund. Gennem de seneste årtier har mange international forskningsgrupper haft det som mål at opnå en dybere forståelse af deres opførsel under reaktive betingelser. I denne afhandling vises tidsopløste undersøgelser på atomar skala af nanopartiklers overfladedynamik samt dynamikken i grænselaget mellem nanopartikel og bærermateriale for guld på ceriumdioxid under varierende omgivelser som er af stor vigtighed for at bestemme katalytiske mekanismer. Med højt-opløst transmissionselektronmikroskopi kan man undersøge materialer med sub-Ångström og sub-sekund opløsning. Når teknikken kombineres med muligheden for at have gasser omkring prøven (environmental tranmission electron microscopy, ETEM) kan atomar dynamik så som kolonnediffusion observeres under gaseksponering.

Elektronstrålens effekt på prøven er blevet evalueret ved at undersøge befolkningen af overfladekolonner under forskellige belysningstætheder. Den interne energi af nanopartiklerne som er hovedbidraget til de diffunderende kolonners kinetiske energi stiger både med elektron tæthed og eksponeringstid.

Dynamikken af overflader og grænseflader i en guld/ceriumdioxid prøve er systematisk undersøgt på en skala fra sub-Ångstöm til nanometer. Reversibel overfladediffusion blev observeret under de fleste betingelser. Under visse betingelser diffunderede flere kolonner samlet hvilket antyder at der er et antal konfigurationer som kan antages at minimere den potentielle energi.

Forholdet mellem nanopartikler og bærermateriale er blevet undersøgt. Partikelbevægelser er blevet inddelt i tre kategorier kaldet rigid sliding, movement via mass transport og rigid rotation. Nanopartikler har to foretrukkende krystallografiske orienteringer i forhold til bærermaterialet og kan transformere mellem disse under gaseksponering.

De kemiske omgivelser og temperaturen influerer dynamikken af nanopartikler. Først og fremmest ændrer formen af partiklerne sig som funktion af den omgivende gas, desuden er overfladerne mere dynamiske i oxygen end under hydrogen. Dernæst blev det observeret at hele atomare lag fluktuerede i forskellige gasser. I hydrogen og carbon monoxid var det hovedsageligt på (100) facettermens det var på (111) facetter i oxygenatmosfære.

I den sidste del af afhandlingen undersøges reversibel variation af strain-fields og fluktuationer af krystaltvillingeplan. Dette antyder at krystaltvillingerplaner spiller en betydelig rolle for katalytiske reaktioner.

Preface

This thesis is submitted in the candidacy of the PhD degree from the Technical University of Denmark (DTU). The work was carried out at the Center for Electron Nanoscopy (CEN) from November 2014 to November 2017. The thesis is part of the project Dyncat under the co-supervision of Senior Researcher Thomas Willum Hansen (DTU-Danchip/Cen), Professor Jakob Birkedal Wagner (DTU-Danchip/Cen) and Professor Jakob Schøtz (DTU-Physics).

Based on this work, several scientific papers are in preparation:

Liu, P., Madsen, J., Wagner, J. B., Hansen, T. W. & Schiøz, J. Surface atom diffusion on Au nanoparticles by time-resolved HRTEM. In preparation. The content comes from chapter 3 and section 4.1.2 of the thesis.

Liu, P., Madsen, J., Wagner, J. B., Hansen, T. W. & Schiøz, J. Rigid-body motion of supported Au nanoparticles at atomic scale. In preparation. The content comes from section 4.3 of the thesis.

Liu, P., Madsen, J., Wagner, J. B., Hansen, T. W. & Schiøz, J. Gas induced crystallite transformation of supported Au nanoparticles In preparation. The content comes from section 4.4 of the thesis.

Liu, P., Madsen, J., Wagner, J. B., Hansen, T. W. & Schiøz, J. Quantitative measurement of gas induced surface atom diffusion of supported Au nanoparticles. In preparation. The content comes from section 5.1 and section 5.2 of the thesis.

Liu, P., Madsen, J., Wagner, J. B., Hansen, T. W. & Schiøz, J. Dynamical twinning of suppoprted Au nanoparticles. In preparation. The content comes from section 5.4 of the thesis.

Acknowledgement

First and foremost, I would like to express my sincere gratitude to my supervisors: Senior Researcher Thomas Willum Hansen, Professor Jakob Birkedal Wagner and Professor Jakob Schiøtz, for their invaluable and constant support during the past three years. They have been a great team guiding both the experimental and theoretical work perfectly and keeping the project on the right track. Thank you for having kept your doors open at all the time, and for insightful and stimulating discussions. I truly feel privileged to have you as mentors.

A special thanks goes to Jacob Madsen in the DynCat project. He is enthusiastic and energetic in programming and calculations which contribute to the analysis of experimental data for the further understanding of surface dynamics. I has been glad for all the moments and events we went through together.

I am grateful to Dr. Agata Gallas-Hulin for providing the chemical prepared samples from the beginning of this project. I also thank her for teaching me to prepare supported catalytic nanoparticles using the deposition precipitation method and the incipient wetness impregnation method.

A special thanks to Dr. Evgeniy Shkondin for helping deposit TiO_2 oxide on the DENSsolution chips using atomic layer deposition.

Tiantian Wu from DTU Energy Conversion and Storage who conducted DFT calculations of the potential energy of Au/CeO_2 system. I thank her for the in-depth discussions and great collaboration.

My appreciation goes to Dr. Marc Heggen, Dr. XianKui Wei and Dr. Paul Paciok, for their help when I carried out the external research in Jülich. It was fantastic to work on the state-of-art microscopes and to have the opportunity to discuss with the microscopists at the Ernst Ruska center.

My sincere thanks also goes to all the members at CEN. Thank you for the great time we have been together. Special thanks to Senior Researcher Andrew Burrows, Senior Researcher Takashi Kasama and Dr. Lili Zhang for your academic support and valuable input for this project. Thank you!

Last but not the least, the greatest thanks to my family for all your love, encouragement and continuous support. I dedicate this thesis to you.

Pei Liu, October 2017

Contents

ACRONYMS

ALD	Atomic layer deposition
ASE	Atomic simulation environment
CTF	Contrast transfer function
CNN	Convolutional neural networks
DFT	Density functional theory
FFT	Fast Fourier transform
Fps	frames per second
Fcc	Face center cubic
HRTEM	High-resolution transmission electron microscopy
SNR	Signal to noise ratio
TEM	Transmission electron microscopy
TMP	Turbomolecular pump
IP	Incipient wetness impregnation method
DP	Deposition precipitation method
NPs	nanoparticles
GNPs	gold nanoparticles
TPD	Temperature programmed desorption
HVAC	High vacuum condition
PSF	Point spread function

Chapter 1 Introduction

1.1 Introduction to heterogeneous catalysis

A catalyst is a substance that enhances the rate of a chemical reaction. The catalyst interacts with the reactants in a cyclic manner promoting the reaction at an atomic or molecular level, but itself is not consumed. Catalysts are referred to as heterogeneous if the reactants and catalyst are in different phases and homogeneous if they are in the same phase.

Heterogeneous catalysis for the oxidation of various chemical compounds is one of the core technologies in the contemporary chemical industry. Harmful substances, such as volatile organic compounds and carbon monoxide, can be generated from vehicles and industrial sources due to the incomplete combustion of fossil fuels. These compounds should be converted into non-toxic CO_2 and H_2O before they are emitted into the air. Due to its technological importance and fundamental interest, CO oxidation has been wildly investigated in the fields of surface science and heterogeneous catalysis

Gold had long been considered to be catalytically inactive before Haruta[1] et al., Baiker[2] et al., and Vannice[3] et al. found that it is very active for the low-temperature oxidation of CO, although the metal or the support alone do not show any pronounced activity. The oxidation of carbon monoxide on Au is a bimolecular process that is straightforward to understand and is a system that has been investigated for decades. However, a detailed understanding of dynamic catalyst processes at the molecular level is still lacking, largely due to the level of complexity inherent in these processes.

The role of the catalyst is shown schematically in Figure 1.1. Here we use the oxidation of carbon monoxide (CO) to carbon dioxide (CO_2) as a model reaction. Dioxygen and carbon monoxide react to form carbon dioxide. The gas phase reaction is associated with a higher energy barrier, which is significantly decreased if the reaction occurs on the surface of a catalyst. Both reactant molecules are chemically adsorbed on the catalyst surface. The interaction between the adsorbates and catalyst weaken the intramolecular bonding strength and lower the reaction barrier to produce CO_2. In the final step, the product, CO_2, leaves the catalyst surface.

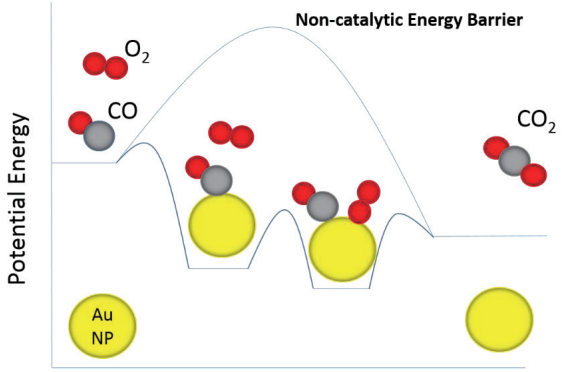

Figure 1.1 Potential energy diagram of CO oxidation reaction.

The most widely used theoretical model to explain bond formation and trends in reactivity between adsorbate and metal surfaces is the d-band theory[4]. For example, if one sweeps through the transition metals in the periodic table, the electronic structure differences between these elements are the energies of the d states, since they all have broad half-filled, s bands[4,5]. The interaction between adsorbate and these transition metals is mainly electron coupling between the valence state of the adsorbate and d states of the metal, and as a result, bonding and antibonding states are formed. The higher the d states are in energy (the center of the d band relative to the Fermi level), the higher in energy the antibonding states are and the stronger the bond between adsorbate and the metal. The correlation between interaction energy and d-band center has been found[6] both for adsorption energies and transition-state energies. Due to the same electronic structure properties of a specific structure, the correlation between adsorption energies and transition-state energies has also been established[5]. Therefore, the d-band center is an excellent descriptor to describe catalytic activity and selectivity.

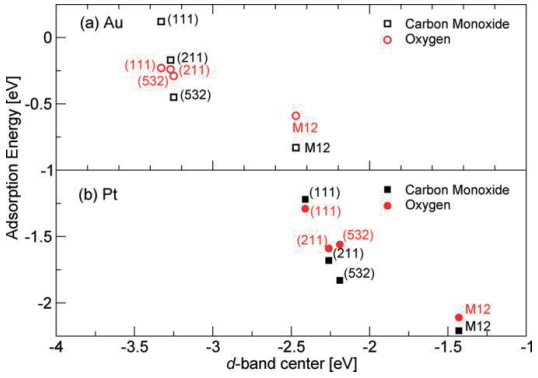

Figure 1.2 Adsorption energy E_{co} and E_o versus d-band center for (111) surfaces, (211) surfaces, (532) surfaces and M12 clusters of (a) Au (open black square, open red circle) and (b) Pt (solid black square, solid red circle). Reproduced from[7].

The d-band center varies depending not only on the element (varying d states filling degree with fixed width) but also on the local structure of the system (varying d states width by alloy, coordination number)[7]. The coordination number significantly influences the width of the d-band, shifting the d states further up or down to compensate for width variations. Figure 1.2 shows that the d-band center varies with metal coordination number and that binding energies shift accordingly for different surface structures. A simple rule of thumb for the adsorption energy dependence on coordination number is the lower the metal coordination number, the higher the d states in energy, and the stronger they interact with adsorbates. The number of low-coordinated Au atoms should scale with the particle size, d, as d^{-2} (edges) or d^{-3} (corner).

In order to limit the number of independent variables characterizing a catalytic reaction, finding the scaling relationship between adsorption energies and activation energies is normally the first step[8]. For example, for CO oxidation which is a prototypical reaction, it has been found that[7] the CO adsorption energy E_{co} and the atomic oxygen adsorption energy E_o are two independent variables, other adsorption energies, and activation energies have linear relations with these two energies. So the Sabatier rate can be calculated as a function of these two parameters[7]. The adsorption energies can be varied geometrically and electronically.

From a thermal dynamics point of view, the energy interactions between the reactants and catalysts have been studied for decades. However, heterogeneous catalytic reactions represent systems far from thermodynamic equilibrium, and therefore the reaction system typically exhibits rate oscillations, spatiotemporal patterns, and chaos – a group of phenomena named as 'dissipative structure' by Prigogine[9]. The discovery of oscillatory kinetics of a heterogeneous system dates back to the experiments by Fechner and co-workers[10] in 1828 on an electrochemical reaction. With the observation of rate oscillations in catalytic CO oxidation by Wicke and co-workers[11], a strong interest[12] remains in the oscillatory behavior of heterogeneous reactions. Gerhard Ertl's[9] group has successfully elucidated the catalytic system oscillation for CO oxidation and synchronized the surface structure oscillation and reaction oscillation. Based on that work and other scientific contributions they won the 2007 Nobel Prize for Chemistry.

1.2 Au based catalysts

1.2.1 Au single crystal surface

Fundamental investigations of reactive chemistry on gold-based model catalysts can provide significant insights into mechanistic details of these reactions since it is possible to carefully control surface structure and reaction parameters on a single crystal system. With the development of spatiotemporal resolving techniques, such as low-energy electron diffraction (LEED), photoemission electron microscopy (PEEM) and scanning tunneling microscope (STM), etc., surface reconstruction or surface self-organization with or without gases present have been extensively investigated on model surfaces under a range of conditions. For example, Theoretical works on surface stress and surface reconstructions have been proposed by Needs[13] and Cammarata [14,15] in the 1990's.

Gold has a face-centered cubic (fcc) structure and three low Miller indexed surfaces, (100), (110), and (111), are usually exposed. The coordination number of atoms at the surface for these three different facets is 7 [Au(100)], 11 [Au(110)], and 9 [Au(111)]. The surface energies for gold are 0.08, 0.10, and 0.05 eV/Å^2 for the clean (100)[16], (110)[17], and (111)[18] surfaces, respectively. The ideal crystalline arrangement of the atoms associated with each of the facets is not the most stable. Therefore, all the faces undergo reconstruction.

Au (111) surfaces typical have a $22 \times \sqrt{3}$ herringbone structure which is a result of a balance between two opposing tendencies[19]: the surface layer undergoes contraction to compensate for its reduced coordination, whereas opposing this contraction the underlying gold substrate potential favors a commensurate surface layer[20]. Due to these two competing processes, two domains of surface atoms occupy fcc and hexagonal close-packed sites associated with a periodic array of pairs of partial dislocations formed on the (111) single crystal surface.

Reconstruction of the Au (110) surface into the (1x2) pattern with the "missing row" along the $\{1\bar{1}1\}$ direction was found by means of low-energy electron diffraction (LEED). In the presence of surface defects, (1x3), (1x5) and (1x7) patterns have also been observed. The reconstruction leads to a distortion of the underlying layer, and a lateral displacement of 0.07 Å of the top layer with ~20% contraction in the vertical direction as reported by Moritz[21].

Compared to the previously mentioned low indexed surfaces, the reconstruction of the Au (100) surface is controversial. (1x5) is the most commonly reported reconstruction, followed by (5x20) with rotation, (24x28) with rotation and a hexagonal (5x28) R0.6°. The reconstruction could also be a combination of the above-mentioned structures depending on the surface temperature and defect density. The displacements could occur in the topmost and subsurface layers.

Gold single-crystal surfaces do not measurably chemisorb oxygen either molecularly or dissociatively under ultrahigh vacuum conditions[22] or at elevated temperatures and pressures[23]. However, molecular oxygen physically adsorbs up to ~50 K. In order to investigate the interaction between oxygen and gold surfaces, atomic oxygen has been created by several associated methods: thermal dissociation of gaseous O_2 on hot filaments, ozone decomposition, coadsorption of nitrogen oxides and H_2O, O^+ sputtering, electron bombardment of condensed oxygen etc.

CO is a probe molecule which has been widely used to investigate the surface structure of metals via adsorption and desorption on the metal surfaces. CO adsorbs on the gold (111) surface at cryogenic temperatures under UHV conditions. At higher temperature, the strong interaction between adsorbed CO and Au (111) occurs, and as a result, either the lattice spacing expanded, or the morphology was modified with a structural transformation from herringbone to a 1x1 pattern. CO adsorption on the Au (110) has five states: multilayer at 32K, second layer at 37K, physisorbed first layer at 145K, physisorbed first layer at 67K and chemisorbed at 145K[24]. At 300K, high coverages of chemisorbed CO could be obtained, with increasing exposure time, CO further dissociated accompanied by a surface roughening or a lifting of the

terrace. No ordered adsorption structure of Au (100) was observed in LEED patterns. CO chemisorption is favored at low-coordinated sites, with the classical trend: terraces<steps<kinks< adatoms[25].

Oxygen interacts favorably with undercoordinated gold in the form of terrace vacancies, steps, and 2D islands but not with single adatoms and 3D islands. At low coverages, atomic oxygen has a repulsive interaction with adatoms and an attractive interaction with vacancies which cause the release of gold atoms from the surface in the presence of oxygen[26]. The surface structure of gold indeed affects the nature of oxygen adsorbed on the surface. Step sites bond oxygen adatoms more tightly than terrace sites. In the presence of oxygen at low coverage, atomic oxygen interacts with adatoms repulsively, and attractively interact with vacancies which could release gold atoms from the surfaces.

Adsorbate	gold surface	desorption temperature	ref
CO	polycrystalline	170K	27
CO	Au(332)	140K, 185K	28
CO	Au (110)	multilayer 32K, bilayer 37K, physisorbed monolayer 55K, 67K, chemisorbed 145K, defects 190-220K	29
Atomic O	polycrystalline	recombination O_2 650K	30
Atomic O	Au (110)	recombination O_2 590K	31
Atomic O by e^- bombardment O2	Au (110)	Au_2O_3 decomposition to O_2 497K chemisorbed O recombination to O_2 553K	32
Atomic O by O^+ sputtering	Au (110)	surface oxide 415K, chemisorbed species 545K, phase transformation species 620K, bulk O (?) 850-680K	33
O_2	Au (110)	multilayer 37K, monolayer 45K, 51K	34
O_3	Au (111)	decomposition to O atoms 550K as O_2	35
Atomic O	Au (110)	O_2 470K	36
CO_2	Au (110)	105K	24
Atomic D	Au (110)	216K as D_2	22
D_2	polycrystalline	125K on defects	37

Table 1.1 Results from TPD experiments for various adsorbates on bulk gold surfaces. Reproduced from[23].

Low coordination sites can be the adsorption sites for hydrogen and deuterium. Stobinski[38] found hydrogen and deuterium molecularly chemisorbed on a sintered gold film at 78K and desorbed at 120K. The AuH_2 complexes formed are similar to the compounds produced due to H_2 interactions with isolated Au atoms.

1.2.2 Au Nanoparticles

Due to the low stacking fault and twin boundary energy and surface energy anisotropy, gold nanoparticles can exhibit several structural and morphological modifications. These include single or multiple twinning (parallel, contact) or cyclic twinning resulting in decahedral and truncated decahedral structures. A quantitative equilibrium phase map for gold nanoparticles was established by Amanda[39] based on a combination of relativistic ab initio thermodynamic calculations and *in situ* high-resolution electron microscopy studies at elevated temperatures as shown in Figure 1.3. The ground state determination of size-selected Au nanoclusters[40] annealed by a focused electron beam shows that fcc and decahedral structures are more stable than icosahedral.

When nanoparticles are supported on crystalline oxide substrates, preferential crystalline relationships normally form to lower the matching energy between nanoparticles and oxide substrate. Many of these relationships have been reported: Au (111)//TiO_2 (110) for Au/rutile TiO_2[41], Au (111)//TiO_2 (112) for anatase TiO_2[42], and Au(111)//CeO_2(111) [43,44] Au(111)//NiO(111) etc.

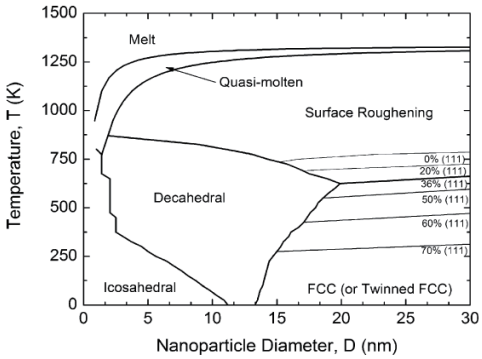

Figure 1.3 Quantitative phase map of gold nanoparticles based on relativistic first principles calculations. Reproduced from[39].

These observations suggest that nanoparticle growth mechanisms should primarily take into consideration nucleation and kinetics, and not only thermodynamics or physical constrictions. The presence and orientation of twin planes in these fcc metals direct the shape of the growing particles as the following examples demonstrate: Twin planes generate reentrant grooves, which are favorable sites for the attachment of adatoms[45]. A single twin plane in triangular prisms direct initial seed growth in two dimensions[46]. Twin planes in hexagonal platelets allow fast-growing edges to regenerate one another[46]. Fivefold symmetry twins in rods and wires constrain the growth in one dimension[46]. These twinning directed growth mechanisms are of great interests in order to synthesis shape controlled functional nanoparticles.

However, direct experimental observations of the twinning process at the atomic scale are lacking in the literature, especially for supported nanoparticles. In Chapter 5, I have summarized several twin types on the model Au/CeO_2 system that are a result of the crystalline constriction between oxide substrate and nanoparticles. Moreover, the dynamical twinning process has been recorded by time-resolved HRTEM.

1.3 In situ time-resolved observation of surface dynamics

Normally, microscopists focus on characterization of the intrinsic structure of a material and the beam induced changes in materials tend to be dismissed. Recently, the electron beam has been proved as a manipulated probe. The beam can provide enough energy for a system to overcome an energy barrier. The growing recognition of electron beam induced changes can, in fact, be informative, especially in beam sensitive 2D materials[47, 48] and functional nanoparticles[49,40] . Beam-induced surface diffusion[50,51], phase transformations[49,52], structural reconstructions[53] and structure modifications[54,55] have been reported for various materials. The interaction between the electron beam and the specimen has a strong dependency on investigated materials. The material response to beam should be taken into account before an intrinsic properties investigation.

The influence of` the electron beam can be reduced in several ways but should be investigated on a per sample basis as effects may vary not only with sample chemistry and morphology but also with sample preparation. Typical approaches to minimize the effects of the electron beam are lowering the acceleration voltage of the microscope, lowering the electron flux density and minimizing the total sample exposure time. Using low electron flux illumination for the acquisition of single images and allowing the sample to relax between subsequent image acquisitions, will allow the sample enough time to dissipate the energy acquired from the beam. In this way, weakly excited objects can relax to the original state prior to the next acquisition. Based on this approach, the "divide and conquer" [56,57] technique has been proposed to increase contrast by recording large image series averaged in some manner to reduce the accumulated electron flux for radiation-sensitive objects and by improving the overall quality and interpretability of the images[58]. Egerton has reviewed several types of energy dissipation: phonon excitation, heating, radiation, displacement, etc[59]. The dynamic responses of the sample can be classified into reversible or irreversible responses[60]. In the case of a reversible response, the sample will regain its original structure; this means that there is a chance to tune the imaging conditions to a level where the true unperturbed structure can be imaged. This is not the case for irreversible responses when imaging over a period longer than the time it takes the sample to destruct.

When the aim is to determine the dynamics of the nanostructure and the rate of atomic displacements, it is essential to monitor how rates vary with varying electron flux and sample stabilities. In chapter 3, surface atom diffusion of supported Au nanoparticle has been observed using HRTEM under a range of electron flux densities.

Time-resolved observations of dynamics either induced by the electron beam or by the surrounding environments (such as a varying temperature and gas composition) have attracted much attention in the past ten years[61]. One of the most significant areas of study is the in situ investigation of oxide-supported metal nanoparticles in reactive gas atmospheres. Au, Pt, and Pd supported on CeO_2, TiO_2 and MgO are usually employed as a model system.

Takeda's group has systematically studied Au/CeO_2 catalysts using ETEM[61–64]. By establishing a morphology diagram under various gas conditions, and with due consideration to electron beam irradiation effects, the conclusion reached was that morphology changes correlate well with the catalytic activity of supported gold nanoparticles (GNPs) on CeO_2. During CO oxidation in CO/air mixtures, it is possible to state that, 1) CO molecules are adsorbed on the surface of GNPs and stabilize GNPs exhibiting the polyhedral shape enclosed by the major {100} and {111} facets, and 2) O_2 molecules are dissociated into oxygen atoms or active oxygen-related species by the catalyst, partly with the aid of electron irradiation, thus inducing the formation of rounded or fluctuating multifaceted surfaces of GNPs.

The oscillatory behavior of catalytic reactions under fixed conditions has attracted wide attention during the last decades[10]. This oscillatory behavior is commonly perceived as a periodic transformation between bistable states. The first successful synchronous in-situ TEM characterization of periodic reaction changes and periodic morphology refacetting was conducted on Pt nanoparticles by Vendelbo[12]. However, these results were obtained under ideal experimental conditions and are not applicable to real world. To fully understand the catalytic process, fundamental investigations of dynamic morphology responses of the catalysts should be taken into account.

Xiaoqing Pan's group have conducted many investigations on the reversible surface dynamics of Pt based alloy nanoparticles during oxidation and reduction cycles at the atomic scale[65–67]. Most of their work has been carried out in STEM mode in which a focused electron beam is used. The STEM technique makes it easier to combine spectroscopy to interpret local composition information and synchronize that information with morphology changes, for example by monitoring the surface oxidation and reduction of alloy nanoparticles[66]. However, the focused electron beam had such a strong, deleterious, effect that the material degraded during the observation. 4D ultrafast STEM with a laser excited electron source can overcome this weakness. But with the laser excited source only one or a few electrons see each reaction, and thus millions of cycles are required to form an image, it limited to perfectly reversible reactions.

In order to track surface dynamics without the damaging effects of the electron beam, temporal HRTEM (parallel illumination) has been employed under low dose rates that allows us to maintain atomic spatial resolution and sub second temporal resolution at the same time. In this project, surface diffusion and dynamic structure responses, plus, prolonged atomic structure tracking are shown to be achievable by means of HRTEM and ETEM. Chapters 4 and 5

systematically summarize the surface dynamics of CeO_2 supported Au nanoparticles and deal with the solid-solid interface structure transformation and gas-solid interface dynamics.

Chapter 2 Methodology

In this chapter, I will introduce the equipment and data processing methods used in this work. The first part is a brief description of transmission electron microscopy (TEM) and a particular focus on the basic principle of high resolution transmission electron microscopy (HRTEM), HRTEM image simulation, then environmental transmission electron microscopy (ETEM). The second part consists two parts of strain analysis method and neural network applications in HRTEM image analysis. Finally, the third section is devoted to sample preparation.

2.1 Transmission electron microscopy

All experiments in this thesis have been performed on the same transmission electron microscope. The basic principle of TEM is that high energy electrons interact with a sample either elastically or inelastically generating different signals (e.g. images, diffraction patterns, X-rays, and energy loss spectra). These signals can be detected using appropriate detectors. There are mainly three characterization approaches used in the TEM: imaging, diffraction, and spectroscopy. Imaging is the main technique used in this work to observe surface dynamics. In this section, I will explain the principles of TEM and imaging (amplitude contrast). Phase contrast imaging, more commonly known as HRTEM, will be discussed in section 2.4 along with image interpretation methods.

2.1.1 Aberrations

Microscope resolution is essentially the smallest spatial feature that can be resolved in a specimen for TEM. The objective magnetic lenses have positive spherical aberration Cs due to the non-uniform magnetic field. The further a ray deviates from the optic axis, the greater its error in the focal length. Figure 2.1 A) shows how the focus is dispersed due to the imperfections of the lens. The positive Cs is the key problem in phase-contrast transmission electron microscopy (high-resolution TEM). For a conventional TEM without a C_s corrector, the

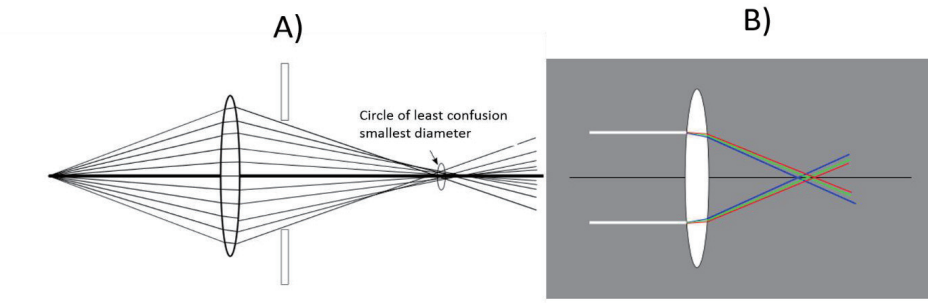

Figure 2.1 A) Lens with positive spherical aberration, showing a shorter focus for off-axis rays B) chromatic aberration.

objective lens should be defocused slightly to compensate for lens aberrations in order to obtain HRTEM images.

Another type of aberration is chromatic aberration due to the energy spread of the electron beam. As a result the focal length depends on the wavelength of the electron beam, as shown in Figure 2.2 B). The electron gun does not produce monochromatic electrons; typically the energy spread is around 1 eV for a Schottky field emission gun used in modern electron microscopes.

2.1.2 Resolution

The driving force for the development of TEM was the prospect of high spatial resolution due to the short wavelength λ of high-energy electrons. In optical microscopy, the resolution is defined as the smallest distance between two features. Rayleigh expressed this in what is known as the Rayleigh creterion

$$\delta = \frac{0.61\lambda}{\mu sin\beta} \quad (2.1)$$

Where λ is the wavelength of the light, μ is the refractive index of the object and β is the semi-angle of collection of the magnifying lens. This equation is often expanded to electron microscopy, however additional parameters also influence the resolution as described below. The wavelength λ of electrons as given by the de Broglie equation, is equal to Plancks constant h divided by the momentum p

$$\lambda = \frac{h}{p} \qquad (2.2)$$

In TEM, the electrons are accelerated in a high voltage electrical field to generate an electron beam energy of $eV = \frac{m_0 v^2}{2}$. When taking relativistic effects into account[68] this becomes,

$$\lambda = \frac{h}{\left[2m_0 eV\left(1+\frac{eV}{2m_0 c^2}\right)\right]^{1/2}} \qquad (2.3)$$

Using Equation 2.3, the wavelengths are 3.35 pm for 120 keV, 2.51 pm for 200 keV and 1.97 pm for 300 keV accelerating voltages.

2.1.3 Contrast

Electrons possess features characteristic of waves. When they travel through the specimen, the wave can change both its amplitude and phase, and both these kinds of changes can give rise to image contrast. Contrast is typically divided into amplitude contrast and phase contrast. In most situations, both types of contrast contribute to an image, although one of them will tend to predominate. In this section only amplitude contrast is discussed. Phase contrast will be discussed in the following section of this chapter combined with HRTEM image simulations to give a more comprehensive explanation about HRTEM.

There are two types of contrast in conventional imaging: mass-thickness contrast and that due to diffraction. Mass-thickness contrast arises from Rutherford off-axis incoherent elastic scattering of the electron and is strongly forward peaked. The scattering cross section is a function of the atomic number Z. Heavy elements scatter the electrons at higher angles, and in thicker regions of the sample, the probability of scattering is higher. The scattered electrons will be filtered out by the objective aperture thus making thicker or heavier regions darker. Figure 2.2 shows a schematic representation of mass-thickness contrast in a TEM bright field image.

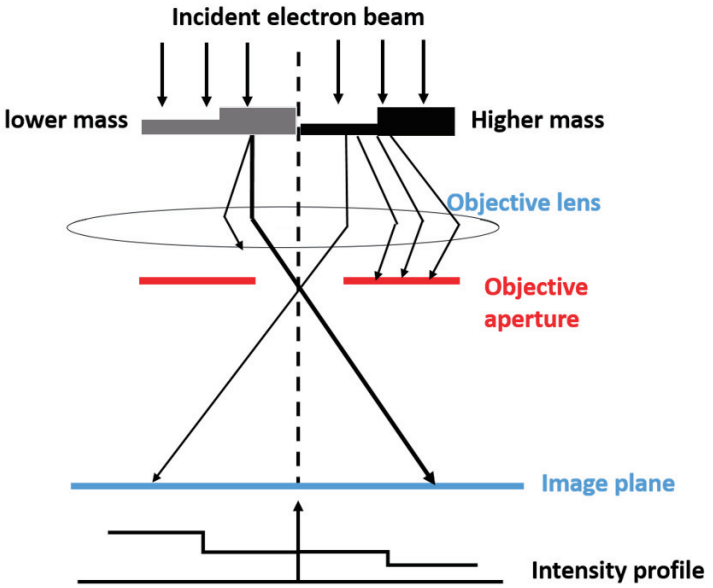

Figure 2.2 Mechanism of mass-thickness contrast in a TEM bright field image. Reproduced from[69].

Diffraction contrast is the result of Bragg scattering in crystalline samples. In this process, the incoming electrons are scattered into discrete locations in the back focal plane. The symmetry and angle of the scattered electron spots can be correlated with the crystalline symmetry of the sample. By moving the objective aperture on the back focal plane, either the direct or a diffracted spot can be selected to form the projected image. Modern TEMs are often equipped with specimen holders that allow the user to tilt the specimen to a range of angles in order to obtain specific diffraction conditions.

2.1.4 Phase contrast and interpretation of HRTEM images

High-resolution imaging is an attractive and fascinating aspect of TEM based characterization as sub-Ångstöm spatial resolution can be achieved. However, obtaining useful information from HRTEM is complicated due to three reasons: (1) information about the sample does not transfer completely to the image detector due to imperfections in the lens system, the resulting

image is distorted when the signal traveled through the optical system. (2) interpretation of the image is based on an atomistic model of the material, which should include all the information of the sample, such as atomic potential, atom arrangement in 3D, etc. (3) the interaction between the electron beam and sample is poorly understood. In order to obtain a satisfactory interpretation of an image and the intrinsic structure of the materials, structure modelling and image simulations are essential.

HRTEM is a phase contrast imaging technique. The phase is not directly observable, and the signal acquired by the detector (camera) is the magnitude squared of the wave function. So, it is necessary to carefully consider the image formation and transfer process: from the beam-sample interaction (signal generation), the optical lens system and finally signal detection.

First, a simplified model with two approximations is used[68]: (1) an absorption function is not considered as it would generally be small in the regime. (2) the specimen is very thin so the potential $V_t(x,y) \ll 1$. That means for a very thin specimen, the amplitude of a transmitted wave function will depend linearly on the projected potential of the specimen. The phase change of the wave from the incident surface to the exit surface depends on the potential function of the sample. So the potential of the specimen can be projected in the z-direction with t being the thickness of the slice

$$V_t(x,y) = \int_0^t V(x,y,z)dz \qquad (2.4)$$

The phase shift is given by $d\phi \cong \sigma \int V(x,y,z)dz = \sigma V_t(x,y)$ (2.5)

σ is an interaction constant that depends on the energy of the primary electrons. The specimen can be considered as weak phase object, the sample transfer function is simplified as

$$f(x,y) = \exp(1 - \sigma V_t(x,y)) \qquad (2.6)$$

Then expand the exponential function, neglecting higher order terms, so the $f(x,y)$ becomes

$$f(x,y) = 1 - \sigma V_t(x,y) \qquad (2.7)$$

The exit wave function, $t(x,y) = exp[i\sigma V_t(x,y)]$, and it Fourier transform is $t(u,v)$.

The electron beam will travel through the optical lens system after it has traversed the specimen. Now we should consider the optical system of the microscope. The contrast transfer function consists of three functions to describe the lens system:

$$H(u) = A(u)E(u)B(u) \qquad (2.8)$$

$A(u)$ is the aperture function, representing the spatial frequency cut-off by the objective aperture. $E(u)$ is the envelope function, representing the attenuation of the wave at high

frequencies. $B(u)$ is the aberration function and represents the effect of the objective lens on the transmitted wave as:

$$B(u) = \exp(i\chi(\mathrm{u})) \qquad (2.9)$$

$$\chi(\mathrm{u}) = \frac{1}{2}\pi C_s \lambda^3 u^4 + \pi \Delta f \lambda u^2 \qquad (2.10)$$

where C_s is the spherical aberration coefficient, λ is the electron wavelength and Δf is the defocus. Multiplication of the exit wave function and the contrast transfer function of the objective lens to obtain the image wave function when the exit wave travel through the lens yields:

$$\varphi(u,v) = t(u,v) \times H(u,v) \quad (2.11) \quad \text{and its Fourier transform } \varphi(x,y)$$

The image signal is acquired on a CCD camera which is a fiber-optic coupled scintillator. For the ideal CCD, each incident electron is only detected by one detector pixel. In practice, though, an electron can generate signals in more than one pixel because of multiple scattering within the scintillator material and the creation of an excitation volume. This effect can be expressed by the point spread function (PSF) of the detector, and its Fourier transform is the modulation-transfer function (MTF). The physical concepts for image simulation are same for both CCD and CMOS cameras, although the technology details and measurement methods of MTF are different.

Convolution of the image function and the modulation transfer function of the detector produces the signal wave function detected by the CCD

$$\varphi = \varphi(x,y) \otimes h(x,y) \qquad (2.12)$$

The final intensity of the wave in the image is

$$I = \varphi\, \varphi^* \qquad (2.13)$$

Above, we assume the sample is very thin to justify the use of the weak phase approximation. In reality, the thickness of the specimen is much larger than the approximation. There are two approaches to deal with an electron wave traversing the sample: multi-slice methods and Bloch wave methods. Figure 2.3 shows a schematic of the multi-slice approach. The thickness of the sample is sliced into thin layers so that for each slice the weak phase approximation applies as the electron wave traverses the sample in the z-direction. In the Bloch wave approach, the specimen is thought of as a filter that converts the incident electron into a superposition of Bloch waves inside the specimen[70]. The Bloch wave method is adapted to the calculation of crystalline solids of small unit cell, while multi-slice method can deal with amorphous solid of larger unit cell or containing defects.

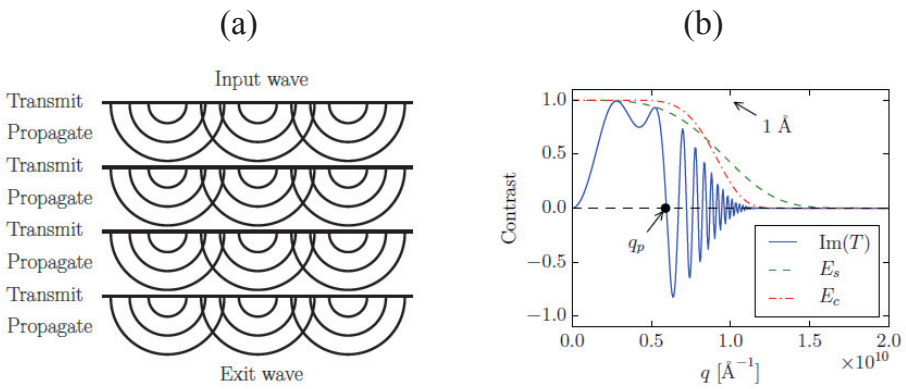

Figure 2.3 (a) The multislice method successively transmits the electron wave through each slice of the potential and then propagates it to the next slice. (b) The contrast transfer function of a HRTEM operated at 300 kV with Cs = 0.6 mm and Δf = - 41.25 nm (Scherzer defocus-the optimum defocus under present microscope conditions). The point resolution q_p corresponds to the first crossing of zero for the imaginary part of the CTF. At Scherzer defocus q_p is maximized. The partial coherence envelopes dampens the high frequency components of the CTF leading to a delocalization in real space. E_s is the spatial envelope, E_c is the temporal envelope. E_s and E_c represent the effect of additional aberrations that damp the contrast transfer function.

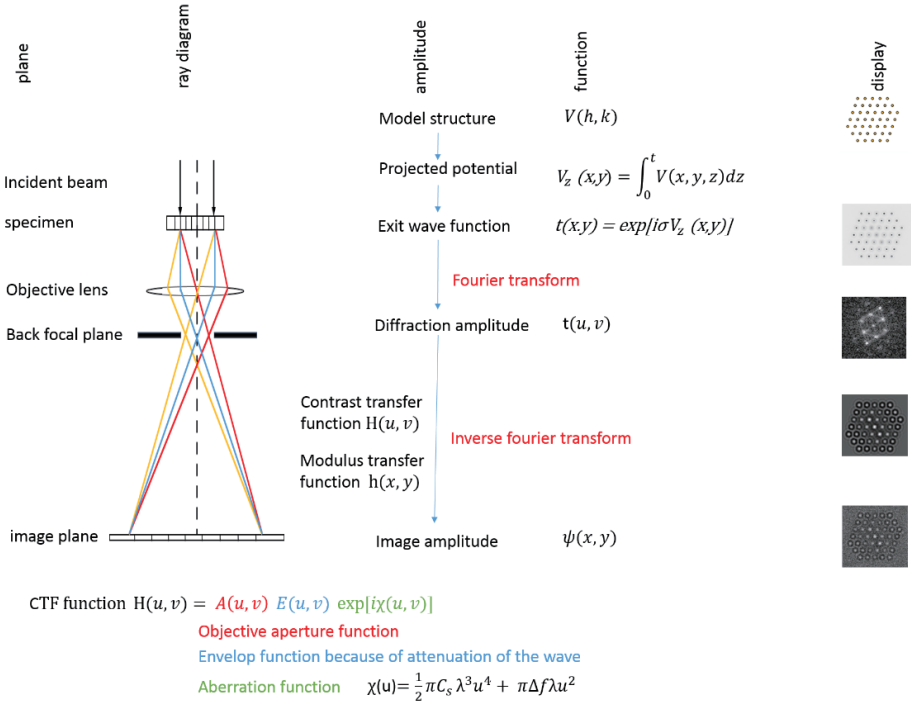

Figure 2.4 Principal of HRTEM image formation and simulation.

The high-resolution transmission electron microscopy simulation steps in multi-slice approach are shown in Figure 2.4:

Step 1 build model using crystalline information of target system, such as unit cell

Step 2 calculates the projected atomic potential $V_z(x,y) = \int_0^t V(x,y,z)dz$

Step 3 calculates the exit wave function (also called the transmission function)

Step 4 Fourier transform the exit wave function

Step 5 Multiplication the Fourier transform of the exit wave function by the transfer function of the objective lens to obtain the image wave function in the back focal plane

Step 6 Invert Fourier transform the image wave function

Step 7 Convolute the image wave function with the Modulus transfer function of the detector and calculate the square modulus to obtain the final image intensity $I = \varphi\,\varphi^*$

2.1.5 Image siumulations and PyQSTEM

There are several commercial and open source programs for simulating electron microscopy images[71–74]. Most of these programs are based on a graphical user interface requiring import of the input structure and export of output images in every simulation. This is impractical for large numbers of image simulations and subsequent analysis. Moreover, such platforms are normally not compatible with other model builder and first principle calculation platforms. Within the framework of this project, PyQSTEM was developed to provide a single programming environment, for carrying out everything related to image simulation, from model building to analysis. PyQSTEM is a Python-based interface and extension to the multislice simulation program QSTEM[72] based on C++ and the FFTW library for computing the discrete Fourier transform in one or more dimensions. Other electron microscopy simulations such as STEM, CBED, and inline holography simulation along with HRTEM simulation in QSTEM, which is also included in PyQSTEM. Potential energy of the system by DFT and finite temperature calculations of the model structure can also be carried out using PyQSTEM. An example of an HRTEM simulation using PyQSTEM is attached in Appendix A.

The Python programming language is open source and has recently gained popularity for scientific applications. There are a large number of free and open-source numerical libraries such as numpy, scipy and scikit-image that provide easy access to a host of common tools, which deal with multi-dimensional arrays, scientific computing, and image analysis. Python is also a leading language for machine learning due to the availability of libraries such as scikit-learn and tensorflow. In this project, a machine learning application in pixel level segmentation of atom column detection in HRTEM is developed and discussedin the following section. Excellent tutorials and introduction can be found elsewhere[75,76].

The atomic model is solved with the Atomic Simulation Environment (ASE) which is extensively used in the theoretical physics community, for doing first principles, ab initio and density functional theory (DFT) calculations. ASE has modules for a wide range of different structures including nanotubes, bulk lattices, surfaces, and nanoparticles. A high degree of manual control is provided, and import capability for most atomic structure file types. Lastly, ASE makes it easier to integrate results from atomistic simulations into image simulations. The program and all its dependencies are open sources under the GNU license. It is available on all platforms from the GitHub repository.

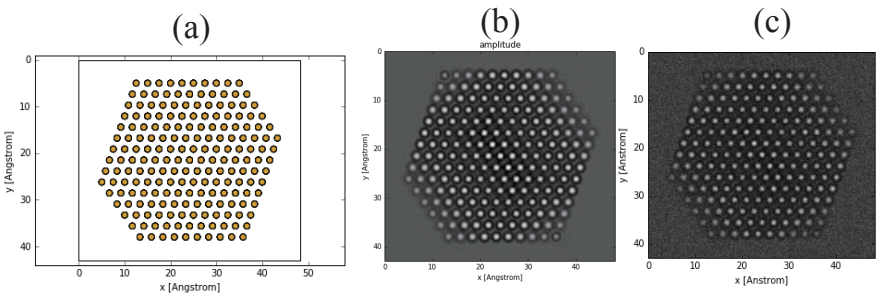

Figure 2.5 ASE built Au nanoparticle, exit wate funciton, simulated image with noise applied.

Typical Image simulation results can be seen in Figure 2.5. Usually, it begins with a model structure of the specimen. Here, a Wulff shaped Au nanoparticle was built using the ASE[77] atoms simulation package. The morphology of the particles is based on information from experiments HRTEM image. Figure 2.5 (b) is the amplitude of the exit wave function and simulated image with detector noise included.

2.2 Environmental TEM

There are two different approaches to perform *in-situ* gas experiments: (1) using a dedicated closed cell sample holder; (2) using a differentially pumped TEM. In the first case, the sample is loaded into the holder between two electron transparent windows (e.g., C or SiN). Either a static gas atmosphere[78] or flowing gas controlled by external pumping systems[79,80] can be established inside the holder. The main advantage of this approach is that no modifications to the TEM column are required, and a gas pressure of up to 1bar can be achieved[80]. The drawback of this approach is resolution limitation and inefficient collection of X-rays for spectroscopy due to the two membranes and gas atmosphere.

The other approach is a differentially pumped TEM. The setup of a differentially pumped TEM is shown in Figure 2.6. Pressure limiting apertures are placed in the bore of the pole-pieces and additional pumping (the red section) is integrated in the column.

The ETEM used in this project is based on the FEI Titan platform, which is a three-condenser lens system with a C_s aberration image corrector, a Gatan imaging filter, and a Gatan Oneview camera. The spatial resolution is around 0.8 Å when the microscope is operated at 300 kV. The

maximum frame rate of the Oneview camera is 300 frames per second (fps) at 512×512 and 25 fps at 4096×4096. These are crucial factors for *in situ* surface experiments where observation of dynamic surface processes is essential. Details of the environmental TEM set up can be found elsewhere[81].

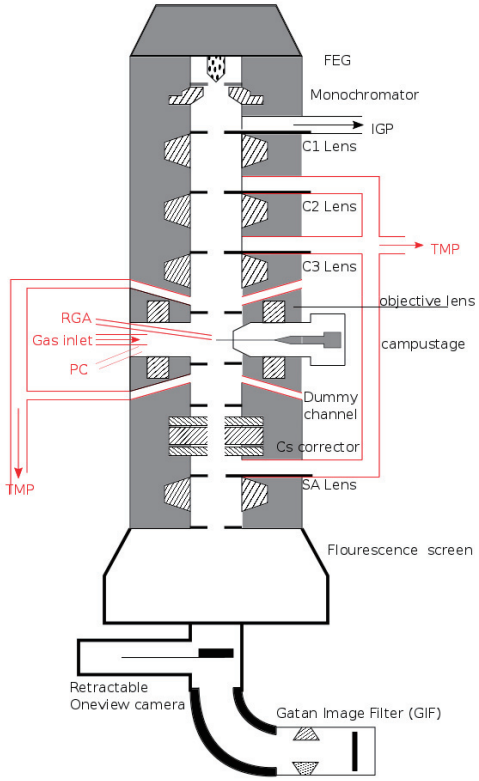

Figure 2.6 Schematic diagram of the differentially pumped TEM column. The black sections denote the standard FEI Titan column configuration. From top to bottom: field emission gun (FEG), ion-getter pump (IGP), condenser lens C1, C2 and C3, sample holder, selected aperture (SA), fluorescence screen, CCD and Gatan Image Filter (GIF). The red sections denote the differential pumping system which consists of three turbomolecular pumps (TMPs) sitting according to C1, C2, and C3 aperture respectively, the residual gas analyzer (RGA), plasma cleaner (PC), gas inlet channels and dummy channels with TMPs integrated around the sample holder. Reproduced from[81].

2.3 Data analysis

2.3.1 Strain measurement at nanoparticle surfaces

There are two main approaches for obtaining values of strain from HRTEM images. The first is to measure the strain directly in real space, either by measuring the interatomic distance[82,83] or comparing the true column location to a reference template[84]. The other method is analysis in Fourier space[85]. These two approaches perform similarly for periodic bulk structures, however, at surfaces or interfaces, the latter can result in some serious artifacts. Therefore we adopted the former to determine the strain map of the supported nanoparticles.

The critical step is to determine the positions of the lattice points, and there are several ways to accomplish this. The most common way is to locate intensity extrema with sub-pixel accuracy by fitting a 2D function, either a polynomial or a Gaussian to the experimental image. It is also possible to define the lattice positions from the center of mass of the intensity distributions. These two methods are slightly different with measurement errors of the same magnitude[86].

The peak pairs algorithm[83] is the most widely used method for finding strain, given a set of measured atomic positions from an HRTEM image. However, this method uses only two lattice vectors to calculate the strain and hence it is sensitive to noise. Our method uses a larger number of lattice vectors. For example, for an fcc crystal in the [110] zone axis, four nearest and two second nearest neighbors are chosen to find the strain at any lattice point. This approach has two significant advantages: 1) it allows us to determine the strain for lattice points at all surfaces, interfaces, and corners, which is tedious with the standard peak pairs algorithm; 2) it is more stable in the presence of noise.

The strain is computed at each lattice point, by comparing the positions of the neighboring lattice points in an ideal template lattice to the corresponding measured lattice points. In practice, this is achieved by finding the optimal affine transformation A**,** between the two sets of vectors. Here we use a least-squares fit to determine A**:**

$$r = min_A \sum_i^N ||Av_i - w_i||$$

Where r is the residual term, v_i and w_i are the ideal and measured lattice vectors respectively, A is the affine transformation and $||.||$ denotes the Euclidean norm. The orientation and elastic strain matrices can be extracted from A via a left-sided polar decomposition of the deformation gradient:

$$PU = A$$

Where U is an orthogonal right-handed matrix (the rotation axis), and P is a symmetric matrix (the elastic strain matrix).

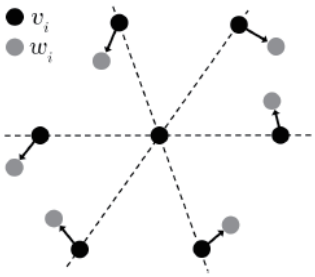

Figure 2.7 The black points indicate the ideal lattice for an fcc crystal in the [110] zone axis. The grey points are the positions of slightly displaced lattice points for a strained crystal. The strain at the central lattice point is calculated by finding the optimal affine transformation between the black and grey points, denoted by v and w respectively.

In this thesis, planar strain ε_p associated with lateral displacement of a column and perpendicular strain ε_n associated with surface relaxation are the two quantities of particular interest for our investigation: Where $\varepsilon_p = \frac{1}{2}(\varepsilon_{xx} + \varepsilon_{yy})$ and $\varepsilon_n = n^T \varepsilon\, n$. The strain measurement errors are discussed thoroughly elsewhere[86].

2.3.2 Application of convolutional neural networks for column recognition in HRTEM images

With the development of high-speed cameras, it is possible to acquire large amounts of data in a short period of time. For example, the capability of the OneView camera is 25 fps at 4k image resolution. The size of a movie including 300 frames is around 19 GB, which is a huge dataset for manual analysis. During a normal experimental day, tens of thousands of images can be recorded. Hence a method for automated analysis is highly desirable.

Interpretation of HRTEM images is a complicated task due to the phase contrast nature of HRTEM images, which is extremely sensitive to the focus, optical aberrations and local vibrations of equipment. In addition, the electron dose must be limited to reduce radiation damage to the sample. All of these factors lower the signal-to-noise ratio of the images. Moreover, surrounding gases used during *in situ* characterization reduces the signal-to-noise ratio of the images still further. These challenges underline the need noted above to automate the analysis of HRTEM images.

In the last few years, deep learning has gained much attention due to the excellent performance of convolutional neural networks (CNNs) in visual recognition tasks. The application of CNNs covers image classification, object detection, pixel level segmentation and more. Especially for

the analysis of medical images, CNNs have become the state-of-art, in tasks including mitosis detection and automatic segmentation of brain images. In this project, a method using a CNN to detect the local structure in HRTEM images is proposed. For example, for identifying the individual atomic columns in images of nanoparticles.

Deep neural networks require a huge amount of data for training. Usually, this data consists of images characteristic structure labeled by humans, for instance images of the brain. Such datasets are not available for HRTEM and it is very expensive to create such databases, so simulated images are used to train the neural network. The results have shown that a neural network trained on simulated images is able to identify the local structure in experimental images.

The proposed method is based on pixel-wise segmentation. The task is to classify and localize all instances of a structure in a grayscale intensity image and assign a 2d oordinate to each intensity extreme. The segmentation proceeds as a supervised learning problem that learns the mapping from an image to a probability map, representing the likelihood of occupancy of some structure class. The coordinates of the structures of interest are obtained from the local maxima in the probability maps. The probability map regression is achieved by training a CNN using the mean squared difference between the output and the true probability maps as the loss function. The intensity at the extremes is taken as a measure of the confidence in the predictions of the occurrence of the structure. Figure 2.8 shows neural networks detection of intensity extremes (either maxima with negative defocus or minima with positive defocus) on a high resolution image of graphene: a) is the experimental image, b) is the prediction of the extremes location, c) shows the dot annotations with detection probabilities larger than 0.01, due to the low detection probability setting the noise can also be detected (the blue circles) d) shows the dot annotations with detection probabilities larger than 0.5. In this thesis, neural network column detection is demonstrated in chapter 5, where atomic columns are identified

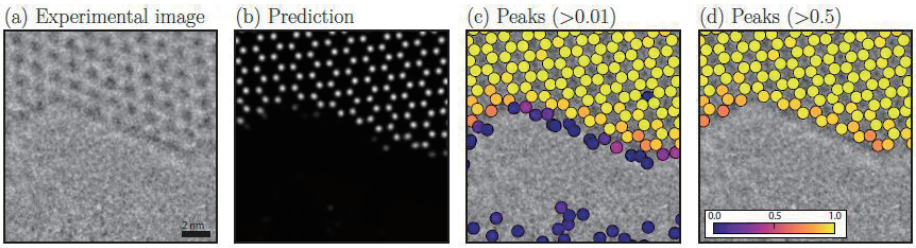

Figure 2.8 A neural network trained exclusively on simulated data is capable of generalizing to experimental images. (a) Single suspended graphene sheet with a hole formed under the influence of the electron beam. (b) The regressed probability distribution predicted by the neural network for the image in (a). (c) The local peak positions of the probability map is overlaid on the image. The peaks are color-coded according to their maximum value. Peaks with a maximum value less than 0.01 are excluded. (d) A higher tolerance for exclusion is used to remove peaks with a maximum value less than 0.5.

2.4 Sample preparation

There are two main approaches to obtain oxide supported nanoparticles: by chemical synthesis or by physical deposition. For large scale commercial production, the chemical method is normally used due to the low cost of production. The drawback of a chemical process is that it is generally complex, and normally has remaining ligands or other contamination from the chemical syntheses. As a result, it will introduce many solvent molecular to the system and make it complicated to interpret the *in situ* experimental results. For fundamental research purposes, model systems are employed to simplify the systems and to achieve better correlation between specific sample conditions and catalytic reactions. Physical methods such as mass-selected deposition, and sputter coating are used to obtain simple model nanoparticle systems. Both chemical and physical sample preparation approaches have been used in this project. Most *in situ* experiments are conducted on the physically prepared samples.

2.5.1 Chemical approach

Two typical heterogeneous catalysts synthesis procedures were employed for preparing six systems: Au/CeO_2, Pt/CeO_2, Pd/CeO_2, Au/TiO_2, Pt/TiO_2 and Pd/TiO_2. The typical morphology of the samples is shown in Figure 2.9.

Deposition precipitation method (DP)

An aqueous solution (H_2PtCl_6 or $HAuCl_4$) was adjusted to a pH of 7 by adding NaOH and heating to 70°C. CeO_2 powder was added, and the suspension was stirred at pH=7 at 70°C for 1h. The suspension was filtered and washed to remove chlorine and sodium ions. Then the sample was subsequently dried overnight, followed by reduction in a H_2 gas stream at 350°C under ambient pressure,

Incipient wetness impregnation method (IP)

Incipient wetness impregnation is another commonly used synthesis procedure for heterogeneous catalysts. A metal precursor such as H_2PtCl_6 was dissolved in a small amount of water, followed by the catalyst support CeO_2 powder, the pore volume of the support should be the same as solution volume. The slurry was stirred for 30 min allowing the solution to enter the pores by capillary forces. The catalyst can then be dried, calcined and reduced.

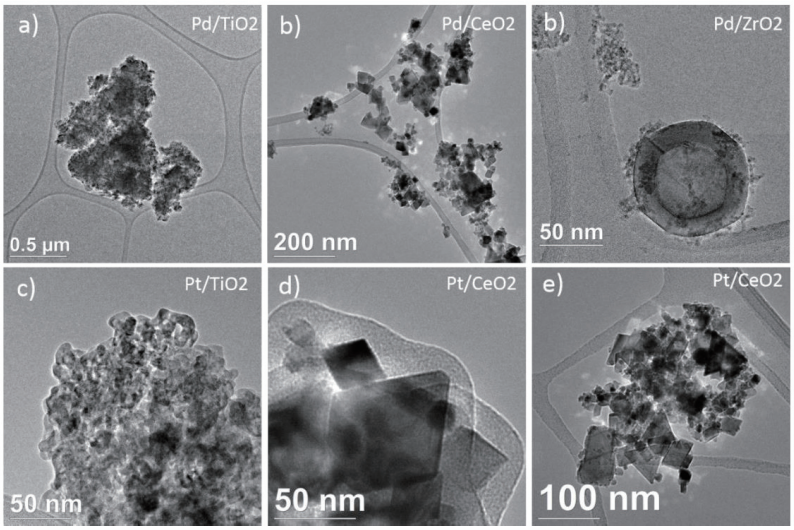

Figure 2.9 Morphology of the samples prepared by incipient wetness impregnation.

2.5.2 Physical approach

Sputter coating

Sputter coating was carried out using a Quorum Q150T sputter coater[87]. In order to determine the most effective conditions to produce highly dispersed nanoparticles, different deposition times were used. Figure 2.10 shows the size and dispersion of the sputtered nanoparticles on lacey carbon films.

Once optimised deposition parameters were established, the next step was to deposit nanoparticles on an oxide substrate. Commercial CeO_2 powder (Sigma-Aldrich) was dispersed in ethanol and drop-cast on a DENSsolutions chip with a SiNx membrane. The chip was dried under a lamp for ten minutes and inserted in the sputter coater. Au was deposited from a gold target using 80 mA current for 10 sec in ionized Argon. The chip was then mounted in a DENSsolutions Wildfire holder and inserted into the TEM. The sample was heated to 500°C in vacuum for 1h resulting in a clean sample of 3 nm Au nanoparticles.

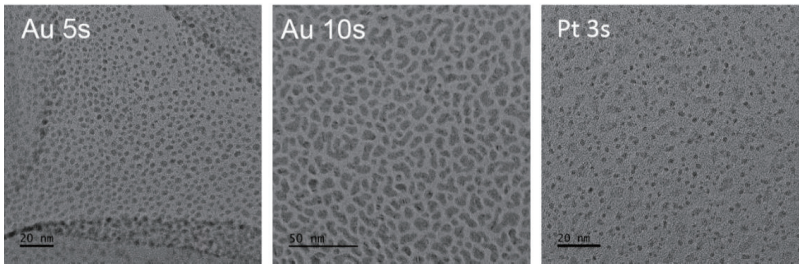

Figure 2. 10 Morphology of sputter coated nanoparticles on amorphous carbon grid. The current used is 80 mA.

Chapter 3 Beam effect on surface atom diffusion

3.1 Introduction

With the advent of aberration correction on transmission electron microscopes, the performance of these instruments has greatly increased; and the resolution is now in the sub-Ångström regime. Studies using such tools are not limited to high or even ultra-high vacuum. With suitable modifications to the microscope column or the use of specialized holders, samples can be investigated under pressures exceeding atmospheric pressure. The possibility of such investigations makes the instrument versatile and highly suited for studies of catalyst materials.

For catalyst materials, the primary interest is the configuration of surface atoms under reactive conditions. Due to the complex structure of industrial catalysts, it is often extremely challenging to derive fundamental properties from such materials. Instead, physically synthesized model systems are often used for this purpose. The synthesis could involve the use of size selected clusters, metal sputtering or evaporation.

High-resolution transmission electron microscopy (HRTEM) studies are normally performed with nanomaterials under high vacuum ($\leq 10^{-5}$ Pa) conditions. However, such conditions are insufficient to study the active functional state of nanomaterials, for example, heterogeneous catalysts, for which the structure and properties depend on the surrounding gas environment[12,62]. Whereas such studies can provide information on the bulk structure of materials such as metallic nanoparticles, they fall short in unraveling the surface structure under reactive conditions. Environmental TEM (ETEM) provides the capability to expose samples to a gaseous atmosphere during imaging and analysis. Moreover, reactions can be studied in operando using a closed cell holder[88].

The major drawback of using an intense high-energy electron beam to probe nanostructures is the lack of understanding how the probe interacts with the sample. A first principles approach may not provide an adequate explanation of the exact sample structure including morphology and interfaces which plays a crucial role in the supply and drain of energy to and from the sample.

However, high-energy electron beams can have a strong effect on nanoparticle samples making it challenging to characterize the intrinsic structure and morphology. Especially for HRTEM, where an accumulated electron flux exceeding 2000 e^{-} $Å^{-2}$ per image is typically used in order to achieve a good signal to noise ratio[89]. Thus, knowledge of the effects the beam may have on the sample is crucial. Phenomena resulting from the transfer of energy from the high energy electron beam to the sample along with relaxation phenomena have been investigated by several

researchers.[56,60,90] The electron beam can even be used as an energetic probe to emulate, tune and quantify functional[53] ability, or to structure materials[91].

The influence of an electron beam can be reduced in several ways, but should be investigated on a per sample basis as effects may vary not only with sample chemistry and morphology, but also with sample preparation. Typical approaches to minimize the effects of the electron beam are lowering the acceleration voltage of the microscope, lowering the electron flux and minimizing the total sample exposure time. Using low electron flux illumination for acquisition of single images and allowing the sample to relax between subsequent image acquisitions, will allow the sample enough time to dissipate the energy acquired from the beam. In this way, weakly excited objects can relax to the original state prior to the next acquisition. Based on this approach, the "divide and conquer" [56,57] technique was proposed to increase contrast by recording large image series averaged in some manner to reduce the accumulated electron flux for radiation-sensitive objects and improving the overall quality and interpretability of the images[58].

Interactions between high-energy electron beams and matter is a complicated topic for both experiments and simulation. Egerton has reviewed several types of energy dissipation: phonon excitation, heating, radiation, displacement, etc[59]. The entanglement of these processes makes it challenging to determine how energy is transferred from beam to object, the relative importance of the different dissipation processes and what the overall behavior of the sample might be.

The dynamic responses of the sample can be classified into reversible or irreversible responses [60]. In the case of a reversible response, the sample will regain its original structure. In effect, this means that there is a chance to tune the imaging conditions to a level where the true unperturbed structure can be imaged. This is not the case for irreversible responses when imaging over periods longer than the time it takes the sample to destruct.

When the aim is to determine the dynamics of nanostructures and the rate of atomic displacements, it is essential to monitor how those rates vary with varying electron flux and extrapolate these to infinitely low electron flux.

For the observation of atom dynamics, the balance between image quality and beam influence should be considered carefully with suitable parameters such as signal-to-noise ratio (SNR), resolution, electron dose, electron dose rate, acquisition time, etc. The time scale of Au surface atom diffusion is from milliseconds to seconds[50]. According to the Rose criterion[92], a SNR = 5[89,93] is adequate to make a high-precision measurement.

In this section, we investigate how the intensity of the electron beam and the accumulated dose influence the surface self-diffusion of gold atoms on gold nanoparticles. Temporally resolved image sequences of the same supported Au nanoparticle were acquired at electron fluxes ranging from 2.7×10^3 to 49×10^3 $e^{-}Å^{-2}$ s^{-1} and the surface dynamics are quantified by identifying events where an entire column of atoms is seen to move on the surface of the nanoparticle. Fluctuations of the surface atom column occupation were measured quantitatively

using sequences of high-resolution transmission electron micrographs. Columns with higher coordination number start hopping under higher electron flux indicating higher internal energy of the particle under the conditions used. The internal energy which contributes the most to the kinetic energy of the diffusing atoms, increases with both the electron flux and the total time of exposure. For a given electron flux, the hopping column number increases as the exposure time accumulates. For columns with high coordination, i.e. higher binding energy, hopping is only observed under high electron flux.

In time resolved HRTEM image sequences, it can be challenging to interpret all atoms in an atomic column and the exact height of the column from one image in a single projection. Although low Z materials such as MgO can be reconstructed in 3D [94] from HRTEM images, the method is not feasible for heavy metals such as Pd, Au and Pt. However, the dynamics of entire atomic columns can shed light on the surface dynamics with information averaged in the z direction.

3.2 Experimental details

Commercial CeO_2 powder (Sigma-Aldrich) was dispersed in ethanol and drop-cast on a DENSsolutions chip with a SiNx membrane. The chip was dried under a lamp for ten minutes and inserted in a sputter coater (Quorum Q150T). Au was deposited from a gold target using 80 mA current for 10 seconds in ionized Argon. After that, the chip was mounted in a DENSsolutions Wildfire holder and inserted into the TEM. The sample was heated to 500°C in vacuum for 1 h resulting in a clean sample of 3 nm Au nanoparticles.

The experiments were performed in an FEI Titan 80-300 environmental transmission electron microscope equipped with a spherical aberration corrector (CEOS) on the objective lens. The microscope was operated at 300 kV. The C_s corrector was tuned to a spherical aberration coefficient better than -5µm. High-resolution TEM image sequences were acquired with electron fluxes ranging from 2.7×10^3 to 49×10^3 $e^{-}Å^{-2}$ s^{-1}. Images were recorded on a Gatan OneView camera at an exposure time of 0.2 sec giving an accumulate electron flux per frame range from 540 to 9800 $e^{-}/Å^{-2}$. HRTEM images were recorded at a magnification corresponding to a sampling of 0.0089 nm/pixel. Between each image sequence acquisition, the sample was allowed to relax for a period of 5 minutes without exposure to the electron beam. The dependence of contrast and SNR on accumulate electron flux were calculated by Lee et al.[89] The data covers a range of electron fluxes typically used for HRTEM image acquisition. Electron counts were measured in the vacuum area of the images provided that 1 primary electron gives 26.42 counts on Oneview camera as specified by the manufacturer.

3.3 Results

In the present work, the focus is on the surface structure of supported nanoparticles under a range of electron fluxes. This is done by observing column occupancy fluctuations at varying dose rates as the most common observation is the disappearance and reappearance of atomic

columns indicating that under the applied conditions, atoms migrate on the surfaces of the gold nanoparticles.

Figure 3.1 shows three gold nanoparticles imaged at three different points in time under different illumination conditions. The common observation is that atomic columns with low coordination disappear. At sites of low coordination, i.e. corners, atomic columns (indicated by the red arrows) are occupied in the left frames and unoccupied in the subsequent frames. This process is often reversible and the atomic column will eventually repopulate. Here, such occupancy changes are referred to as "column hopping." The term is used both for events where an occupied column disappears, or where an unoccupied column is populated. Such surface column hopping has previously been reported in the literature for CeO_2 [53], Pt [51] and Au [50,95].

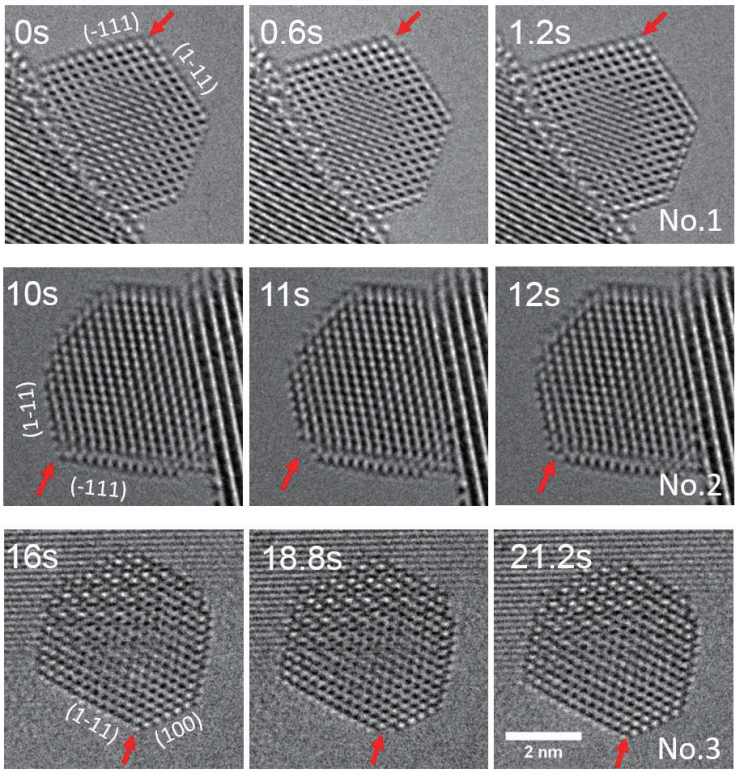

Figure 3.1 Frames from temporal HRTEM image sequences. The occupation of the columns indicated by the arrow fluctuate through the temporal sequences. Red arrows indicate column hopping. Dose rates are 44 × 10^3 e−Å^{-2} s^{-1}, 34 × 10^3 e−Å^{-2} s^{-1} and 8.3 × 10^3 e−Å^{-2} s^{-1} for No1, No2 and No3 particle respectively. Exposure time is 0.2 s for a single image.

This quantification method for surface diffusion is not trivial using HRTEM. The reason is that HRTEM images are 2D projections of a 3D structure. First, each pixel contains information from all the atoms in the direction parallel to the electron beam. Second, recognition of the object becomes increasingly challenging as the accumulated electron flux decreases. The low signal-to-noise ratio of the contrast especially at low electron flux hampers determination of the occupational state rendering some evaluations erroneous due to the strong statistical fluctuation of the noise in such images.

Figure 3.2 A) shows intensity profiles integrated over the topmost 20 pixels of the top layer with five selected electron fluxes, corresponding images are displayed in C). Signal and contrast are quite weak at 2.7×10^3 $e^{-}Å^{-2}$ s^{-1}. The signal-to-noise ratios at different fluxes are measured and displayed in Figure 3.2 B). For the lowest flux (2.7×10^3 $e^{-}Å^{-2}$ s^{-1}), an SNR of 4.68 is measured, which is close to the Rose criterion[89], and indeed the contrast of the corner column is smeared into the noise

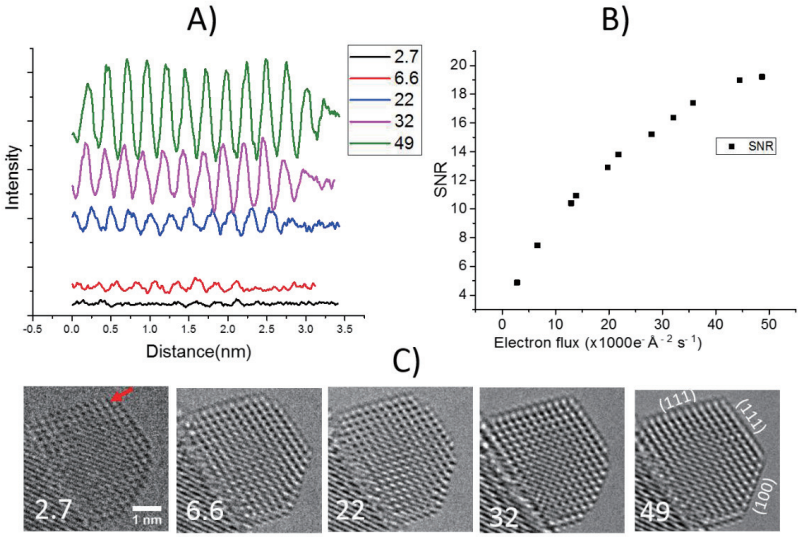

Figure 3.2 A) Intensity profile summed over 20 pixels of the top first layer for five selected dose rates, the top layer was indicated by red arrow in image. B) Experimental SNR versus electron flux. SNR is calculated using average electron counts divided by standard deviation of the counts. All these data were measured in the vacuum area close to the target particle. C) Selected frames extracted from temporal image sequence acquired with different electron flux, the inset number is the electron flux, and the unit is 10^3 $e^{-}Å^{-2}$ s^{-1}. Due to the low signal-to-noise ratio the presence of an atomic column is smeared in the noise making it challenging and ambiguous to count the column occupation.

In order to determine how the electron flux affects column hopping, the hopping rate of the 6 columns closest to a corner is determined as a function of electron flux. The columns are labeled in Figure 3.3. This is done by counting "column hopping events" for a single nanoparticle. The dose rate was increased from 6.6×10^3 $e^{-}Å^{-2}$ s^{-1} up to 44×10^3 $e^{-}Å^{-2}$ s^{-1}, and then decreased

again to 13 × 10^3 $e^{-}Å^{-2}$ s^{-1}, to enable us to distinguish between the effects of dose rate and accumulated dose. For each dose rate, at least 350 frames of 0.2 s each were recorded, and the occupancy of the individual column was noted. Each time an atomic column disappeared or appeared, an event was logged for that specific column. No data was recorded for the lowest electron flux for the reasons mentioned earlier and for the highest electron flux as will be explained later.

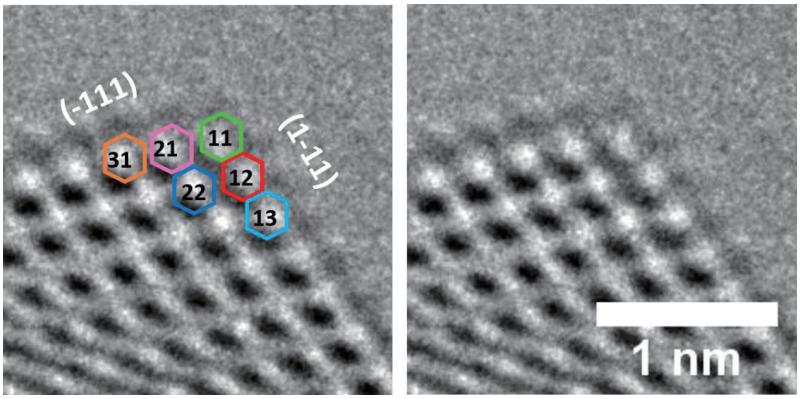

Figure 3.3 A frame extracted from an image sequence showing the corner of a 4 nm gold nanoparticle. The presence and absence of atomic columns at the corner are clearly identified.

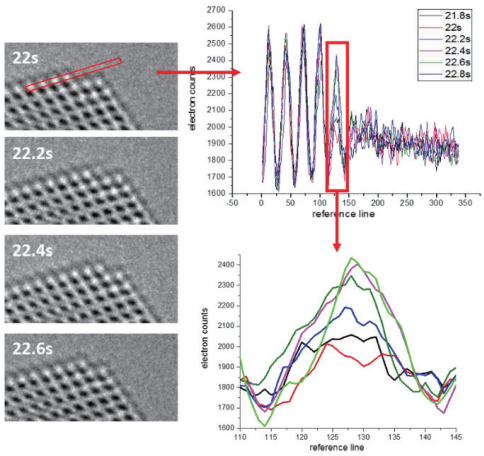

Figure 3.4 Shows sequential frames of the nanoparticle's corner. The intensity of the enlarged peak increased gradually from 22s to 22.6s indicates that atoms number increase in second corner column. It's challenging to trace individual atom diffusion trajectory. However, the gradually increased intensity suggests the exposure time is short enough to catch the column diffusion.

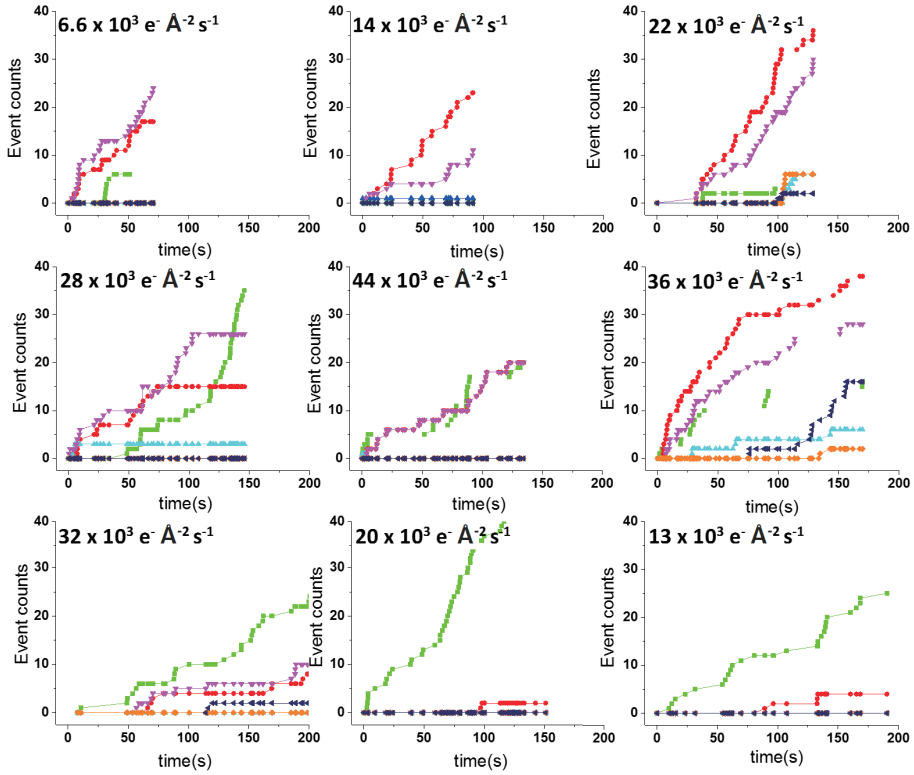

Figure 3.5 Accumulated 'significant' contrast changes as a function of time (frame No.) are shown under different dose rates. The color of the dotted curve corresponds to the location of the column. The dose rate used for temporal image sequences is from 6.6×10^3 e–Å^{-2} s^{-1} up to 44×10^3 e–Å^{-2} s^{-1} then reduced to 13×10^3 e–Å^{-2} s^{-1}. Exposure time is 0.2 s for a single frame. A missing point in the line means no column appears in the image for more than two frames, for example, the green dot-line in dose rate 6.6×10^3 e–Å^{-2} s^{-1}, from frame 200 (blue circle marked) column11 disappears in the image.

Figure 3.5 shows the accumulated count of events for the six atomic columns indicated in Figure 3.3, as a function of electron flux. It should be noted that diffusion events in the columns are not independent, as only the outermost columns in the nanoparticle exhibit diffusion. With column (11) present, no diffusion of the other columns is observed. When column (11) is absent, diffusion may occur in columns (21) and (12). In a similar way, column (21) or (12) must be absent for any activity to be seen in columns (31) and (13), respectively, and both must be absent for column (22) to show activity. This is caused by the lower binding energy of the under-coordinated corner atoms. In most cases, hopping events are only observed in a single column within two consecutive frames. In rare cases, several columns can hop simultaneously during the exposure time of a single frame.

Initially, at a dose rate of 6.6×10^3 e^{-}Å^{-2} s^{-1}, the (11) column is empty and events are seen in the (12) and (21) columns, interrupted briefly by events in the (11) column where it occasionally

fills. Similar behavior is seen in the next two plots, as the dose rate is increased, until late in the plot for 29×10^3 $e^{-}Å^{-2}$ s^{-1}, the (13), (22) and (31) columns are activated. During conditions of high electron flux, activity is seen in most atomic columns, corresponding to significant dynamic roughening of the observed corner of the nanoparticle. As the dose is ramped down again, the activity decreases and the sharp corner is reformed, although the outermost column (11) continues to exhibit significant hopping.

In order to obtain images as those shown in Figure 3.1-Figure 3.3, a significant number of nanoparticles have to be found and observed. Here, the complete analysis was only carried out for a single particle, but several other particles showing similar behavior were observed. Whereas the specific hopping frequencies may depend on factors such as the epitaxial relationship between the support and the nanoparticle and nanoparticle size, the variation in electron flux is expected to be similar.

The various corner configurations for the particle shown in Figure 3.3 are shown schematically in Figure 3.6. The more under-coordinated sites, the higher the internal energy of the system. Energy therefore needs to be supplied to the particle to create the rougher configurations with more low coordinated columns. This energy could be supplied either in the form of thermal energy from heating the sample using a heating holder or from the electron beam. In the latter case, several energy transfer routes are possible.

In Figure 3.6, the corner configuration is shown as a function of time and electron flux, first increasing and then decreasing the electron flux. Initially one or two missing rows are most frequently observed. As the electron flux is increased, the presence of configurations with more missing columns increases. As the electron flux is decreased again, the corner heals and only shows few missing columns. It is interesting to note that while the corner initially fluctuates between one and two missing rows, it ends up fluctuating between a perfect corner and one with a single missing row. Judging from this corner alone, it appears that the nanoparticle has been annealed into a lower overall energy configuration by the electron beam.

In order to extract more information from the dataset, the configuration frequency (frame percentage of total frames) for different electron fluxes is shown in Figure 3.7. It clearly shows that the highest-frequency configuration shifts from number 2 to number 1 or number 0 between these two ranges. The nanoparticle has probably been annealed under irradiation and has become less rough.

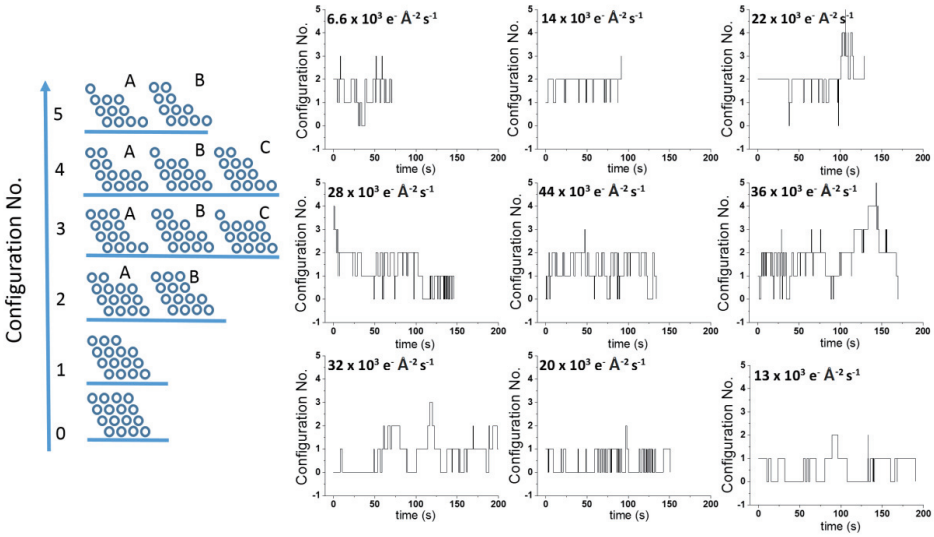

Figure 3.6 Left is internal energy diagram of metastable column configurations in projection view. Right is the time sequence evolution of the corner column configurations under the dose rate range from 6.6 × 10^3 to 44 × 10^3 e–$Å^{-2}$ s^{-1}. All the stretch configurations are observed in the image series. The configurations have been assigned a number. 0 is fully occupied configuration, 1 is missing one column, 2 is missing two columns etc. A, B and C are the energy equivalent types. Configurations with more missing columns have higher potential energy. The x-axis is the time.

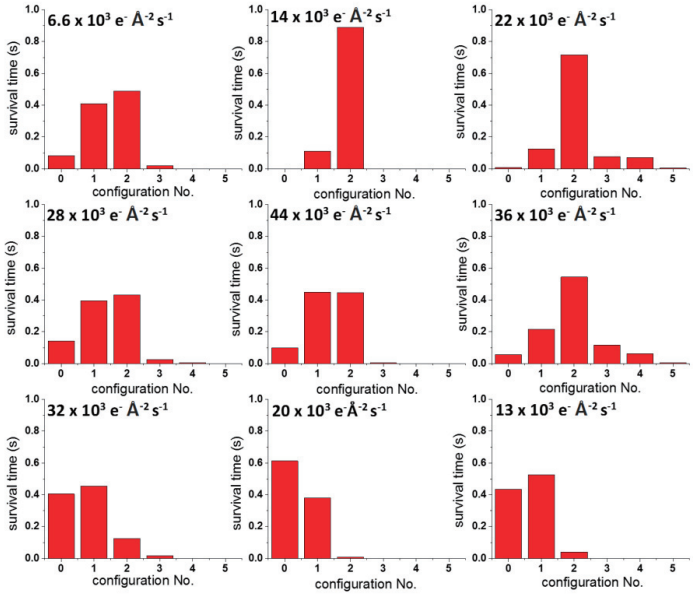

Figure 3.7 Frame percentage of different configurations under different electron flux.

3.4 Discussion

Assuming that the nanoparticle has a constant cross section, the number of electrons passing through the particle is proportional to the electron flux. It is challenging to assess the energy transferred to the sample by a single electron. Van Dyck *et al.* estimated it to be in the range from a few meV to tens of eV, with an average around 40 meV, depending on the material and the imaging conditions. The highest energy transfer would lead to ejection of atoms from the sample, if the energy is transferred to one or a few atoms. While this is sometimes observed under STEM-HAADF imaging condition, no evidence for such reactions is observed in the present observations, implying that if atoms are ejected, the rate is low. Incident high-energy electrons impinging on thin samples could sputter atoms into the vacuum, and is referred to as the knock-on effect. Atom loss may be up to 5 atoms per frame under the focused beam estimated using time sequences of STEM-HAADF images[96]. Such issues are not severe in the present observations. As the electron flux is ramped down, the high index columns missing under a higher electron flux reappear under lower electron flux, as Figure 3.6 shows.

More moderate energy transfer to the nanoparticle can occur through different processes, including electron-hole pair creation and direct momentum transfer to atoms. Regardless of the details of the energy transfer process, the energy ends as thermal vibrations, i.e. phonons. This heat mainly leaves the particle through thermal conductivity, and it is assumed that higher beam intensities lead to higher temperatures of the nanoparticle.

It is therefore assumed that the electron beam can induce enhanced surface diffusivity through at least two mechanisms. First, the general heating of the sample can help the atoms overcome the diffusion energy barriers. Second, energy initially transferred directly from the beam to a loosely bound surface atom will induce a non-thermal velocity, which may also trigger a diffusion event. Both of these mechanisms are expected to lead to an enhancement of the diffusivity, which scales linearly with the beam intensity.

In the experiments, not only an increased diffusivity at increased beam intensities is observed, but also an increased roughness of the corners of the nanoparticle (3.7). This is consistent with an increase in diffusivity, whether from a locally elevated temperature, or from non-thermal motion of the atoms under electron illumination.

The activation energy of an Au atom leaving a step has been estimated to be in the range 0.67 to 0.86 eV, depending on the step geometry.[97,98] This would result in jump frequencies of a few Hz[19] at room temperature, and be consistent with such jumps being observable in the electron microscope. Activation energies in this range also means that a local increase in temperature will result in an order-of-magnitude increase in diffusivity, in agreement with the observations. Experimental results indicate that the local temperature of Cu_2S nanocrystals[49] and graphene increases only by a few degrees.

Beam induced reversible atom displacement of a rhodium catalyst and graphene has been investigated by Kisielowski *et al*[60]. The electron-beam-induced object excitations are highly reproducible if the illumination is confined to the imaged sample area indicating a well-defined

amount of energy from the impinging electron beam is absorbed by the material. Phonon excitation induced low-frequency atom displacement is one reason for the contrast difference between simulated and experimental images, also known as the Stobbs factor. The random phonon excitations of the entire object can temporarily stabilize site-specific (systematic) atom displacement. Atom dynamics was captured in real time in atomically resolved images. The whole excitation and relaxation process takes around 1 min. Due to the excitation-relaxation process, the dose rate is probably as important as the total dose effect on the beam-sample interaction. The 'Divide-and-conquer' approach applied for beam sensitive samples [12,58,60] using sufficiently low electron fluxes so the specimen has enough time to relax between delivered electrons ensures that a purely intrinsic structure is observed[12].

3.5 Summary

Surface atom diffusion of supported Au nanoparticle has been observed using HRTEM under a range of electron flux. Only small differences in individual column jump frequencies have been detected. Higher potential energy configurations present under higher electron flux condition or after long exposure times under moderate electron flux, indicate the excitation-relaxation process of the supported Au nanoparticles. Atom diffusion is one way that the Au nanoparticles can relax energy. The time scale of the excitation-relaxation process is in the order of seconds. The local temperature of particles increases only by a small amount as the hopping is more like a random process rather than exponentially dependent on the dose rates since the relation between atom diffusion and the temperature is in Arrhenius form[99]. To fully understand the dose effect, more experiments need to be conducted at lower temperature and lower acceleration voltage as well as the theoretical work on the energy transfer from the beam to the nanoparticles. The results reported here provide a valuable experimental reference for beam-sample interaction and *in situ* morphology reconstruction and surface dynamics of nanoparticles under reactive and reaction conditions. Both the electron flux and the accumulated dose influence the surface dynamics of supported Au nanoparticles. For a given dose rate, the hopping column number increases as the exposure time accumulates. Columns of higher coordination only hop under relative high electron flux condition

Chapter 4 Time-Resolved Dynamics of Supported Nanoparticles

Heterogeneous catalysis is a molecular bond breaking and rebinding process in which reactant gas molecules adsorb on a solid surface, dissociate, and new molecules are formed and desorbed from the solid surface. Generally, adsorption and desorption are the two limiting steps controlling the reaction rate, which depend strongly on the local electronic and geometric structure of the catalyst. Investigation of the local atomic structure of the catalyst is essential in order to understand its surface properties. Manipulations of surfaces and interfaces either by crystalline facet control or by element composition control is often a key target in catalysis synthesis, for the final purpose of controlling the local atomic structures. On the other hand, the adsorbing molecules can also tune the local structures of catalysts[100], e.g. by changing the surface energy. As a result, the surfaces often reconstruct to a different atomic arrangement, which further tunes the adsorption performance. Heterogeneous catalyst systems are far from thermodynamic equilibrium. Therefore, a comprehensive and synchronized knowledge is required to understand the whole process including catalyst morphology transformations, reaction oscillation, etc.

Since oscillatory kinetics was discovered in catalytic CO oxidation by the group of Wicke in 1970[101], rate oscillations, spatiotemporal patterns, and chaos have been observed with the development of spatially resolving techniques such as field ion microscopy (FIM)[102], *in-situ* LEED[102], and photoemission electron microscopy (PEEM)[103]. Ertl summarizes surface dynamics by introducing two principal new aspects[10]: anisotropic diffusion (surface diffusion) and the possibility of global synchronization via the gas phase (surface reconstruction). However, due to the geometric limitation and nature of the signal of the techniques mentioned above, most surface dynamic observations were conducted on flat surfaces of model systems, which means, only the top-view of the sample has been analyzed.

A systematic understanding of surface reconstruction under reaction conditions requires that characterization methods can visualize atoms in real space and time. *Time-resolved in situ* HRTEM can be a complementary technique for such surface and interface dynamics characterization at the atomic scale from both top-view and side-view. Recent works conducted on Pt nanoparticles by *in situ* TEM shows that synchronized catalysis process characterization can be achieved inside the TEM[12]. The reversible dynamic behavior of nanoparticles under reactive surroundings has also been reported [12,104–107]. However, there are still plenty of unknowns about surface dynamics on nanoparticles, which require systematic studies.

In this project, Cs-corrected ETEM was employed to investigate atomic dynamics in real time in the presence of gas which help us to understand the interactions between adsorbate and nanoparticle surfaces, and, moreover, to understand the nature of active sites for a specific reaction. The motion of atom columns at the surfaces of supported Au nanoparticles have been

directly traced using temporal HRTEM image sequences. The dynamics of surfaces and interfaces were observed at the atomic scale which has enabled us to acquire further knowledge on the intrinsic properties of oxide-supported metal nanoparticles. Such dynamics taking place at either the gas-Au, or Au-CeO_2 interfaces are important for both catalytic performance and stability. This chapter summarizes the dynamical behavior of CeO_2 supported Au nanoparticles based on the geometric dimensionality of the dynamics: 1D, 2D, and 3D.

4.1 1D dynamics

HRTEM images are projections of a 3D object on the camera and all the information in the z-axis is averaged. It is possible to interpret 3D information on light elements with nanometer precision with the help of simulation and precise calibration of the microscope[94]. However, for CeO_2 supported Au nanoparticles, it's challenging to identify a single atom in 3D space from projected HRTEM images, and even more difficult to trace the motion of single atoms.

Thus only projection information in the images is considered and column dynamics are investigated instead of individual atom movement. The nanoparticle dynamics are classified into three categories based on the dimensionality of the dynamics in real space. For example, 1D dynamics refer to single atom column movement which is an atom column spot in the HRTEM images; 2D dynamics are atoms moving in an area of the surface which is an array of atom columns in the images; 3D means whole nanoparticle dynamics which are the changes of an area in the images.

4.1.1 Atom column hopping

Single atom column diffusion has been reported on the surfaces of Au and Pt nanoparticles by Surrey[50,51] and on CeO_2 surfaces by Bhatta[108]. In their observations, the nanoparticles were suspended on carbon grids and were not stable under the electron beam meaning that the shape of the nanoparticles was continuously changing. The occupation of the individual atomic column locations could not be tracked during the observation.

A physically prepared sample consisting of CeO_2 supported Au nanoparticles was used as a model system. This system is stable under the electron beam enabling us to track the column occupation for individual columns. The electron flux influences the diffusion of single atom columns as previously discussed in Chapter 3. In this chapter, the focus is on direct observation of various surface dynamics.

Surface atom columns, especially the corner columns, have lower binding energy compared to fully coordinated inner columns. Figure 4.1 shows a corner column disappearing and reappearing under electron beam irradiation. The red arrows indicate where an atomic column is originally observed at the corner column positions at 0 s and vanish at 0.6 s. This process can be reversible: the corner column reappeared at 1.2 s. The phenomenon has been extensively observed in this work on the surfaces of supported Au nanoparticles. The term 'column hopping'

is here used to describe such a significant variation in contrast, where either an occupied column is emptied, or an unoccupied column is populated.

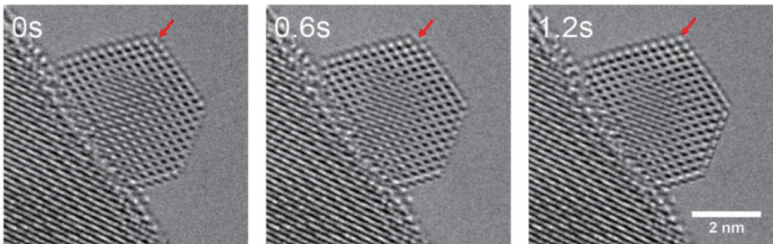

Figure 4.1 Snapshots taken from HRTEM image sequences. In the left image the contrast of the atomic column indicated by the red arrow is significant enough that the naked eyes can identify that there is a 'column'; no significant contrast at the same position in the right image. In reality, all the atoms of this column move to other places of the particle that makes no contrast at corner position.

4.1.2 Reconfiguration of atom columns

Reversible column hopping indicates that some active atoms diffuse on the surface of the nanoparticle. The diffusing atoms can jump between adatom sites if these adatom sites have similar potential energy and the energy barriers between these adatom sites are low enough for the diffusing atoms to overcome. These atoms could jump between several adatom sites back and forth in a random fashion and as a result different surface atomic configurations are formed.

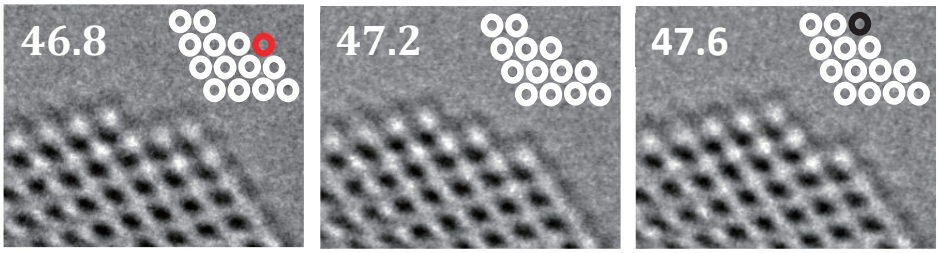

Figure 4.2 Atom column reconfiguration: significant contrast raised at red circle marked location at 46.8s and smeared at 47.2 s; opposite contrast change took place at black circle marked location: there was no contrast can be recognized since from 46.8s and strong contrast raised at 47.6 s.

In Figure 4.2 the location marked with a red circle in the inset sketch was occupied at 46.8 s and empty at 47.6 s, the black location was empty at 46.8 s and occupied at 47.6 s. These locations have similar energies due to crystalline symmetry. The atoms disappearing from the red location at 46.8 s have a higher probability of jumping directly to the black location rather than other locations. The whole transformation process between the atom configurations takes 0.8 s, and the transition state is shown at 47.2 s. The lifetime for an intermediate state is around

0.6 s. Such corner column reconfiguration can be reversible, red column disappeared at 46.8 s, and black column appeared at 47.6 s in Figure 4.2. Figure 4.3 shows the same process at a different point in time.

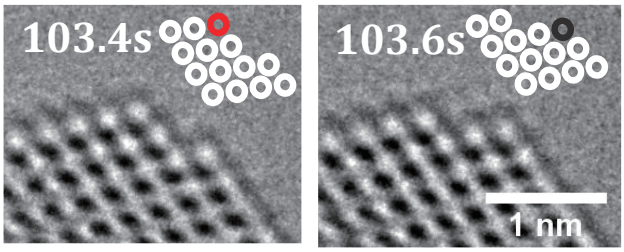

Figure 4.3 Atom column reconfiguration: significant contrast raised at red circle marked location at 103.4 s and smeared at 103.6 s; opposite contrast change took place at black circle marked location: there was no contrast can be recognized at 103.4 s and strong contrast raised at 103.6 s. Experimental conditions: high vacuum, room temperature, exposure time is 0.2 s.

4.1.3 Atom column position deviation

Deviation from the ideal crystal structure during the surface reconfiguration process was also observed. The position of the column indicated by a yellow circle deviates from the ideal crystalline position by 0.07 nm (Figure 4.4) which is much larger than thermal vibration (picometer level)[60] induced position vibration. This column moved out to the surface and formed a new metastable corner. The lifetime of this metastable state is around 0.6 s. Afterwards, this column moves back to the original location. Meanwhile, a column disappeared from the location indicated by the black circle at 21.2 s and a new column populated at the location indicated by the red circle.

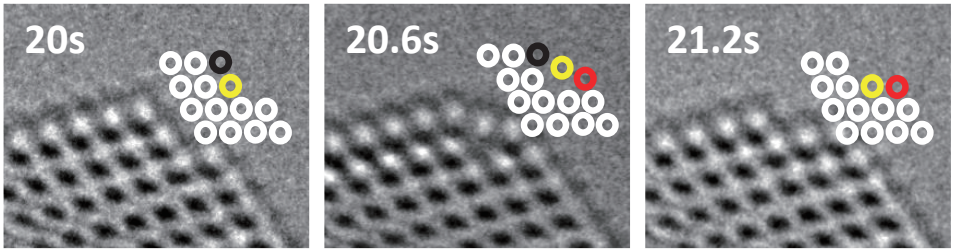

Figure 4.4 The yellow circle indicates a column that deviates from the original lattice position and moves out to vacuum to form a new metastable smooth surface.

Many factors influence the column position deviation from the ideal lattice position, such as thermal vibrations due to the nature of the sample, delocalization induced by the aberration of

microscope due to the microscope abberation and defocus, etc. However, thermal vibration induced deviations are on the order of picometers and hardly observable; delocalization is normally perpendicular to the surface. It has been reported that surface atoms could be sputtered from the sample to the vacuum during high-resolution STEM imaging[96,109]. In that case, the density of electrons is much higher due to the focused beam; the parallel illumination used in TEM results in a significantly lower density of electrons. The total observation time was about 30 min, during which the shape and size of the nanoparticle did not change. Most of the observed dynamical processes were reversible. So one can speculate that the number of atoms sputtered away by the beam was insignificant compared to the total number of atoms in the nanoparticles.

4.2 2D dynamics

In this section, the 2D dynamics observed on Au nanoparticle surfaces with or without gas adsorbed are summarized. As mentioned previously, 2D dynamics in real space projected as an HRTEM image is a 1D signal. The dynamics occurring on surfaces such as surface reconstructions are extremely important for the functionality of nanoscale systems, especially catalysts. Here, Au (100) surface buckling accompanied by the formation of excess columns and (100) surface reconstruction will be discussed. More interestingly, under some conditions (temperature, gas), the entire surface shifts in a concerted manner (Figure 4.10). For example, the columns in the uppermost layers shift in the same direction while maintaining the inter-column distance; column layers disappear and reappear. Although no theoretical explanation for this phenomena is proposed, it is a significant observation.

4.2.1 Surface buckling

Au (100) surfaces typically undergo a (5x1) surface reconstruction and form quasi-hexagonal (111) over-layers. During the reconstruction, excess atomic columns are typically found at corners[43] or on Au (100) surfaces[50,95]. In this configuration, the columns are not stable but fluctuate under electron beam irradiation. As a result, Au (100) surfaces show local bulging when one atomic column is expelled from the surface. Similar column splitting under electron beam irradiation has been observed during high resolution imaging of CeO_2[53].

Figure 4.6 shows buckling occurring on the top most layer of an Au (100) facet. The arrow indicates that the Au (100) surface layer reconstructing under electron beam irradiation. At 8 s, there are clearly five atomic columns. At 9.2 s, atoms move out into the vacuum, and the contrast is lower compared to the previous frame. After an additional 0.8 s, the contrast at the atomic columns is reestablished. The intensity profiles of the topmost surface layer (red box) are displayed in the Figure 4.5 (d). The profiles indicate that the contrast of two corner columns remains stable while the middle columns are lower in contrast during the reconstruction. The process typically lasts one or two seconds.

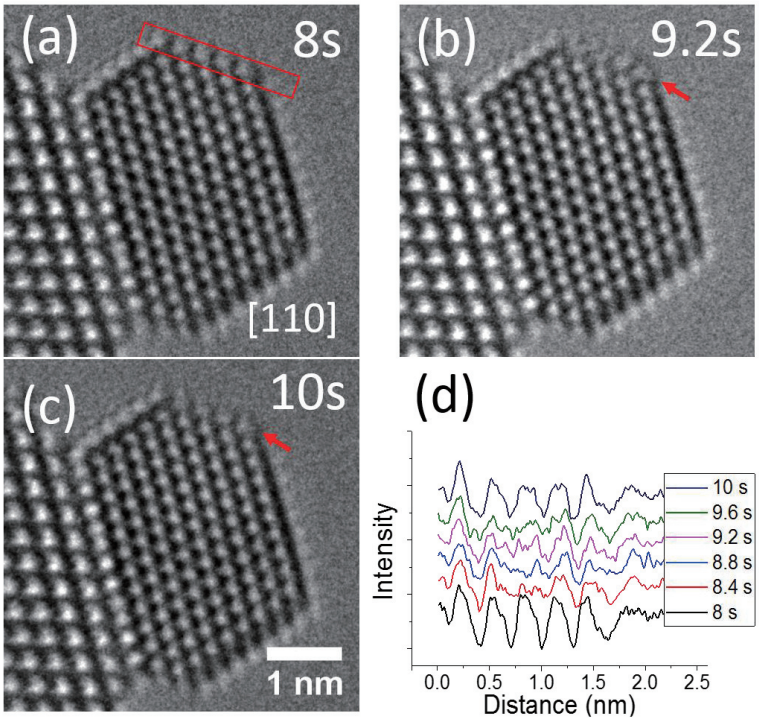

Figure 4.5 Snapshots from a temporal HRTEM sequence. The arrow indicates the (100) top layer of a gold nanoparticle. The particle has an $(111)_{Au}$ // $(111)_{CeO2}$ epitaxial relation with CeO_2 support.

A further observation of excess atom column induced surface buckling is shown in Figures 4.6 and 4.7 where the excess atomic column is indicated by the red arrows. During the observation, the location of the excess column moves back and forth on the facet. Such excess surface atomic columns has been reported in previous HRTEM nanoparticle characterization works [110,111].

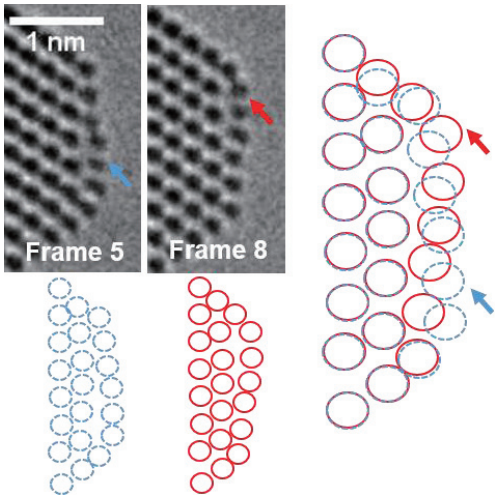

Figure 4.6 Protrude positions according to excess atoms. Arrows indicate the excess atoms.

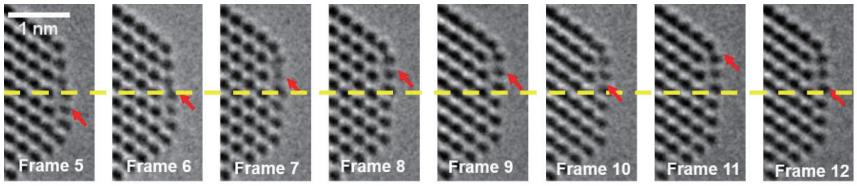

Figure 4.5 The excess atom (indicated by the red arrow) corresponding surface protrusion moves back and forth on the (100) facet. The yellow line is a reference.

4.2.2 Column splitting on the (100) facet

This section demonstrates another phenomenon related to the (100) surface reconstruction. Figure 4.8 shows a (100) surface layer reconstructing under electron beam irradiation. At 90 s, the intensity is elongated parallel to the surface. The elliptical spot (90 s) splits into two peaks (91s) with one staying in the same crystallographic site, and the other is displaced by 0.08 nm from the nearest crystallographic site as shown in Figure 4.8 (c). After further fluctuations at 92 s, the elliptical contrast feature can be seen. The elliptical contrast possible induced by the 2×1 surface reconstruction of the (100) facet.

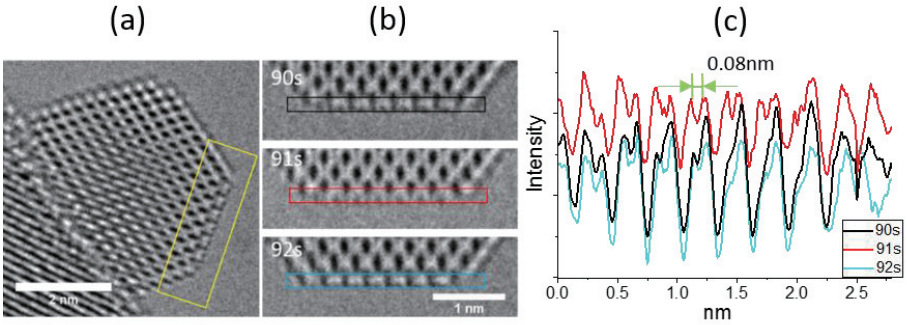

Figure 4.8 Magnified images of the (100) surface reconstruction at selected times.The red box indicates the surface atomic layer reconstructing under electron beam irradiation. Exposure time is 0.2 s for each frame.

The column splitting occurs with a random time constant. No periodicity was observed as can be seen from Table 4.1 where the time and duration of the measured atom column splitting are indicated. Most splitting processes took less than 2 s, a few took longer, and the longest lasted 6.2 s.

Splitting start time (s)	Splitting finish time (s)	Duration time of splitting process (s)
0	0.8	0.8
2	3.6	1.6
11.8	17	5.2
22	23.8	1.8
61.2	62.6	1.4
80.2	83.4	3.2
91.6	92.8	1.2
98.8	100.6	1.8
128	128.6	0.6
132	138.2	6.2

Table 4.1 Start and finish time for each atom column splitting, most processes take less than 2 s.

4.2.3 Layer shifting

The columns in the surface layer could shift in a concerted way as determined from single 0.2 s frames. In Figure 4.9, the columns in the topmost surface layer shift to the left at 20.6 s (the red box) and shift back to the original location at 21.2 s (the blue box). Interestingly, all the columns in this layer behave in the same way, as indicated in the intensity profile (right). The profiles are aligned with a reference on the substrate (yellow circle). The column peaks shift to the left by the same distance of 0.06 nm (7 pixels, pixel size is 0.0089nm) at 20.6 s, and shift back at 21.2 s.

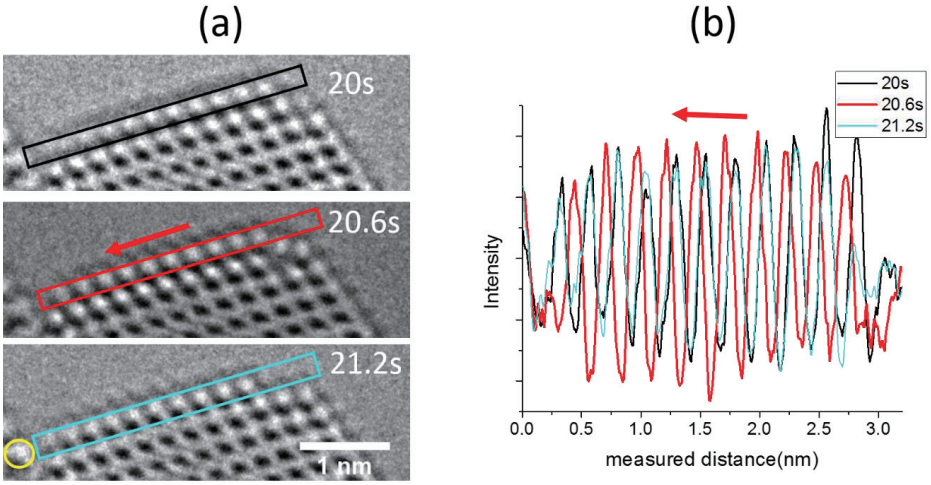

Figure 4.9 Columns in the red frame shift to the left at 20.6 s and shift back to the original location at 21.2 s. The intensity profile at each time is displayed on the right. The line profile is aligned using a reference area on the substrate. All the columns in this layer behave in a concerted manner.

4.2.4 Layer disappearance and reappearance

More than one columns could disappear and reappear at the same time. Figure 4.10 shows a nanoparticle having 9 columns on the (111) facet and 4 columns on the (100) facet at 200.6 s. At 200.8 s the top (100) surface layer (indicated by a yellow arrow) disappears, leaving the nanoparticle with 8 columns in the (111) facet and 5 columns on the (100) facet. However, the layer shows up again at 202 s with the same atom arrangement as at 200.6 s.

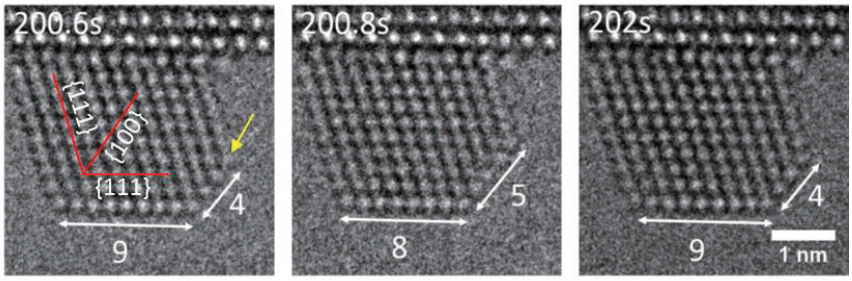

Figure 4.10 Layer disappearance and reappearance oscillation in 4.5 Pa CO at 250°C. The outmost (100) surface layer with 4 columns disappeared at 200.8s and reappeared at 202 s.

4.3 3D Dynamics – Particle Motion

Understanding metal-support interactions are of particular importance for nanostructure designed catalysts. The active sites are generally on the surface of nanoparticles and so a larger surface area means more active sites. Therefore a particularly severe problem for catalysts is sintering where the nanoparticles tend to grow in size resulting in loss of total surface area. Temperature and surrounding gases can accelerate this process[112,113.] Ostwald ripening, and particle migration and coalescence are the two sintering mechanisms[113]. To further understand the underlying processes of nanoparticle sintering and develop mitigating procedures, atomic scale observation of nanoparticle movement on substrates are necessary. In this section, rigid-body sliding, rigid-body rotation and layer movement via mass transport at the atomic scale are discussed.

4.3.1 Rigid-body sliding

Au nanoparticles attached to the oxide support normally have an epitaxial relationship with respect to the substrate. The Au (4x4)//CeO_2 (3x3) relation is a commonly observed structure for this system[44].. The crystalline structure of the Au/CeO_2 interfaces are shown in Figure 4.11 (a). The planes facing each other from both sides are $\{111\}_{Au}$ // $\{111\}_{CeO2}$. The lattice spacing is 0.235 and 0.312 nm for $\{111\}_{Au}$ and $\{111\}_{CeO2}$ respectively; the mismatch is about 25% which is too large to be matched elastically. For a small cluster, the lattice mismatch between the substrate and the nanoparticle can be compensated by distortion of the lattice plane. When the cluster size increases, the energy gain due to interface adhesion is no longer sufficient to compensate for the elastic energy due to the lattice mismatch strain. As a consequence, atoms will leave their preferential adsorption sites and a dislocation network is formed to release the strain at the interface. As the cluster size further increases, the dislocations organize themselves in a periodic network[114]. In the $\{111\}_{Au}$ // $\{111\}_{CeO2}$ case, every four Au (111) layers match three CeO_2 (111) layers to form an edge dislocation (Figure 4.11(a)). A rigid-body sliding movement of the nanoparticle has been observed on the Au/CeO_2 interface with the dislocation network as mentioned above. The blue dotted line is included as reference. The Au nanoparticle moves upward by one Au (111) lattice spacing (around 0.235nm) at 39.2 s. Figure 4.11 (b) shows the intensity profile of the interface layers at 38 s and 39.2 s. The dislocations marked by red lines (Figure 4.11 (a)) remain at the same position during nanoparticle movement.

This rigid-body sliding is reversible. The displacement evolution of the nanoparticle is shown in Figure 4.11 (c). The nanoparticle moves back and forth between two positions, the distance between these two locations is one (111) lattice spacing (around 0.235 nm). Such rigid movement with stable dislocations were found in several other particles and the phenomenon is more common at moderate temperature in my observations.

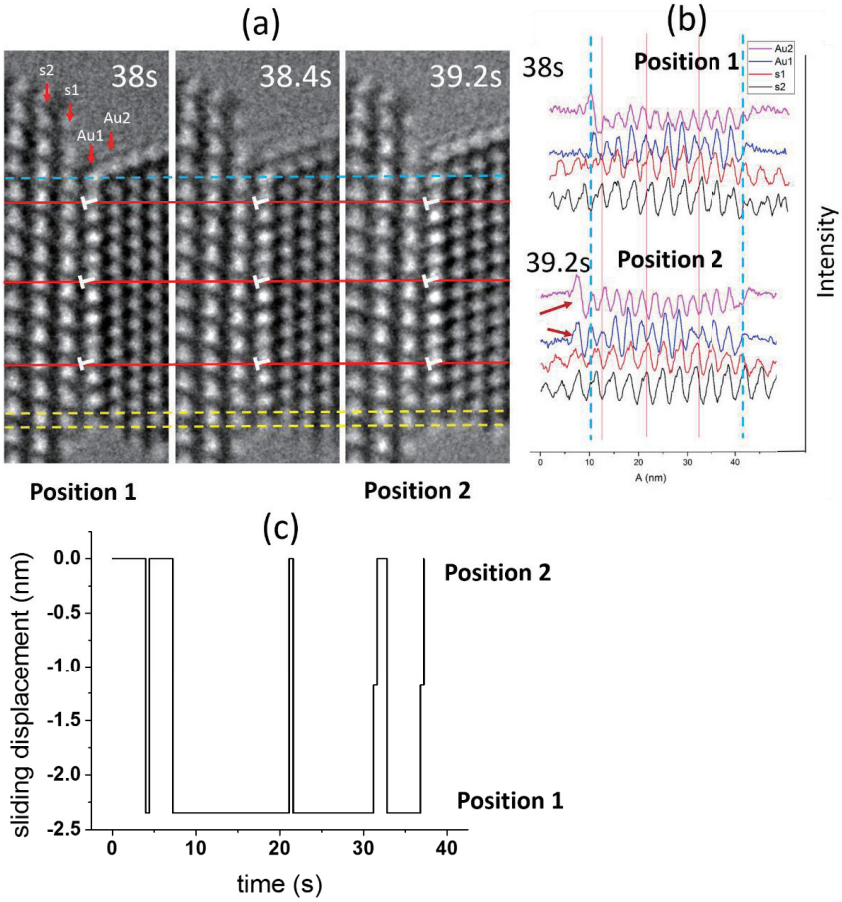

Figure 4.11 (a) Dislocation network of the interface between CeO_2 (left) and Au nanoparticle (right). The blue dashed line is the reference. The nanoparticle moves one lattice spacing upward at 39.2 s. The three red lines indicate the positions of dislocations. The interface layers are labeled s1 and Au1. The layer labeled Au2 is the second layer inside the Au particle counting from the interface, s2 is the second CeO_2 layer counting from the interface. The "T" symbol indicates the position of dislocations at the interface, where extra Au columns are present; (b) Intensity profiles of the interface layers for t = 38 and t = 39.2s are displayed. Red arrows indicate two peak appearing where no peak was previously present, meaning that the particle moves upward on the image by one lattice spacing; (c) Position evolution of the nanoparticle.

4.3.2 Layer movement by mass transport

Mass transport on the surface of nanostructures has been reported for layer-by-layer sublimation of PbSe[115], layer-by-layer growth of ZnO[116] and Tungsten growth[117]. During growth or

sublimation, mass transport via atom migration on the surface consistently in one direction results in the layer by layer growth of nanowires. However, such mass transport has not been reported on supported nanoparticles.

Figure 4.12 shows mass transport on an Au nanoparticle in a temporal sequence of HRTEM images. Within 2 s, one (111) layer at the bottom of the particle disappears from view as shown by the red arrow and a new (100) layer populated on the right corner (100) facet as shown by the blue arrow. The diffusion of atoms continues to move from the new (100) facet to the top (111) facet (as indicated by the yellow arrow). As a result, the whole particle moves laterally on the oxide substrate by 0.235 nm respect to the substrate (one (111) lattice space).

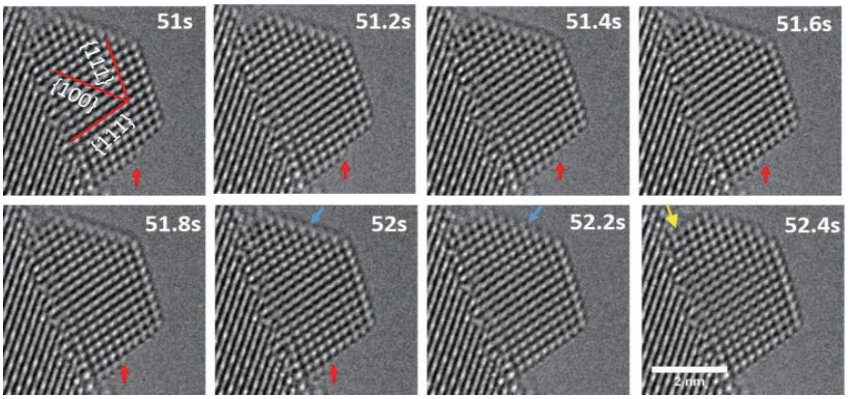

Figure 4.12 The red arrow indicates an atomic layer disappearing column by column on the (111) facet: initially the surface layer consists of six columns. The first column, which is furthest away from the interface disappears at 51.2s. The columns disappear gradually in the next frames. At 52.2s, four columns appear at the blue arrow indicated on (100) facet, two more columns show up in the next frame. Experimental conditions: room temperature, 4.5 Pa CO.

4.3.3 Rigid-body rotation

Numerous studies[118–121] have focused on the role of the interface between gold nanoparticles and metal oxide supports, because inactive gold needs to be supported on selected metal oxides or active carbon to exhibit catalytic activity[122]. Although there are few reports[105,123] focusing on the atomistic structure determination, the characterization of the interfacial structure between Au and metal oxide support is still challenging. Rigid body rotation occurs in a reversible manner during catalytic reactions[105]. Such rigid-body-motion was considered to be the result of weak interactions between gold atoms and metal atoms in the substrate, and at the same time oxygen vacancies where strong Au-metal bonds form to pin the nanoparticles, may play an important role[105].

The rigid-body rotation of Au nanoparticles on metal oxide supports are investigated in the present section by tracking a single nanoparticle. The orientation of the nanoparticle was determined using the FFT. Figure 4.13 shows an HRTEM image of an Au nanoparticle from the top view which is in [110] zone axis. It is interesting to find that the particle always in zone axis whatever the interface plane is normal or inclined to the view plane. This points out that the rotation angle can be directly determined on the FFT graph of the nanoparticle by measuring a pair of lattice spots peak. A script has been developed in-house to detect the peaks in the FFTs automatically.

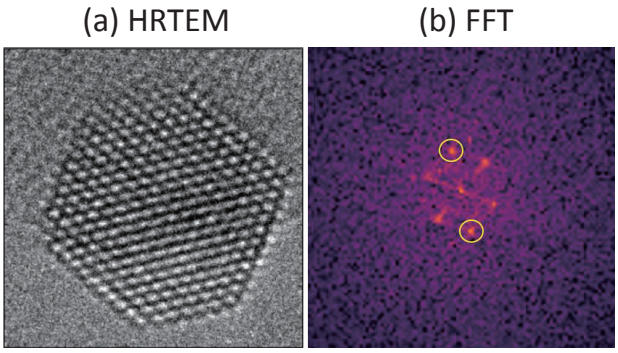

Figure 4.13 (a) HRTEM image of a top-view supported Au nanoparticle on CeO_2 with the [110] zone axis normal to the view and the corresponding FFT (b). Yellow circles indicate the spots detected for each frame. The rigid body rotation axis is also normal to the view, parallel to the [110] zone axis of the gold nanoparticle, so the nanoparticle stays in the same zone axis for all frames. The rotation angle can be determined directly on FFT.

Figure 4.14 shows two consecutive frames from the observation of an Au nanoparticle on TiO_2 with the interface showing a tilt angle of 2° around the [110] zone axis. The particle rotates back and forth on the interface with the rotation axis along with the [110] zone axis, as shown in Figure 4. 15 where the relative rotation with respect to the starting frame is shown. It is interesting that the relative rotation angle falls into two zones, Zone 1 and Zone 2. In each zone, the rotation angle fluctuates within 0.5º. The angle difference between each zone is 2º. Figure 4.16 shows another case of rigid body rotation of an Au nanoparticle where the particle/substrate interface is inclined to the [110] zone axis. The particle rotates in three zone positions indicated by yellow, green and blue boxes with the relative angle difference around 2°.

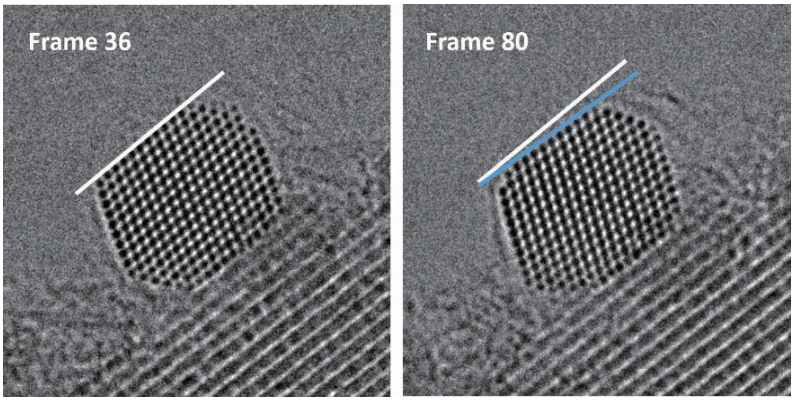

Figure 4.14 An Au nanoparticle tilts around the <110> zone axis. The white line is the surface edge reference on frame 36, while the blue line represents the surface edge on frame 80. Acquisition time for each frame is around 1.2s (exposure time is 0.5s plus 0.7s read out time). The nanoparticle rotates clockwise from frame 36 to frame 80.

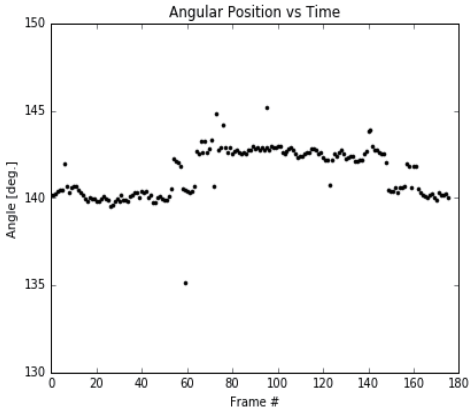

Figure 4.15 Orientation evolution of a TiO_2 supported nanoparticle under an O_2 atmosphere, where the angle is the orientation difference between the first frame and the present frame, measured using the surface edge position shown in Figure 4.14.

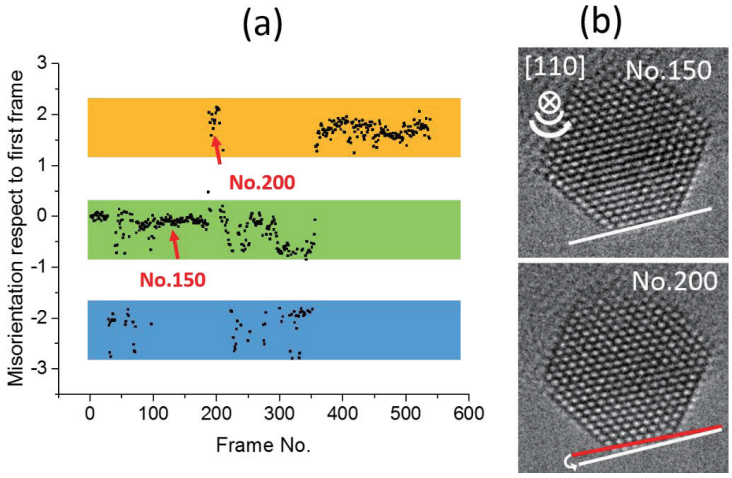

Figure 4.16 Rigid-body rotation of an Au nanoparticle on the substrate. Respect rotation angle of the nanoparticle for all frames, the first frame is the reference. Top view images with electron beam perpendicular to the interface on the right. Exposure time for each frame is 0.2 s.

4.4 Other dynamics

4.4.1 Crystallite transformation

Au nanoparticles may present a range of different geometric structures, such as bulk-like fcc arrangements, and translational-symmetry-forbidden icosahedral (Ih) or decahedral (Dh) structures[124,125]. A quantitative equilibrium phase map (structure dependence on temperature and nanoparticle size) was given by Barnard[39], based on relativistic ab initio thermodynamics and *in situ* high-resolution electron microscopy. However, the structure transformation is still under debate. Some previous reports show: (1) at or above room temperature, the decahedral morphology has been identified as the most favorable structure for 5-12 nm sized nanoparticles, and the fcc structure and decahedral morphology were stable for clusters[40]; (2) there is evidence for a decahedral to icosahedral transition at low temperature (-174 °C)[126]; (3) surface roughening is an important process above 600 °C[39]. However other *in situ* observations on the structural transformation of 6 nm Au nanoparticles do not have any order of preference[127], and any of the structures can transform from others. Most reported observations of nanoparticle structure transformations are based on clusters or nanoparticles on amorphous carbon grids in a non-crystalline epitaxial arrangement. For the application of catalysis, the nanoparticles are normally supported on crystalline oxide substrates and have an epitaxial relationships with the substrate. In this section, the $(111)_{Au}//(111)_{CeO2}$ epitaxial relationships between gold nanoparticles and CeO_2 was tracked under an electron flux of 35×10^3 $e^{-}Å^{-2}$ s^{-1}.

Figure 4.17 shows the evolution in shape and crystallographic morphology of a supported Au nanoparticle with time. During this process, the particle reshapes and the formation of a twin plane is observed. At 7.4 s, the particle begins to adopt a more spherical shape which could be

interpreted as dewetting which seems complete in the last frame. At this point the nanoparticle changes to a twinned structure which is the common structure of Au nanoparticles[46,125,127]. After 8 s, the twinning is clearly observed, the top part of the nanoparticle remains in the original structure, while the bottom part appears to have detached from the support at 30.2 s. At 32.2 s the nanoparticle still has two twins, but now the top part is detached from the support and bottom part is attached to the support in another epitaxial relationship. The results show that for nanoparticles supported on crystalline substrates, the substrate plays an important role in constraining the particles in fixed epitaxial relationships. At all times, the nanoparticle remains at least partially in an epitaxial relationship with the substrate.

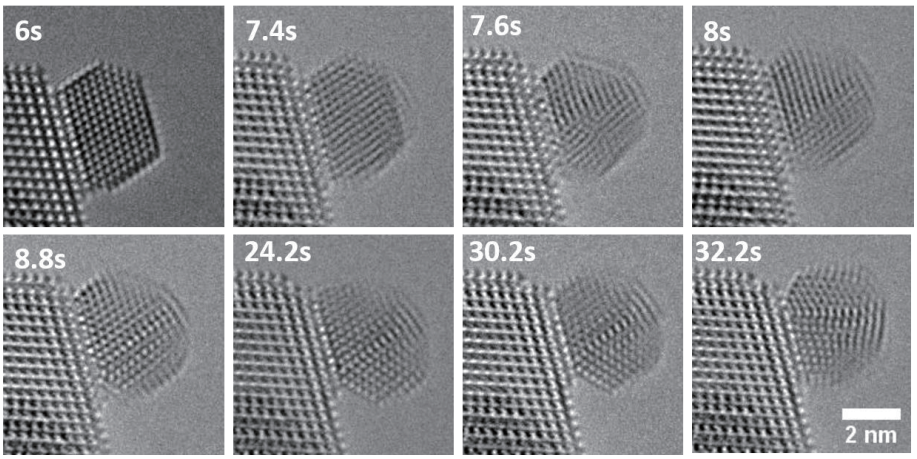

Figure 4.17 Snapshots from temporal HRTEM image sequence of an Au nanoparticle imaged at a dose rate of 35×10^3 $e^{-}Å^{-2}$ s^{-1}. The time of observation is indicated in each frame. Original structure (6 s), a transient structure (7.4 s) and a multi-twinned structure (7.6 s) are shown.

4.4.2 Orientation transformation

Nanoparticles tend to have an epitaxial relationship with substrate even during crystallite transformation. Such relationships have been extensively observed in other studies: Au (111)//TiO_2 (110) for Au/rutile TiO_2[41], Au (111)//TiO_2 (112) for anatase TiO_2[42], Au(111)//CeO_2(111)[43,44] and Au(110)//MgO(110)[128] etc. The crystal structure of oxide-supported nanoparticles directly influences their catalytic activity and stability. The substrate has been found to function mainly in two ways: 1) the oxide support is highly temperature resistant thus hindering particle coalescence; 2) reducible supports like TiO_2 and CeO_2 act as an oxygen source supplying oxygen for oxidation reactions. Typically, oxide supported nanoparticles have preferential orientation relationships with their substrates.

Rearrangement of atoms leading to the formation of twins and stacking faults has been found dating back to 1986 by Smith[129]. Low coordination number sites such as steps, corners and

kinks are considered active sites for catalytic processes, and twin boundary termination could supply stable surface steps[130]. Twins in nanoparticles are common in elements of low stacking fault energy, such as Au, Cu, etc. Furthermore, twins are also found commonly in supported nanoparticles[109,43,61]. Ceria is a good example where fundamental studies have been conducted at the atomic scale in order to understand its function as a catalyst[63]. The oxygen storage capacity of CeO_2 in catalysis, including the ability to release the surface oxygen to form oxygen vacancies in a reducing atmosphere and to capture oxygen in an oxidizing atmosphere is widely used[131]. CeO_2 is also extensively used as substrate because of its excellent thermal stability. Typically, ceria nanocrystals exhibit three low-index surfaces {111}, {110} and {100}. {111}[132] is the most stable surface with the lowest surface energy, followed by {110} and the least stable {100}, while the order of reactivity of oxygen vacancy formation is $\{110\} > \{100\} > \{111\}$.[131]

Figure 4.18 (a) shows the typical morphology of a CeO_2 supported Au nanoparticle on a model system. The shape of commercial CeO_2 support nanoparticles are normally octahedral and exhibit eight (111) surfaces. Two distinct crystalline orientation relationships between Au and the ceria support were observed. Here, these are referred to as type I Au(11-1)[101]//CeO_2(11-1)[101] and type II Au(11-1)[-10-1]//CeO_2(11-1)[101]. The planes match each other at the (111) interface planes of both Au and CeO_2. As the lattice misfit is 25%, it is difficult for both to match elastically so a dislocation network is formed to accommodate the strain that exists at the interface. As a consequence, every four (111) Au layers has an edge dislocation, as shown in the sketch in Figure 4.18(c) and (d). The distribution of these two types of relationships was measured on the as-prepared sample and was found to be 62% for Type I and 38% for type II.

In order understand more about the difference between these two orientation relationships, density functional theory (DFT) calculations have been performed using the Vienna Ab-initio Simulation Package (VASP) [1-4]. The ionic cores are described by PAW potentials[5,] and the wave functions are expanded as plane waves with an energy cutoff of 550 eV. The exchange and correlation are approximated by the PBE function, to which the aspherical gradient corrections are added. The First Brillouin zone is sampled using a 1×1×1 Monkhorst-pack grid of k points. The CeO_2 (111) surface is built using a 3×3 surface unit cell with nine atomic layers. Three atomic layers in the bottom are fixed. The Au particle is created using a 4×4 unit cell with two layers. A vacuum thickness of 15 Å is used to reduce interaction between the periodic units. Kohn-Sham formalism[6], the DFT+U approach[7] is used to describe the on-site Coulomb interaction and provides a better description of electron localization on the 4f states of the reduced cerium atoms. The low value of the U parameter (Hubbard correction) may result into electron delocalization and how large a U correction on ceria is appropriate has been discussed extensively[8-11]. Here, the value of 4.5 eV for U correction is used. The bulk equilibrium lattice constant is 5.497 Å, which is consistent with the result of Su *et al*[12]. To match the lattice of gold, the lattice parameter of ceria increases to 5.739 Å, which differs by 6% compared to the experimental value (5.423 Å) [13,14,133].

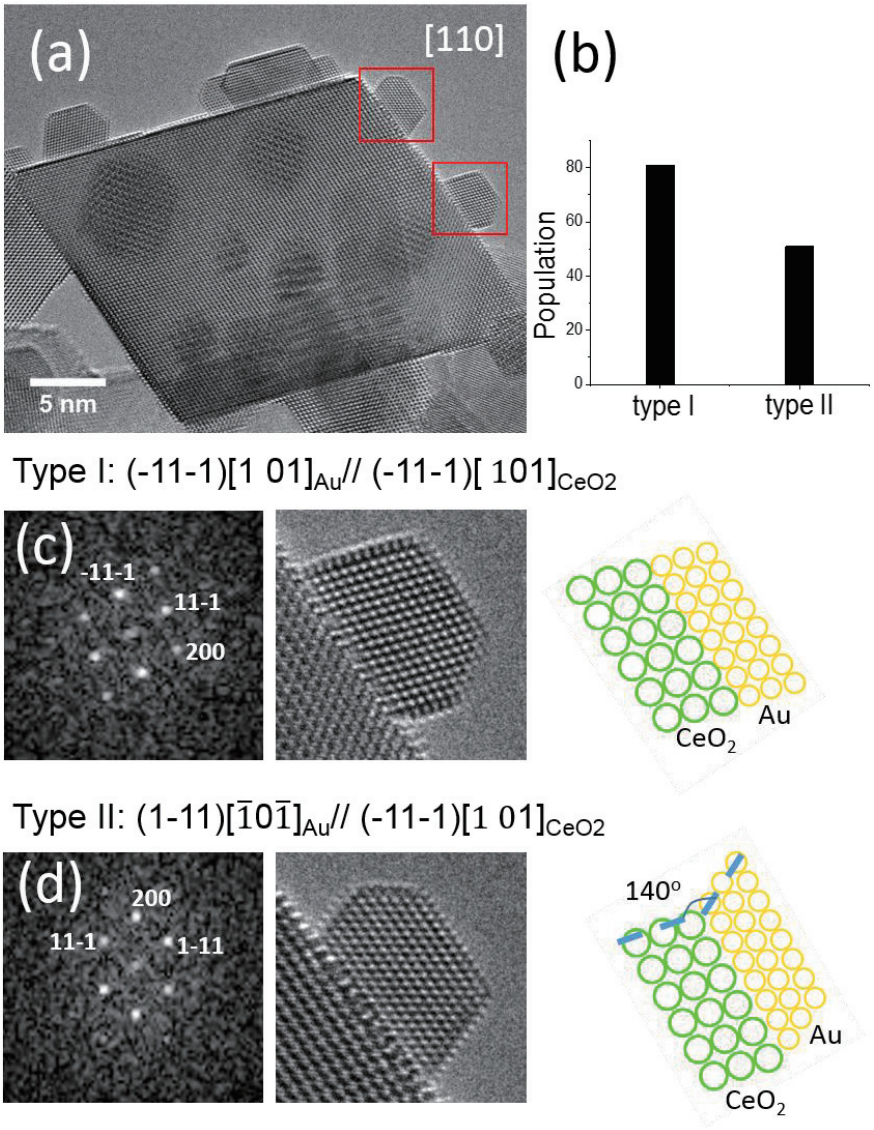

Figure 4.18 (a) Typical morphology of the as received sample. Truncated decahedron gold nanoparticles sitting on octahedral CeO_2 (111) surface. Both CeO_2 and Au are in [110] zone axis. (b) Populations of two preferential orientation structure on as-received sample. (c) Types I, Au (11-1) [101]//CeO_2 (11-1) [101]. (d) Type 2, Au (11-1) [-10-1]//CeO_2 (11-1) [101].

The system energy of the Au particle adsorbed on the pure and defected ceria surface is calculated (Figure 4.19. For pure ceria, the energies of a gold particle growing along Type 1 and Type 2 directions are very close, with an energy difference $\Delta E = E_{Type1} - E_{Type2}$ lower than

0.02 eV. For the defected ceria, nine possible structures of creating one surface oxygen vacancy (surVo) are considered for both Type 1 and Type 2 (the energy difference is shown in Figure 4.19 (d)). Figure 4.19 shows the most stable structures of surVo in Type 1 and Type 2 configurations. The most stable surVo site in Type 1and Type 2 is where three electrons localize on three nearest-neighbor cerium ions, one of which is an electron from the gold atom. The energy difference for the strongest adsorption of the gold in defected Type 1 and Type 2 is much lower than 0.02 eV. The calculated formation energy of creating an oxygen vacancy in Type 1 and Type 2 is 2.133 and 2.129 eV, respectively, which is 0.25 eV lower than the reported result 2.38 eV[12] caused by gold adsorption and lattice expansion.

Although the energies of the most stable structure of surVo in Type 1 and Type 2 are very close, for each possibility of surVo, five sites of surVo including V_1, V_4, V_5, V_7 and V_8 in Type 1 are more stable than those in Type 2. This means that a gold particle is more likely to grow along Type 1 than Type 2.

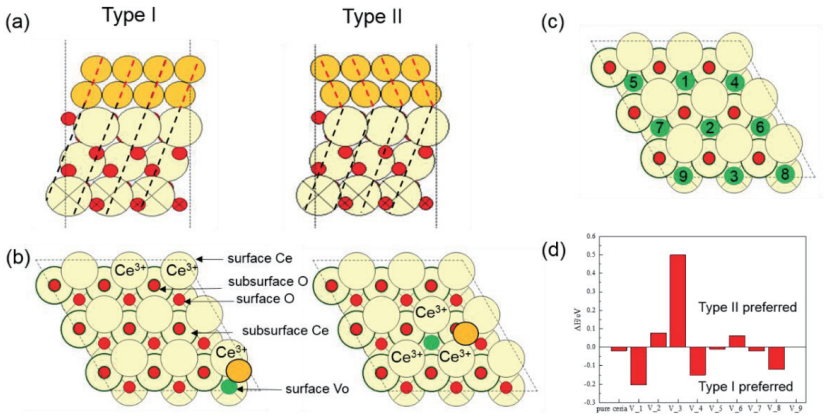

Figure 4.19 Relaxed structure of CeOx (a) the two nearest-neighbor Ce ions in the first layer are reduced (b) one nearest-neighbor Ce ions in the first layer and two symmetry equivalent Ce atoms (one in the surface and the other in the subsurface) are reduced (c) the two nearest-neighbor Ce ions in the first layer are reduced (d) the two nearest-neighbor Ce ions in the first layer are reduced.

The DFT calculations show Type I and type II have similar potential energies either on crystallographically perfect CeO_2 or oxygen deficient CeO_x. If the system is stimulated by gasous surroundings, the nanoparticle could transform between these two orientation relationships. Figure 4.20 shows the structural transformation of two nanoparticles at room temperature. Both nanoparticles became round in an O_2 atmosphere which is the typical morphological change for Au nanoparticles in O_2[62]. The structure of the top nanoparticle transforms from Type I prior to oxygen exposure (Figure 4.20 (a)) to Type II after oxygen

exposure (Figure 4.20 (d)). In the first frame in O_2 (b), the right bottom corner of the nanoparticle is more round than the top-right corner. After 2h exposure in O_2 without electron beam illumination, however, the right-top corner is more round than the bottom-right corner It seems the atoms in the two (111) facets corner (right-top) are transported to the bottom corner and the orientation of the particle changes at the same time. When O_2 is removed, the transition of the nanoparticle to Type II (d) is seen. Images (e) - (f) show the reverse process. The top half of the nanoparticle changes from Type II to Type I through the motion of the inner twin boundaries, and the twin boundaries are created between Type II and Type I crystallographic orientations.

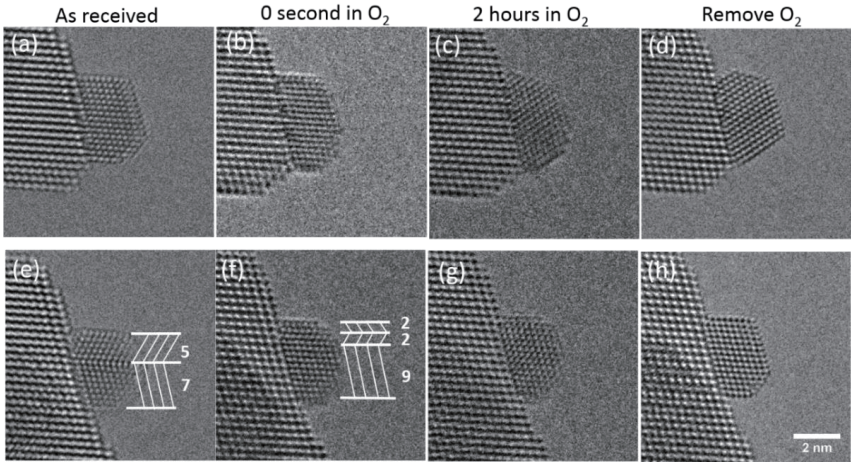

Figure 4.20 Orientation transformation in O_2 at room temperature. Top row shows an Au nanoparticle transforming from Type I to Type II, bottom row shows an Au nanoparticle partially transforming from Type II to Type I. Schematics are superimposed in (e) and (f) illustrating the direction of the (111) layer with layer numbers.

In order to obtain detailed information on the structural transformation process, a movie was acquired when studying a supported Au nanoparticle subjected to an atmosphere of 4.5 Pa O_2 at 973 K. Under these conditions, the nanoparticle changes continuously between three structural states. Figure 4.21 shows that the structural transformation which mainly occurs between the non-crystalline state (Figure 4.21 (c)) and Type I. In some cases, the nanoparticle change from non-crystalline to Type II and from Type I to Type II. However, the lifetime for Type II is much shorter compared to the other two states.

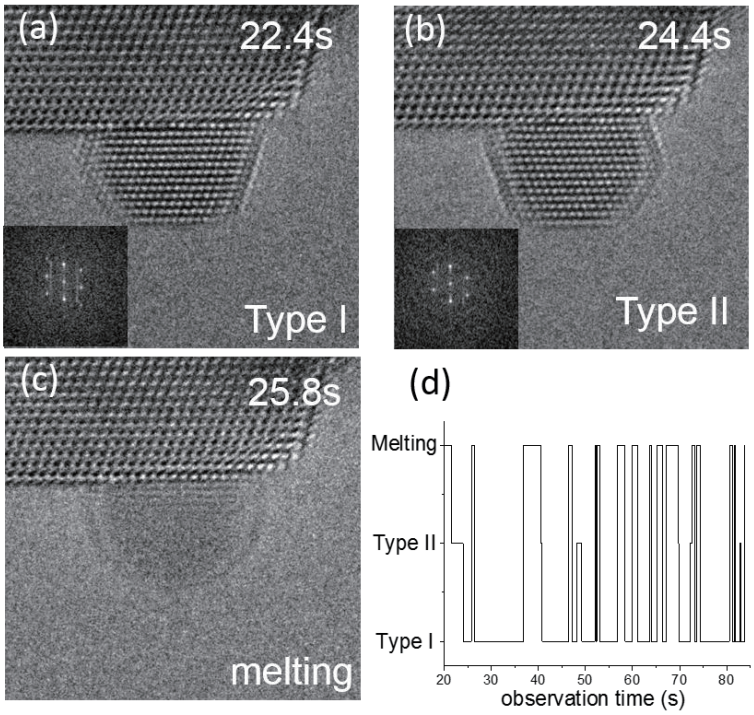

Figure 4.21 Time sequence evolution of the morphologies for a supported Au nanoparticle. Each state of morphology has been assigned an arbitrary value.

The melting point is strongly size-dependent. The melting point of a 5 nm gold nanoparticle is around 1000K[134], which is slightly higher than the temperatures used in present experiments. One possible explanation is the presence of O_2 lowering the melting point. Oxygen can lower the binding energy of metallic bonding[30]. The substrate has also been shown to affect the melting point so that the nanoparticle on substrate has a higher melting point compare to free standing nanoparticles[135]. Moreover, the effects of electron beam irradiation has to be taken into account and thus it is quite challenging to determine the exact local temperature of the nanoparticle. Despite the lower melting point observed compared with previously reported values[134], the more interesting phenomenon is the nanoparticle transitioning between several structural states as the temperature is kept constant.

At 973K transient states are also observed as shown in Figure 4.22. The lifetime of the transient states is around 0.8 s. The exposure time for each frame is 0.2 s, so the transient state is not Type I and Type II averaged over time. Although the Fourier transform of the transient states shown in Figure 4.22 exhibit both crystallographic features of Type I and Type II, the structure

of the transient states have yet to be determined. A reasonable physical model is required to understand such strange structure.

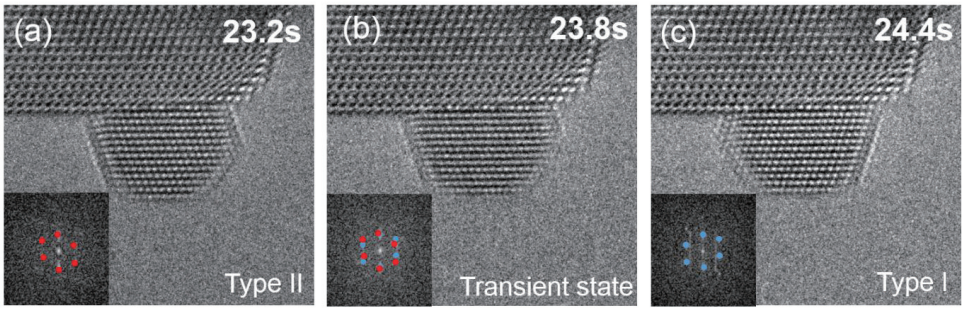

Figure 4.22 Morphology evolution of an Au nanoparticle at 973K in 4.5 Pa O_2. a) Nanoparticle is in Type II, b) transition state between Type I and Type II, c) nanoparticle in Type I. Observation time and FFT of the nanoparticle is shown on each frame.

Two transient state types have been found during the transformation between Type I to Type II. Both transient states have similar FFTs and three-layer periodic contrast features in the images as shown in Figure 4.23. However, the details of the contrast are different for these two types. The three layer periodicity of the contrast of transient type 1 is shown in Figure 4.23 (d), layer 1 and layer 2 have blurred contrast, while layer 3 has clear contrast. In transient type 2, the contrast feature is opposite, the contrast of layer 1 and layer 2 is clear, while layer 3's contrast is blurred.

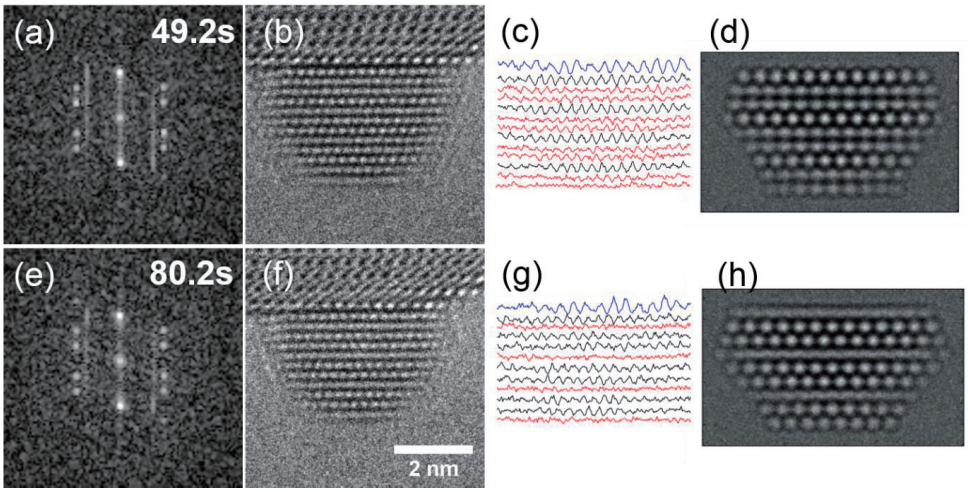

Figure 4.23 Structure detail of transition states. a) and e) Fourier transformation, b) and f) transient state images. c) and g) intensity profile corresponding to each layer of the gold nanoparticle. d) and h) simulated images.

Two preferentially orientated Au nanoparticles: type1 Au(11-1)[101]//CeOx(11-1)[101] and type 2 Au(11-1)[-10-1]//CeOx(11-1)[101] have been observed and a statistical measurement shows that type 1 is the dominant structure. Density functional theory calculations with Hubbard corrections suggest that these two types of nanoparticle have similar potential energies on a perfect ceria surface. The observation of twin boundary-associated orientation transformations of a supported Au nanoparticle in O_2 at room temperature indicates that the defects in nanocrystals may play an important role in structural transformations. Such observations may provide a valuable experimental reference for catalyst utilization and theoretical model setup.

The observation of a transformation of the orientation relationship between Au nanoparticles and the CeO_2 {111} surface demonstrates that the crystalline structure could affect the complex interface dynamics that take place. Au nanoparticles can transform between two orientation relationships, and the vacancy formation energy varies between these two configurations. These results have been verified by DFT calculations which show that the system potential energy of Type II is slightly higher than that of Type I on a perfect CeO_2 surface. However, the difference is as large as 0.2 eV when there are one or two oxygen vacancies present.

4.4.3 Contamination growth via the Stranski-Krastanov mode

As ETEM becomes a quantitative experimental technique in physical and chemical science, there are several issues to address. Among the most important are the purity of the gases used and the cleanliness of the gas delivery systems which can lead to contamination of the sample and the effect of electron irradiation. The beam effect on the surface dynamics has been

discussed in Chapter 3. The origin of contamination in ETEM could be from the high-pressure gas bottle and supply line, leakage through O rings, contamination on the sample from ambient air before being inserted into the column etc. Since the gas cylinders and supply lines are made from steel, high-pressure CO can react with the inside wall, forming corrosion products. Fe and Ni are the two most commonly reported contamination elements[64,136].

In this section, contamination growth in unpurified CO is displayed. Such observations may be of interest to reveal solid nucleation and growth mechanisms. Gas-solid growth at the atomic scale can be observed inside the ETEM leading to the possibilty of elucidating the resulting nanoparticle or thin film growth mechanisms.

Three basic growth models[137] of thin film growth are shown in Figure 4.24. Depending on the interaction energies of substrate and film atoms, any of these three growth modes can occur. In the Volmer Weber growth mode, the total surface energy of the film interface is larger than that of the substrate-vapor interface; adatoms tend to ball up, and small islands form under the condition of slow diffusion, as indicated in Figure 4.24(a). If the substrate-vapor surface energy is larger than the combined surface energies, a smooth atomic film will form and growth will occur layer by layer as shown in Figure 4.24(b). The Stranski-Krastanov mode is a combination of these two modes where growth takes place initially in layers then changing subsequently to island growth (Figure 4.24(c)).

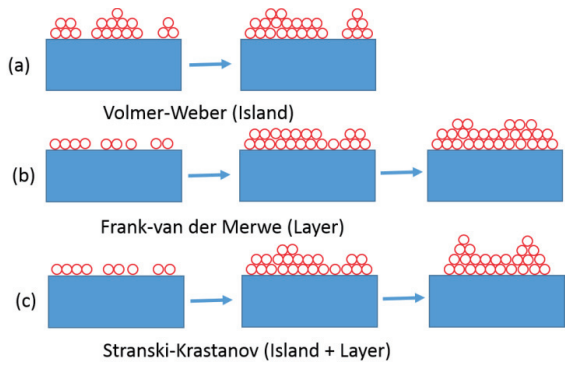

Figure 4.24 Basic modes of thin film growth: (a) Volmer-Weber modes, separated islands form on the surface of the substrate, the interaction between atoms of the film is greater than that between a substrate and the adjacent atoms of the film. (b) Frank-van der Merwe mode: layer-by-layer growth, the interaction between substrate and atoms of the film is greater than that between adjacent atoms of film. (c) Stranski-Krastanov mode: one or two monolayers form first and then growth via individual islands.

A sequence of HRTEM images in Figure 4.25A shows the Stranski-Krastanov growth of a nanoparticle on an Au nanoparticle. Initially, the adatoms diffuse on the Au surface, as indicated

by arrows at 40 s and 80 s. With more adatoms attaching to the surface, adatoms tend to ball up and a small island forms, as shown at 156 s. Afterwards, due to the interaction between Au and adatoms, the small island gradually changes to a film at 184 s, and a three-layer film is formed

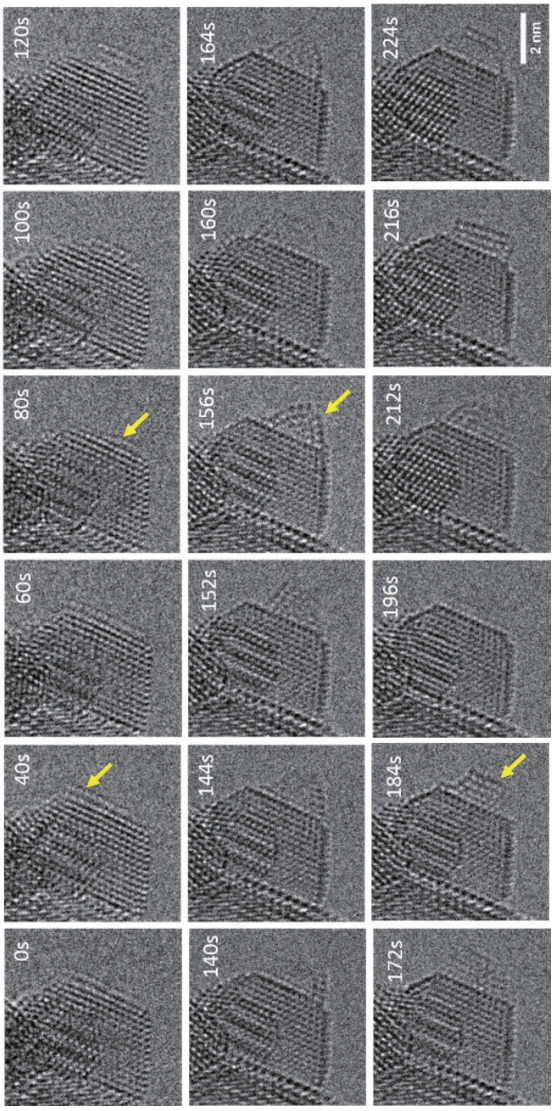

Figure 4.25 In situ contamination growth on the supported Au nanoparticle in impurity 4.5 Pa CO, the gas purifier was not used.

4.5 Summary

This chapter summarized surface and interface dynamics on a scale ranging from sub-Ångstrøm to 10 nm on a model system of Au/CeO_2 (111). These dynamics were investigated

systematically and divided into three categories based on spatial geometry; from single column hopping to layer shifting and from surface bulging to whole particle sliding. Surface atom diffusion is observed under most conditions and normally reversible. Under some conditions, the diffusing atoms on the surface move in a concerted manner: atoms in the same layer shifting in the same direction at the same time or disappearing-reappearing at the same time. Such concerted and reversible behavior of a group of atoms suggests there are a variety of configurations which can be considered as local minima in potential energies in configurational space.

Chapter 5 Dynamic Surface Effects of Gas and Temperature

The chemical environment and temperature leads to significant changes in morphology and structure of gold nanoparticles. An equilibrium phase map of gold nanoparticles with the consideration of temperature and pressure has been proposed by Amanda[39]. However, the non-equilibrium dynamic response of the nanoparticles under operational conditions which is essential in order to understand the behavior of the nanoparticles in their working state.

This chapter is devoted to investigating how the local environment influences the interface dynamics at both the gas-nanoparticle and the nanoparticle-substrate interface. By varying gas species and/or changing temperature, surface dynamics of nanoparticles are investigated at the atomic level. Particular attention is given to atomic morphology transformations and atom column hopping of Au nanoparticles by means of atom column detection on sequential images. In this way, quantitative measurement of atomic column diffusion on large datasets (thousands of images) is carried out and surface dynamics are evaluated at the atomic column level (as opposed to nanometer-scale evaluation of the morphology of whole nanoparticles[62].

Surface atom layer appearance-disappearance is investigated in different gases and temperature ranges. The kinetics of layer appearance-disappearance are analyzed in CO and H_2. At the same time, atomic-scale reversible twinning processes are investigated by temporal HRTEM sequences as well as strain mapping and twinning. All these factors are important in the particle synthesis process and can control the final shape and facet exposure of the Au nanoparticles[46,127]. Additionally, the formation of twinning can occur under reactive or reaction conditions[63,109].

5.1 Equilibrium shape of nanoparticles in gases

A crystalline nanoparticle usually exposes planar facets at low temperatures, as steps and kinks (under-coordinated sites) are energetically expensive. Traditionally, the Wulff criterion has been employed to predict the equilibrium shape of free-standing particles[138]. For particles grown on a substrate, the shape is truncated by the substrate. Assuming the height of a free-standing particle is H and that of a particle grown on a substrate is h, the truncation ratio (h/H) depends on the interface energy via the Winterbottom construction[139] as shown in Figure 5.1.

Moreover, the interface energies have a strong dependence on the environment meaning that the nanoparticles have different truncation ratios under different conditions. Further, the surface free energies of different Miller index facets vary depending on gas species and pressure, for example Au nanoparticles tend to extend under oxidation conditions and to contract under reduction conditions[109]. During the course of the development of nanoparticle models, the theoretical calculations to predict equilibrium atomic shapes have taken into consideration the

size of the nanoparticles[138], the adsorbate influence[100] and support constraints[100]. However, the shape of nanoparticles has a strong dependency on the environment. The morphology change of CeO_2 supported Au nanoparticles induced by the surrounding environment has been reported by Takeda *et al.*[62,140,141]. During the process of CO oxidation in a CO/air mixture, O_2 molecules are dissociated into oxygen atoms or active oxygen-related species by the catalyst, thus inducing the formation of rounded or fluctuating multifaceted surfaces of gold nanoparticles and the surfaces show dynamic behavior at the same time[62].

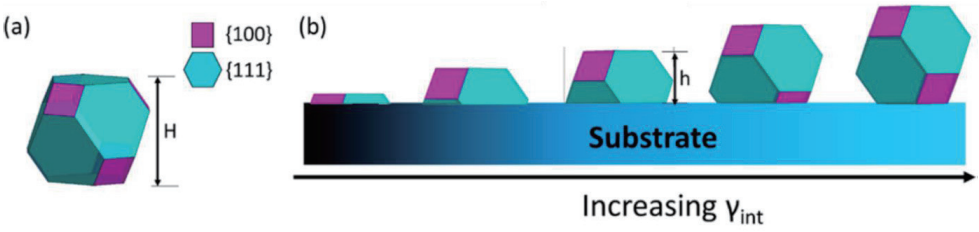

Figure 5.1 (a) Illustration of the Wulff construction of an Au particle and (b) Winterbottom construction of Au nanoparticles supported by a substrate with different interface energies. Reproduced from[109].

Quantitative evaluation of the shape of Au nanoparticles with diffusing surface atoms is challenging. Here, the time averaged shape is adopted to quantify the morphology transformation induced by the gases. Supported Au nanoparticles are tracked in different gases at room temperature. The average projected atomic morphology and the surface facets of these particles exhibiting dynamics such as atom column diffusion was recorded using HRTEM. Figure 5.2 shows the time-averaged morphologies of a supported Au nanoparticle in different gases at room temperature. Each facet has been assigned a letter from A to D. The number of columns of each facet is listed in Table 5.1. The number of surface columns on different facets and the total number of projection columns changes in response to different gas environments.

The detailed practical experimental procedures for the study of surface dynamics are as follows. 1) record an image sequence under high vacuum conditions in order to obtain the reference information such as particle morphology and the number of columns on facets; 2) close the microscope column valves, introduce O_2 into the column and allow it stabilize for 30 min; 3) record the image sequences with similar dose rates for the HVAC condition in step 1); 4) pump O_2 out of the column. The same procedure was applied when using H_2 gas. The reason for recording the Au nanoparticle movie at room temperature under high vacuum conditions is to obtain a reference. Electron beam irradiation inevitably induces diffusion of Au atoms, even in the absence of gaseous environments. Based on these image sequences, the atom column occupancy is determined using a neural network method instead of by manual detection (human) as applied in Chapter 3. An example of the column detection results is shown in Figure 5.2. The columns are assigned as 'occupied' if the detection probability is higher than 50%, otherwise they are assigned as 'unoccupied'. The column occupancy is detected by the neural network method on single frames from sequences as shown in the middle row of Figure 5.2. The shapes

of nanoparticles are also examined on the occupancy maps where the average of all frames in the sequences are taken into account.

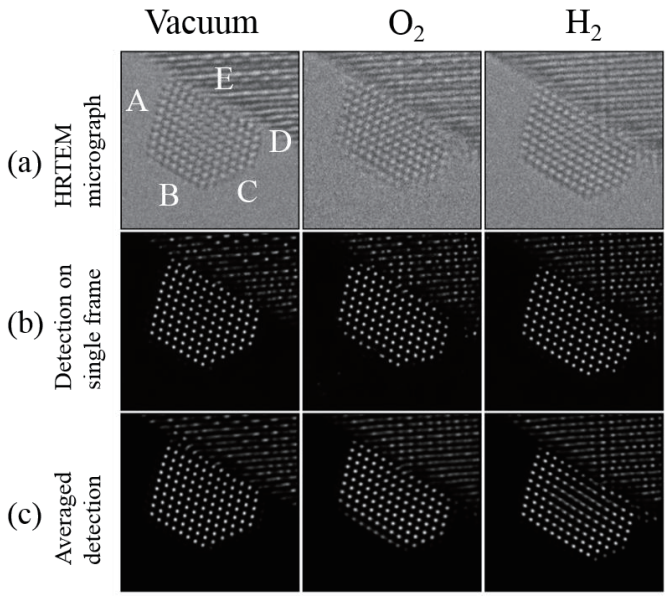

Figure 5.2 Equilibrium shape of a supported Au nanoparticle exposed to different gases, (a) Experimental HRTEM image; (b) Neural network column detection on a single frame; (c) Neural network column detection averaged over frames. 300 frames for HVAC, 267 for O_2, 477 for H_2. The dose rates are 4.1, 1.6, 2.1 and 1.1 $\times 10^3$ $e^-/Å^2$ s^{-1} for HVAC, O_2, and H_2 respectively. Gas pressures of O_2 and H_2 are 4.5 Pa. The residual pressure in the column is around 1×10^{-5} Pa. The images were acquired at room temperature. The exposure sequence is HVAC, O_2 then H_2. After each exposure, the gas was evacuated to a pressure lower than 5×10^{-5} Pa. The new gas was introduced and allowed more than 30 min to stabilize prior to image acquisition. The view direction is along the [110] axis.

	A(-111) height	B (1-11)	C (001)	D (-111)	E (Interface column)	Total projection columns
HVAC	10	8	6	5	13	105
O2	8+1	11	4	5	14	111
H2	9	10	5	5	14	106
CO	8	11	4	5	14	106

Table 5.1 Number of surface columns in different facets and total projection number of the columns under different gas environments. The facets corresponding to A, B, C and D, are labeled in Figure 5.2.

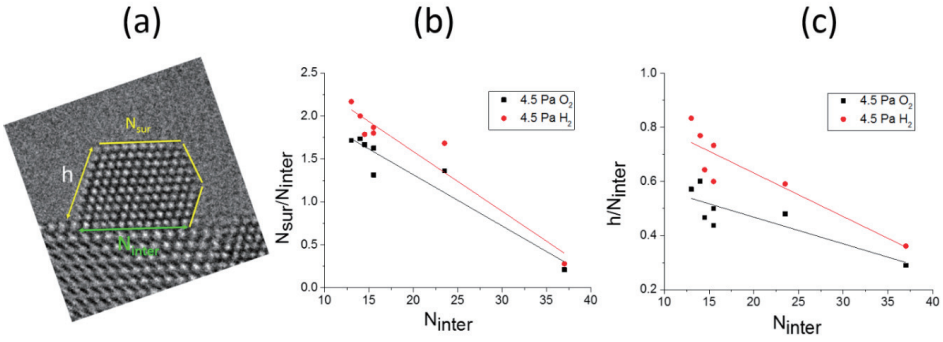

Figure 5.3 (a) Number of surface columns versus number of interface columns (b) height/interface ratio as a function of the number of interface columns in O_2 and H_2, (c) the number of surface columns/interface columns ratio as a function of the number of interface columns in O_2 and H_2.

Seven nanoparticles (six shown in Appendix B) have been exposed and tracked in 4.5 Pa O_2 and 4.5 Pa H_2 respectively. As shown in Figure 5.3 a), the number of surface columns (indicated by yellow lines) and the number of interface columns (indicated by the green line) are counted, where h represents the height of nanoparticles parallel to {111} planes. The surface columns /interface columns ratio and the height/interface ratio (where the number of interface columns is used as the diameter of the nanoparticle) have been displayed as a function of the number of interface columns as shown in Figure 5.3 (b) and (c). Both the height/interface ratio and the

surface/interface ratio are lower in O_2 than in H_2 for all seven particles, indicating that the particles have a larger interface area in O_2 where particles wet the substrate surface.

Oxidative or reductive gases influence not only the interface energy but also the surface energy. The nanoparticle has 5 columns in facet C ((001) facet) in O_2, while only 4 columns in H_2 as shown in Table 5.1. The difference in the number of columns under these conditions suggests that the surrounding gas environments can tune the surface energies and that the (001) atom facet is more sensitive and reactive to changes in the surrounding environment. So, the nanoparticle has different equilibrium shapes in different gas environments.

5.2 Quantification of adsorbate-induced surface atom mobility at room temperature

Surface column diffusion has been quantitatively evaluated by the column occupancy percentage and hopping event frequency. Figure 5.4 shows the neural network detection results on HRTEM images in O_2 at different times. Due the surface diffusion, the number of columns in the first layer varies with time.

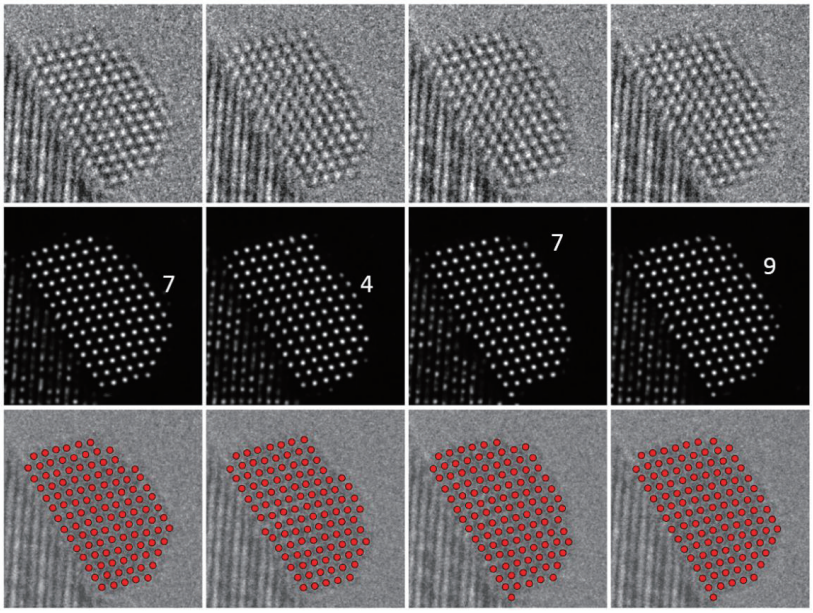

Figure 5.4 Snap shots of HRTEM sequential images, which are chosen every 10 frames. The first row shows the original HRTEM frames, the second row is the neural network output for a potential occupancy of the columns, and the last row shows where the probability of occupancy is higher than 50%. The exposure time is 0.2s per frame; the movie was recorded in 4.5 Pa O_2 with a dose rate of 1.6 $\times 10^3$ $e^-/Å^2$ s^{-1}.

The occupancy percentage is the percentage of frames where the neural network has identified an atomic column. This is indicated by a color-coded dot in Figure 5.5 (b). The occupancy

percentage ranges from 0 to 100 % according to the color code. Atom diffusion induced occupancy changes are defined as a "column hopping event". The term is used for both an occupied column change to unoccupied and an unoccupied column change to the occupied state. The hopping events are counted for each atom column and presented by color-coded dots in Figure 5.5 (c).

Figure 5.5 (b) shows how the column occupancy percentage varies in different gas environments. In high vacuum, most of the columns are fully occupied (yellow) excluding some atom columns at the interface. In O_2, atom columns on facets B and C have a lower occupancy percentage compared to internal columns. In H_2, the occupancy percentage map is similar to that that in high vacuum where most atom columns are fully occupied with only some columns partly occupied at perimeter sites and on facet C. The hopping event frequency shown in Figure 5.5 (c) shows that hopping is more likely in in O_2 than in H_2.

The combined information of the occupancy percentage and hopping event frequency clearly shows that surfaces of the nanoparticle in O_2 are much more active than in H_2. It is interesting to find that facets show similar hopping behavior in O_2 with active facets B, C, D and an inactive facet, A. Hopping was only observed at C facet in H_2.

A possible explanation for the higher hopping frequencies observed in O_2, could be the desorption temperature of the difference gases, e.g. hydrogen and deuterium molecules have been found to desorb from Au at 120 K[38]. Chemisorbed atomic O has a much higher desorption temperature in the range from 415K to 650K[30,32] depending on the oxygen species. The details have been shown in Table 1.1.

The experiments in this section were carried out at room temperature (300K) which means that there can be atomic O on the Au nanoparticle surfaces and that no, or very little, H_2 is adsorbed. The significantly higher frequency of surface atom activity in O_2 is corresponds to oxygen adsorption on the Au nanoparticle surfaces.

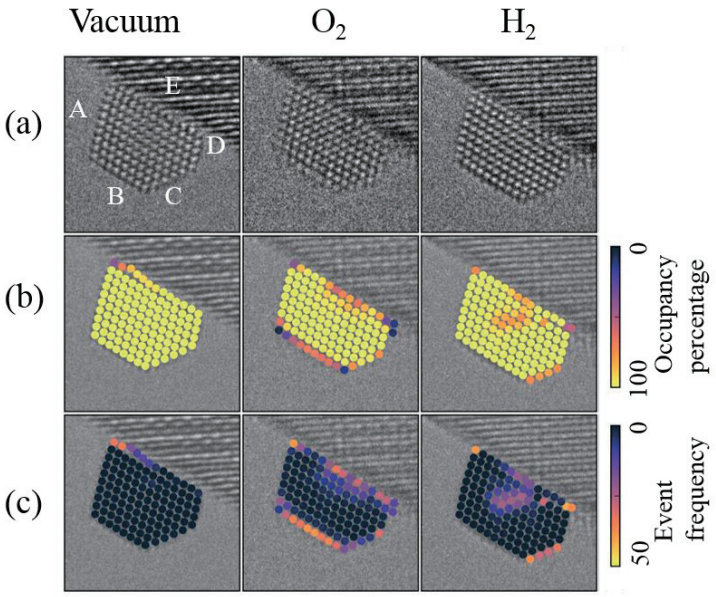

Figure 5.5 Quantification of surface atom column hopping in different gases. (a) Experimental images. (b) Color-coding of occupancy referring to the frame percentage in all the frames of the sequence. (c) Event frequency representing the hopping event percentage, where the highest percentage of 50% signifies the hopping event occurred in every second frame. The lower the event percentage, the lower the frequency of the hopping event. The dose rates are 4.1, 1.6, 2.1 and 1.1 $\times 10^3$ $e^-/Å^2$ s^{-1} for HVAC, O_2, and H_2 respectively. Gas pressures of O_2 and H_2 are 4.5 Pa. A, B and D indicate (-111), (1-11) and (-111) facets, C indicates (001) facets, and E indicates interfaces.

In order to understand the surface dynamics of Au nanoparticles in O_2 and H_2, the averaged strain mapping of the nanoparticle is shown in Figure 5.6. The strain coordination of each column corresponds to two nearest neighbor shells (four nearest neighbors and two next-nearest neighbors). The parallel strain at the interface layer is mainly contraction strain, i.e. crystalline accommodation via the epitaxial relationship, Au {111} // CeO_2 {111}. A dislocation network (see Figure 4.11) is created at the interface to reduce the large elastic strain caused by the large difference in the lattice spacing: 0.235 nm and 0.312 nm for $\{111\}_{Au}$ and $\{111\}_{CeO2}$, respectively, and between two neighboring interface dislocations, four Au {111} layers match three CeO_2 {111} layers. As a consequence, the distance between two interface dislocations on the Au side is 0.004 nm larger than that on the CeO_2 side, resulting in a contraction strain on the Au side. However, the detailed local contraction strain along the interface also depends on the local interface atomic structure and the gaseous environment.

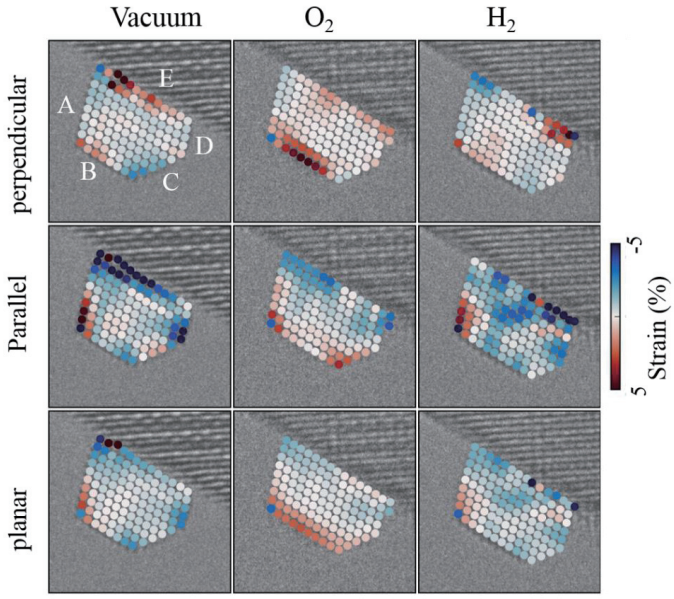

Figure 5.6 Averaged strain mapping of an Au nanoparticle in HVAC, O_2, and H_2. The perpendicular strain is the strain perpendicular to the interface, the parallel strain is the strain parallel at the interface, and the planar strain is the average of the two.

In high vacuum, minor expansion strain is observed in the perpendicular direction and contraction strains in the parallel direction on the surface of the nanoparticle. This could be caused by surface relaxation. Atoms in the outermost layer have a low coordination number, and the electronic density of states is lower for these columns. As a result, atoms tend to relax perpendicular to the surface, and at the same time contract in the parallel direction.

When the nanoparticle is exposed to 4.5 Pa O_2, the top surface layer on facet B tend to expand in the perpendicular direction. There is no significant strain on the other facets in this direction. In the parallel direction, the atom columns at two corners (A-B and B-C) show expansion strain and the bottom half of the particle shows column contraction strain. To sum up, the nanoparticle has expansion strain at the top two layers and small contraction strain for the bottom layers close to the interface in planar. This distribution can be directly connected to hopping events at the top (1-11) layer on facet B (see Figure 5.5).

In H_2, the particle has a similar strain field as in high vacuum. Only the corner and perimeter sites show some expansion strain. It is very intriguing that the active atom sites are coincident with locations where the larger strain fields exist, either expansion or contraction. The conclusion is that large local strains influence the atomic diffusion and vice versa.

5.3 Atomic layer appearance-disappearance

Layer appearance-disappearance has been observed on Au nanoparticles and was discussed in Section 4.2.4. In this section, more detailed cases of atomic layer appearance-disappearance influenced by the environments such as the gases and temperature will be discussed.

5.3.1 Dynamical (100) atomic layer appearance-disappearance in CO

Thermally-activated dynamic (100) atomic layer appearance-disappearance has been observed in a CO atmosphere in the temperature range from 200°C to 300°C as shown in Chapter 4. The supported gold nanoparticle typically has a truncated octahedral shape truncated by (111) and (100) facets. The interface between CeO_2 and the Au nanoparticle is $(111)_{Au}$ // $(111)_{CeO2}$.

Movies to investigate the surface dynamics were recorded by time-resolved HRTEM (Figure. 5.7). The number of columns on the truncating facets are labeled on the image. For example, at 76 s, the nanoparticle has a configuration of 10×8×5×6, where the numbers refer to the number of atomic columns on each facet. The atomic configuration changes to 10×9×4×7 at 78.2 s. This atomic configuration transformation is reversible: the atomic configuration transforms to 10×8×5×6 at 80.4 s and to 10×9×4×7 again at 81.8 s.

The difference between the above two configurations is an additional (100) atomic layer, as indicated by red arrows in Figure 5.7. The corresponding intensity change during the formation of the (100) atomic layer observed by HRTEM at different times has been analyzed and is shown in Figure 5.8. The colored intensity profiles presented in c) correspond to the same colored boxes on the images, and the blue intensity line represents vacuum as the reference intensity. The black and blue intensity lines have similar contrast indicating that at 204.8 s the layer bounded by the black box is empty, while the red intensity line shows a significant contrast increase compared to the reference blue line indicating the formation of a new (100) layer at 205.2 s.

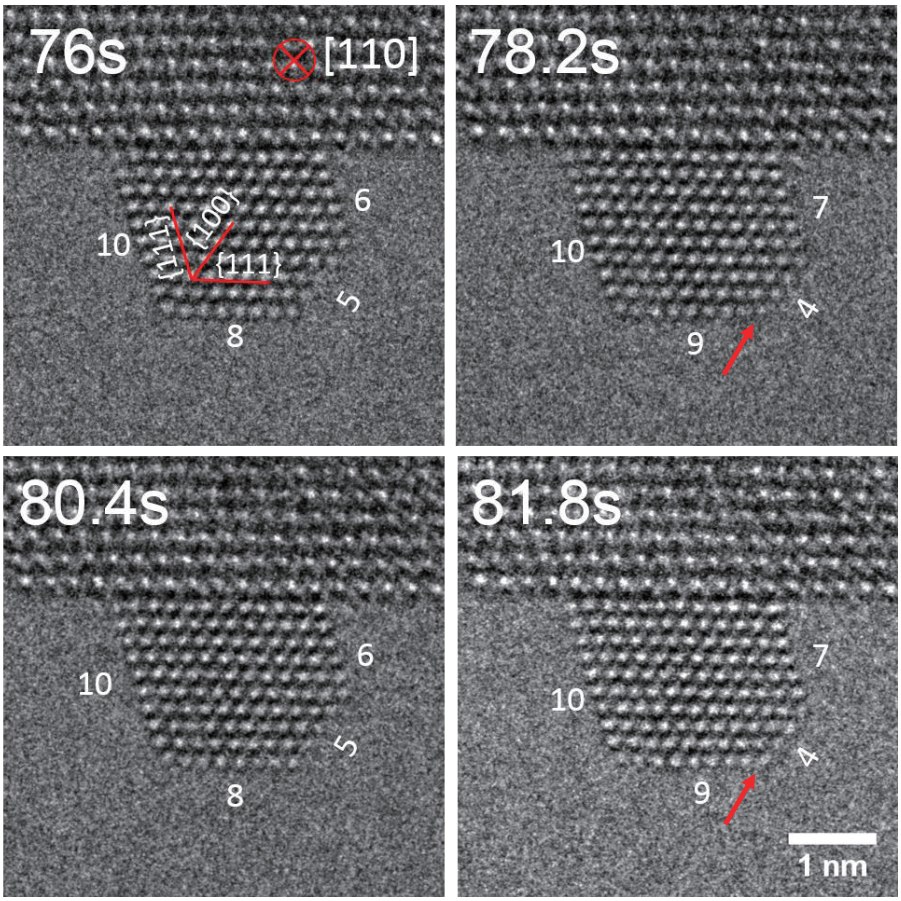

Figure 5.7 Time-resolved HRTEM images of a supported Au nanoparticle with a (100) surface layer appearance-disappearance oscillation in 4.5 Pa CO at 250 °C. The atom arrangement of the particle varies between two configurations 10×8×5×6 (76 s, 80.4 s) and 10×9×4×7 (78.2 s, 81.8 s).

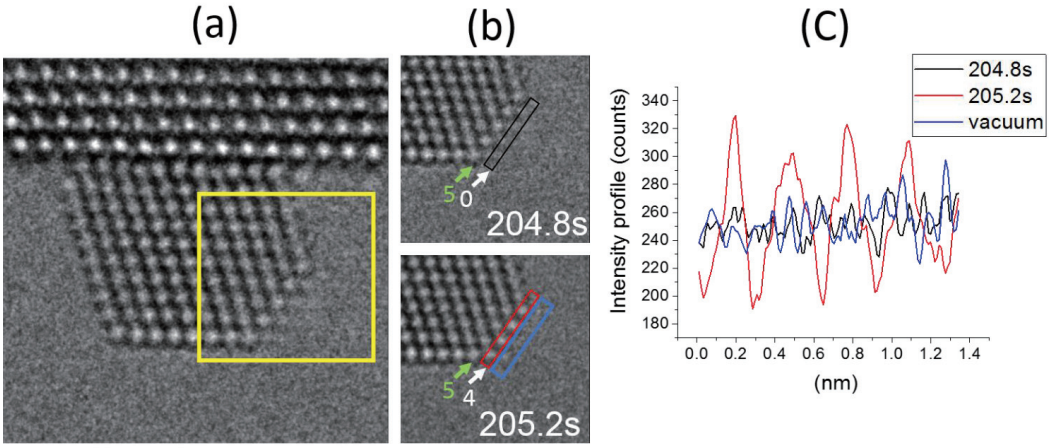

Figure 5.8 (a) CeO_2 supported Au nanoparticle, (b) Cropped corner micrographs of the nanoparticle at different times where the number of atom columns in the layer is indicated, and (c) Intensity profiles produced by the layers bounded by the colored boxes in (b). The yellow area in a) is enlarged in (b) at different times. In (c), the black and blue intensity profiles have similar contrast; the blue plot is an intensity reference in vacuum; the red intensity profile has significantly higher contrast compared to the black and blue lines. Experimental conditions: 0.2 s exposure time per frame, 4.5 Pa CO at 250°C.

In order to investigate the atomic layer appearance-disappearance kinetics, the intensity profiles of this fluctuating layer at different times have been extracted from the images and stacked in a time sequence, as shown in the top image of Figure 5.9. The contrast evolution of the four atom columns in this layer are the four rows in Figure 5.9. The intensity profile of a column (red line) in time is displayed on the plot beneath the image along with an intensity profile (black line) in vacuum for reference. The peaks in the red line indicate the appearance of the atom column. It should be noted: 1) the four columns with the fluctuating layer behave in a concerted manner since the four rows in the image have similar contrast features; 2) such an appearance-disappearance fluctuation is not ideally periodic, and the width of the peak of the red intensity profile varies with time.

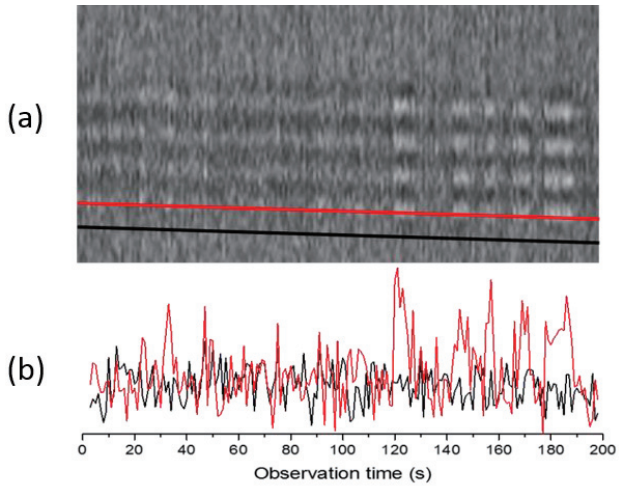

Figure 5.9 (a) Time evolution of the outmost layer intensity. (b) Black lines represent the vacuum reference intensity profile while red lines the position and intensity evolution of an atom column.

5.3.2 (100) atomic layer appearance-disappearance in H_2

(100) atomic layer appearance-disappearance was also investigated in H_2 and is shown in Figure 5.10. At 3.2 s, the atom configuration is 6×5×11×10, changing to 5×6×10×10 at 4.4 s. The atom configuration reverses back to 6×5×11×10 at 9.6 s and changes to 5×6×10×10 again at 24.8 s.

Figure 5.11 shows the configuration evolution at 300°C and 350°C. The lifetime of the configuration 6×5×11×10 (corner (100) disappeared) is shorter than the 5×6×11×10 configuration at both temperatures in the investigated periods. At 350°C, the lifetime of 6×5×11×10 configuration is even shorter than that at 300°C, suggesting that the potential energy of this configuration varies with temperature.

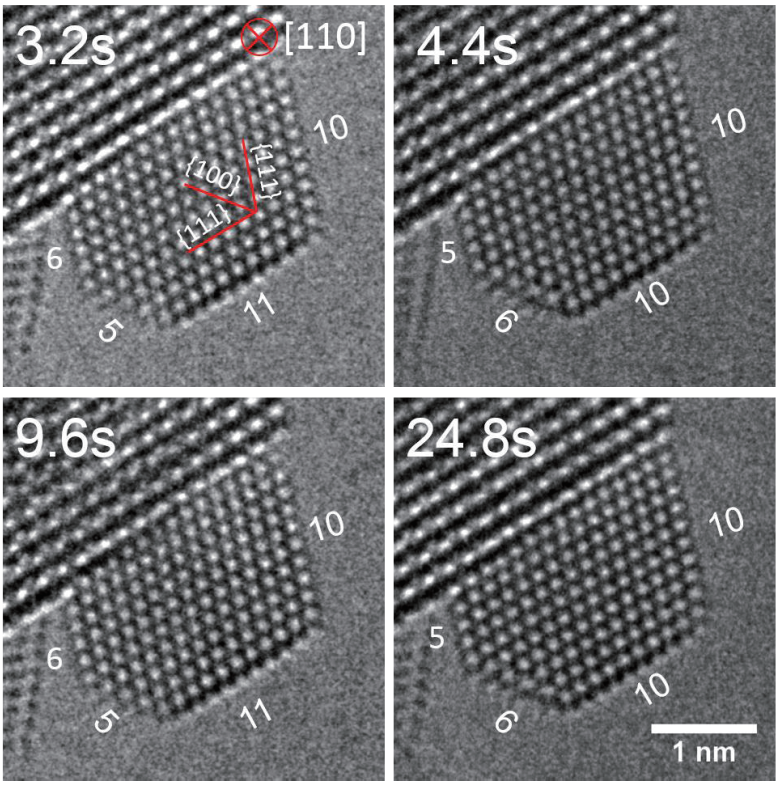

Figure 5.10 Supported Au nanoparticle truncated by three (111) facets and one (100) facet. The number of columns in each surface facet has been counted and labeled accordingly. The atomic arrangements of the particle varies between two configurations 6×5×11×10 and 5×6×10×10.

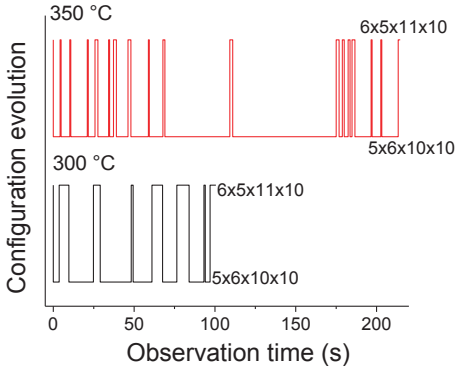

Figure 5.11 Variation of nanoparticle atomic configuration as a function of time at different temperatures.

5.3.3 (111) atomic layer appearance-disappearance fluctuation in O_2

Figure 5.12 shows that layer appearance-disappearance also occurs on the (111) atomic facet in 5.5 Pa O_2. At 61 s, the height of the nanoparticle changes from 16 layers at 61 s to 15 layers at 61.2 s. At 62 s, the height changes back to 16 layers and again to 15 layers at 63.8 s. The same phenomenon has been found on another four nanoparticles in O_2.

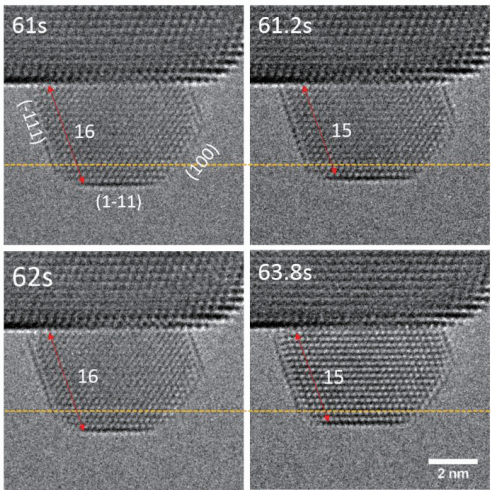

Figure 5.12 Surface (111) layer appearance-disappearance in 5.5 Pa O_2 at 700°C.

From the observation shown above, several preliminary conclusions can be drawn as follows: 1) atomic layer appearance-disappearance of the nanoparticles was only observed at moderate temperature, such as 250°C in CO, 300 - 350 °C in H_2 and 450 - 700°C in O_2. 2) All the cases in CO and H_2 occurred on the (100) facet, and most cases in O_2 occurred on the (111) facets. It is essentially a thermodynamically driven process, but the surrounding gas environments interact in different ways on (111) and (100) atomic facets.

5.4 Dynamical atomic twinning structures of supported Au nanoparticle

For fcc nanocrystalline materials especially with low stacking fault energy such as gold and silver[45,125], twinning plays an important role in determining the structure, size, and morphology of nanoparticles. Two general types of twinning have been reported in nanoparticles[46]: parallel and cyclic. In the case of parallel twinning, the parallel lamellar repeats continuously one after another, whereas cyclic twinning requires nonparallel coplanar planes; here a complete circle is formed which restricts growth in the radial direction, leading to, for instance, a five-fold symmetry structure.

The most commonly observed structures of Au nanoparticles are shown in Figure 5.13: octahedal (a) and (b), icosahedral (c), decahedral (d), and Marks decahedral multiply-twinned nanoparticles (MTPs) (e)[46,125] . An octahedral particle is a single crystallite. The icosahedral structure, forms by a junction of 20 tetrahedral with a common vertex and three twin boundaries each. Similarly, the decahedral structure can be described as the junction of five tetrahedral single crystals with twin-related adjoining interfaces.

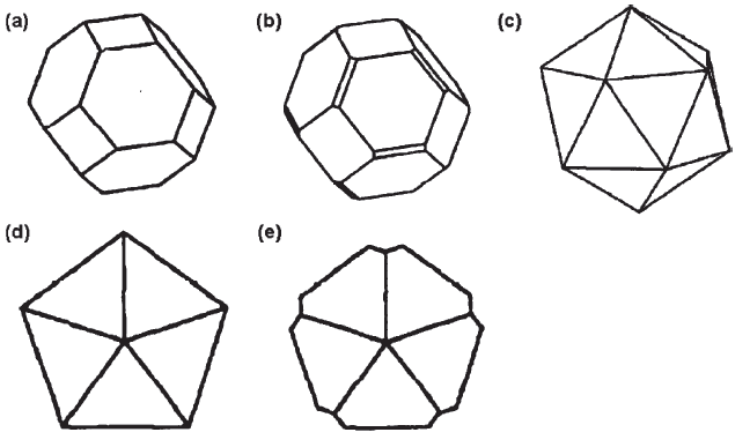

Figure 5.13 Common morphologies of small metal nanoparticles: (a) truncated octahedron, (b) truncated octahedron with extra (110) truncations, (c) icosahedron, (d) regular decahedron, and (e) Mark's decahedron. Reproduced from[46].

In the case of supported nanoparticles, a systematic investigation of dynamical twinning process is still missing in the literature. In this section, three twinning types and the dynamical twinning process of supported nanoparticles have been investigated by means of time-resolved HRTEM. The twinning orientation and reversible twinning process suggest a strong crystalline constriction between oxide substrates and nanoparticles.

Figure 5.14 shows three observed types of twinning. The green arrows represent the normal directions of twinning planes. For purposes of the discussion that follows three cases of twinning, A, B, and C are considered. In cases A and B, the twin planes are parallel with the interfaces between Au nanoparticles and the oxide substrate. In case A, a twin forms on the surface of the nanoparticle indicated by a yellow line with three layers. In case B, a twin forms close to the interface between the nanoparticle and its substrate with three layers. In case C, the twin plane intersects the interface where the new twin of 8 layers is indicated by the yellow line.

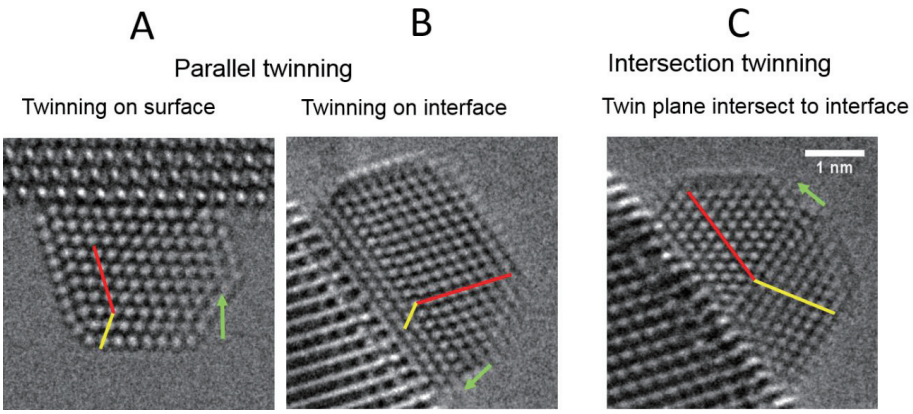

Figure 5.14 Different twinning types in oxide supported Au nanoparticles. The red line is the original atom arrangement direction, the yellow line is the atom arrangement direction of the new twins, and the green arrow is the normal direction of the twin planes. A Twinning occurring near the surface of the Au particle, B twinning occurring near the interface between the Au nanoparticle and the CeO_2 substrate. The twin planes for both A and B are parallel with the interface. C Twinning with the twin plane intersecting the interface.

5.4.1 Reversible dynamic twinning and its stability

The content of reversible dynamical twinning and its stability is connected with Section 4.2.3 where concerted layer shifting has been observed. In that case, only columns in the topmost layer shift and introduce a mismatch between the shifted topmost layer and other layers. To understand the nucleation and kinetics of parallel and intersection twinning in terms of cases A, B, and C, time-resolved HRTEM images have been taken

For case A, three states of the atom arrangement have been recorded and are shown in Figure 5.15. In (a) and (c), the atoms in the top three surface layers parallel with the interface arrange in a different direction from the atoms in the other layers. Yellow and red lines indicate these two directions and configuration 2 refers to such kind of atom arrangements. In (b) and (e), atoms are arranged in the same direction as the original single crystalline nanoparticle, referred to as configuration 1. In (d), the blurred contrast of two atomic layers indicated by blue arrows indicates that the atoms move during image recording and that the motion of atoms causes this blurred contrast.

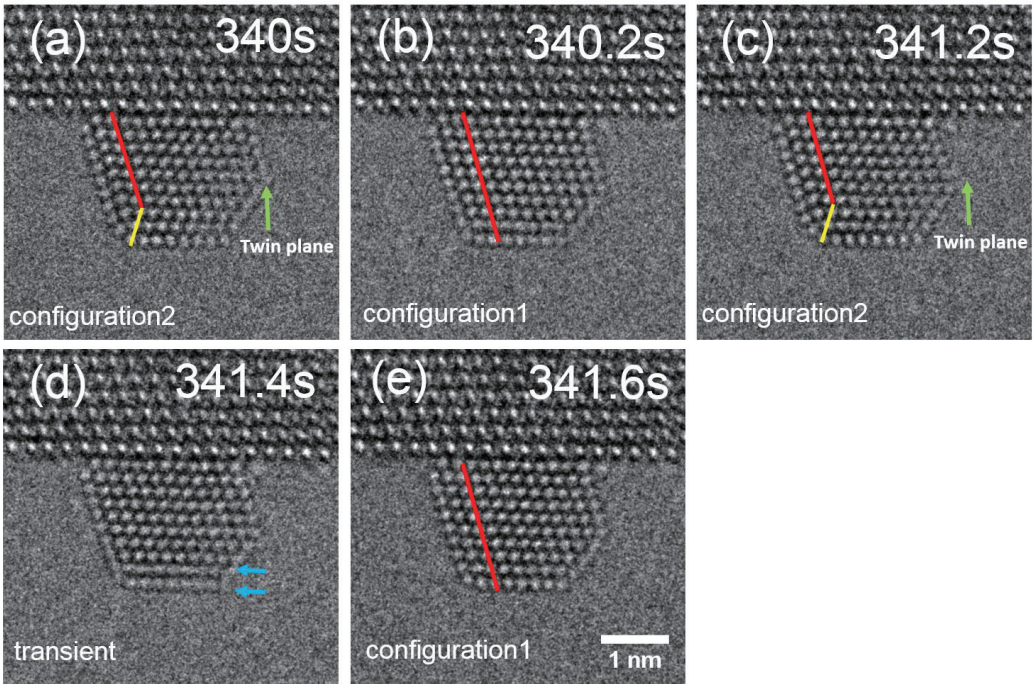

Figure 5.15 Surface atom diffusion induced surface twinning-detwinning. Red and yellow lines show the [111] directions of the atoms; green arrows indicate twin planes, and blue arrows indicate an intermediate state of atom diffusion. Exposure time is 0.2 s for each frame.

The detailed positions of the atoms in Figure. 5.15 (b) and 5.15 (c) of configuration 1 and configuration 2 have been sketched in Figure 5.16. For the analysis of the twinning nucleation and kinetics, these two atom schematics are overlapped to show the atomic position differences between the two configurations. The blue surface column atoms in configuration 1 diffuse in the anticlockwise direction to new positions as indicated by red atoms for configuration 2. The movement distance of each atom column, especially the top surface and subsurface columns, is different, as sketched, while the other atom columns stay at the same positions.

Strain mapping of configuration 1 and configuration 2 are shown in Figure 5.17. Configuration 1 has strong perpendicular expansion strain in the top 2 layers on the (111) facet B and (100) facet C. In the parallel direction, the left part of the nanoparticle shows expansion strain, and the right part shows compression strain.

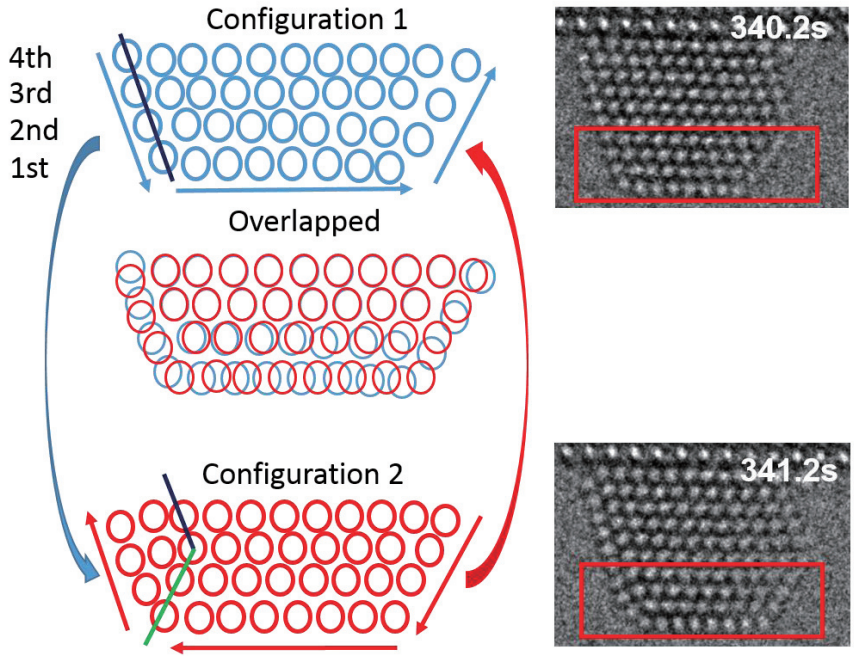

Figure 5.16 Surface twinning-detwinning via surface atom column concerted diffusion. The atom schematics are extracted from the red box areas showing the transition process between configuration 1 and configuration 2.

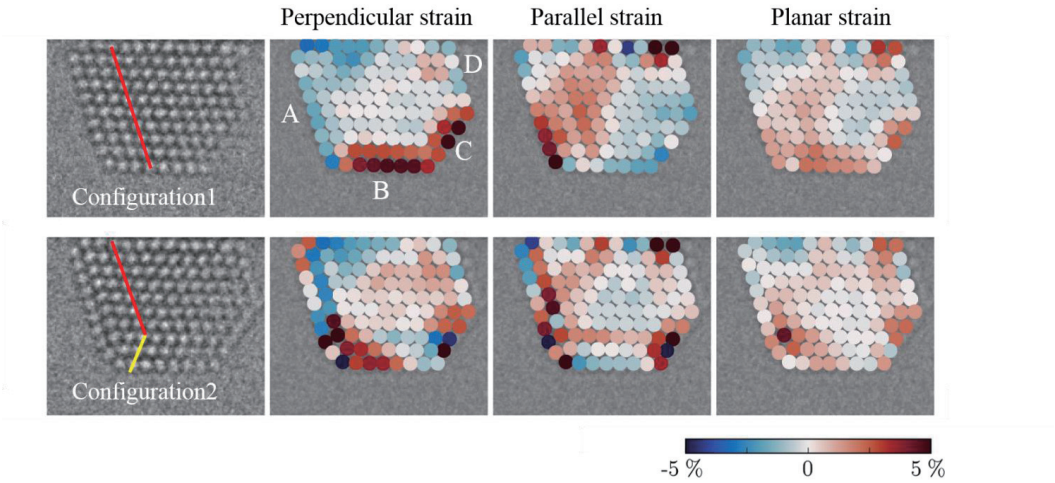

Figure 5.17 Strain mapping of configuration 1 and configuration 2. The nanoparticle-substrate interface is used as reference; the perpendicular strain means the strain perpendicular to the interface. The color scale bar from left to right is from compression strain to expansion strain. The strain mapping of configuration 2 is under the assumption that the third layer (from the surface) is a twin plane. A, B and D are {111} facets and C is (100) facet.

Configuration 2 has strong expansion strain at corner sites in both perpendicular and parallel directions. Here, the strain calculation only considers the six surrounding columns for a specific column without a periodic template, as shown in Chapter 2, which means twin boundary induced crystallographic distortion is not included in the strain map.

It can be speculated that the potential energies of these two configurations may be similar since configuration 1 has larger surface strains than configuration 2; while configuration 2 has a twin boundary inside which will give an additional contribution to the potential energy. In that case, atmosphere stimulation either in a thermally-driven way by temperature or in an adsorbate-driven way by gaseous surroundings can easily trigger the nanoparticle to overcome the energy barrier between these two configurations.

The other parallel twinning close to the interface (case B) is shown in Figure 5.18. It is a similar twinning process as for case A shown in Figure 5.14, but the layer shifting is due to nanoparticle motion induced inter-layer shifting. At 18.4 s, the red line indicates that part of the particle which shifts upward by 0.2 nm (one (111) lattice spacing) while the bottom three layers slide with a displacement of approximate 0.67 nm of each (third of the lattice spacing) layer by layer. As a result, a three-layer new twin forms beside the interface. The total time for the twinning formation process was ≤ 1.8 s, from 16.6 s to 18.4 s. However, the twin close to the interface was not stable. For example, at 20.2 s, as the top part of the particle rigidly slides back, one layer of the new twin shifts to the original lattice location and only two layers are left of this twin. As the process continues, the twin disappears at 21.4 s.

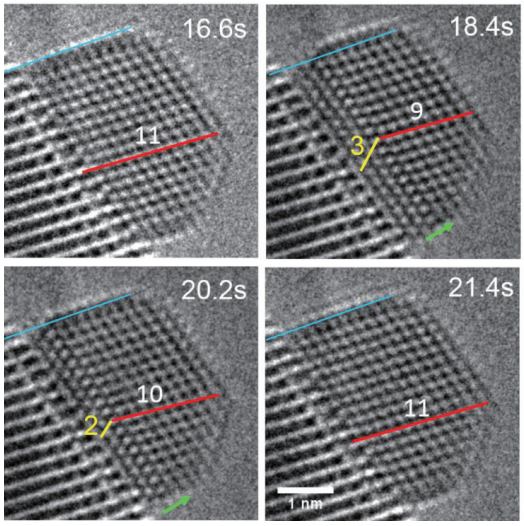

Figure 5.18 Twinning evolution of a supported Au nanoparticle where the twinning occurs at the interface between particle and substrate. The original crystalline structure is indicated by the red line and the new twins are indicated by the yellow line. The twinned layers are labeled respectively at the different time. Blue lines indicate the same position from a substrate reference location. Experimental conditions: 600°C 5.5 Pa O_2.

Figure 5.19 shows case C, an intersection twinning transformation where the twinning plane intersects the interface between the particle and substrate. Red lines indicate the original atom arrangement direction, while the yellow line indicates the atom arrangement direction in the new twin. In this case, the bottom part of the nanoparticle transforms to a different orientation at 113.4 s and changes back to the original orientation at 114.6 s.

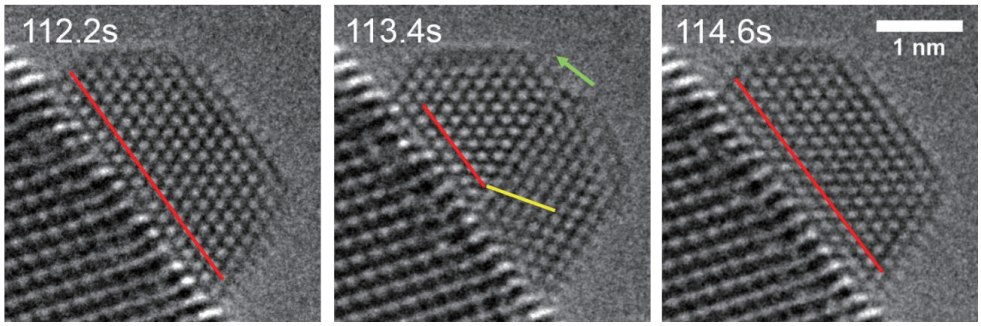

Figure 5.19 Intersection twinning evolution with the twinning plane intersecting the particle-substrate interface. Red lines indicate the original atom arrangement direction, and the yellow line indicates the atom arrangement in the new twin. The green arrow is normal to the twin plane. Experimental conditions: 600°C, 5.5 Pa O_2.

In the above cases, several unstable twinning structures have been observed, while in several other observations twins could be stable and survive harsh conditions, such as prolonged electron beam irradiation, exposure to different gases and temperature ramp up-down cycles. In the following section, the surface dynamics of a gold nanoparticle with two twins will be discussed.

Figure 5.20 shows, schematically, a nanoparticle consisting of two twins: top (black) 6 atomic layers and bottom (red) 3 layers, where the twin plane is marked by solid green circles. This nanoparticle transforms through surface atom diffusion rather than the twinning-detwinning process. The nanoparticle transforms between two atom arrangement configurations: in configuration 1 the nanoparticle is truncated by 5 surface facets labelled A, B, C, D, and E whilst in configuration 2 the nanoparticle is enclosed by 6 surface facets A, B, C, D, E, and F. It is interesting that such a transformation is associated with atom diffusion between two specific scenarios back and forth. During the configuration transformation, the twin boundary always remains in the same position with respect to the other part of the nanoparticle.

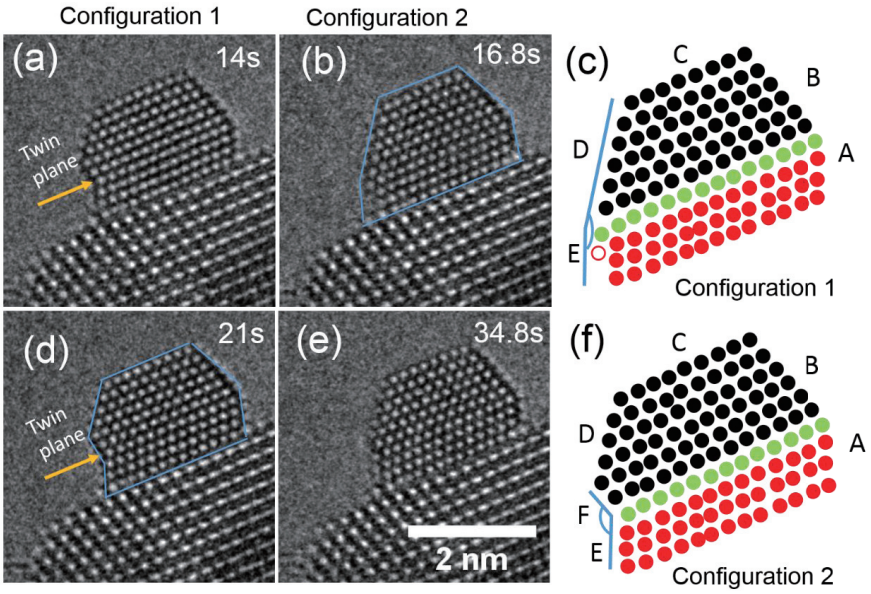

Figure 5.20 High resolution images recorded at different showing the atomic morphology of an Au nanoparticle with two twins. Adjacent are schematic representations of the area bounded by the blue box, where black circles represent atomic columns in the top twin and red circles represent atomic columns in the bottom twin. The green layer is the twin plane. Each surface facet is labeled by a letter. In configuration 1, the twin boundary associated angle between facet D and E is a convex configuration. In configuration 2, a new facet F is formed and the twin boundary associated corner angle between F and E is now in a concave configuration. Experimental conditions: 350°C, 5.5 Pa O_2.

In order to understand the atom arrangement difference between these two specific scenarios, the schematics are overlapped in Figure 5.21. Open circles represent columns that remain in the same locations. The solid circles are the differences between these two configurations: configuration 1 has five more columns indicated by filled orange circles on facet D; configuration 2 has two more blue filled columns on facet E. The dynamical transformation from configuration 1 to configuration 2 occurs by the disappearance of the five red columns and the appearance of two blue columns while the transformation from configuration 2 to configuration 1 is the reverse process. Such scenarios suggest that facet D and facet E are two sites to which diffusing adatoms prefer to attach. Atoms detached from either facet D or facet E have a possibility to fill facet E or facet D for short periods.

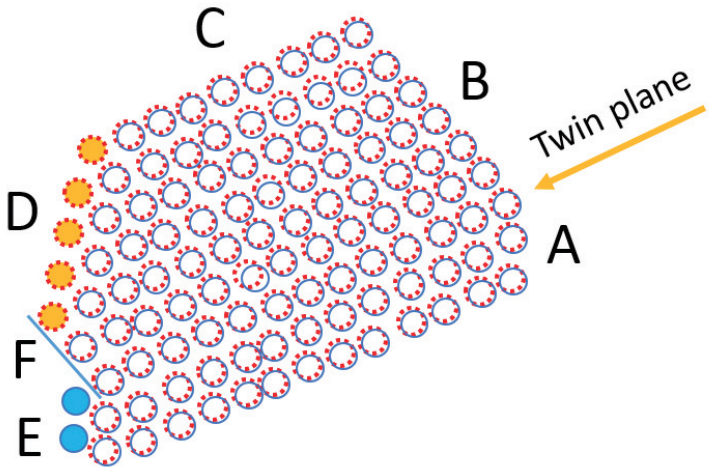

Figure 5.21 Overlapped schematic of the two configurations shown in Figure 5.20. Dashed red circles represent configuration 1, and the solid blue circle represents configuration 2. A comparison between these two configurations shows that configuration 1 has five more columns indicated by a filled red circle on facet D and configuration 2 has two more blue filled columns on facet E.

Chapter 6 Conclusions and Outlook

Conclusions

The surface dynamics of nanoparticles have been systematically investigated on the model systems Au/CeO_2 and Au/TiO_2 by means of *in situ* time-resolved high-resolution transmission electron microscopy. Responses of the materials have been tracked at the atomic level under different atmospheric conditions (various dose rates, various gases, and various temperatures).

Influences of the electron flux on the atom column diffusion have been evaluated before *in situ* experiments in the presence of various gases. Columns with higher binding energy start hopping under higher electron flux, indicating the positive correlation between the binding energy of Au nanoparticles and the electron flux. The internal energy mostly contributes to the kinetic energy of the diffusing atoms, increasing with electron flux and the total time of exposure. For a given electron flux, the hopping column number increases with the exposure time. For columns with a high coordination number, i.e., higher binding energy, hopping is only observed under high electron flux.

Diffusion of surface atoms exists under most conditions and is normally reversible. Several nanoparticles have been observed in different gases, and the time averaged morphology, column occupation percentage, diffusion events frequency and in time averaged strain have been analyzed. The interface energy between nanoparticles and the substrate is higher in O_2 (stronger bonding) than in H_2, while the surface showed more activity in O_2.

Under some conditions the diffusing atoms on the surface move in a concerted manner. Atoms in the same layer shift in the same direction at the same time or disappear-reappear at the same time. Such concerted and reversible behavior of a group of atoms suggests a variety of configurations which can be considered as local minima in potential energies in a configurational space.

Three types of nanoparticle motion on oxide substrates have been observed. These are categorized as particle rigid sliding, particle movements via mass transport, rigid rotation. Nanoparticle sintering is a particularly severe problem for catalysts where the nanoparticles tend to grow in size and lose total surface area by Ostwald ripening or particle migration and coalescence. Temperature and surrounding gases typically accelerate this process. The observation of nanoparticles motion at atomic level may enable a deeper understanding of the initial phase of sintering.

The Crystallographic relationship between nanoparticle and substrate has been examined quantitatively. Two distinct relationships have been observed. Type I (Au (11-1) [101]//CeO_2 (11-1) [101]) dominate over Type II (Au (11-1) [-10-1]//CeO_2 (11-1) [101]) on the annealed sample. Nanoparticles can transform reversibly between these two types in the presence of O_2 at elevated temperature.

In H_2 and CO, the (100) surface layer starts to fluctuate between appearance-disappearance in the temperature range from 523K to 623K. In O_2, fluctuations at the (111) surface layer were more frequent compared to the (100) layer at elevated temperature. The real-time variations of configurations at different temperatures in H_2 indicate that the potential energies of the configurations vary with temperature.

Twinning-detwinning processes have been investigated. The reversible changes of local strain field and coordination number accompanied by the twinning-detwinninng process indicates such processes may be important for oscillations of heterogeneously catalyzed reactions.

Outlook

There are several interesting topics for future research: 1) *in situ* observations should approach industrial conditions even more, particularly at higher pressures; 2) correlation between local morphology variations and macroscopic reaction oscillations; 3) *in situ* characterization of the 3D structures; 4) big data analysis techniques development to match the current and future data gathering ability; 5) development of physical models to help us understand surface dynamics.

The first task is definitely a continuation of the surface dynamics observation. The observations should be carried out with statistical significance in order to obtain rational conclusions and to elucidate the change of fine structures on the atomic scale under reactive conditions and highlight the diversity in structures. In the meantime, this could lead to correlations between local structure and surface dynamics on the one hand and catalytic properties under reaction conditions on the other. *In situ* experiments should also be carried out under high-pressure conditions to bridge the pressure gap between ETEM pressure ranges to ambient pressure. Closed cell holders show promising results in order to obtain this.

In the present work, various surface diffusion and fluctuation processes have been explored. Naturally, the next step is to correlate such surface dynamics to reaction oscillations. Due to the low sensitivity of mass spectrometry detection ability by ETEM, it is challenging to obtain quantitative reaction rates and turn over frequencies during *in situ* TEM observations Again, a closed cell holder could be an approach to obtain correlations between nanostructural repsonses of the catalyst and reaction parameters.

Due to the nature of HRTEM, it is challenging to obtain three-dimensional information of the nanoparticles during in situ experimentation. Significant progress has been achieved to characterize the 3D structure nanometer nanoparticles with atomic resolution using tomography. Such information is lacking in the present observation which hinders an in depth understanding of these reversible dynamics. Electron tomography would be a good technique to achieve atomic three-dimensional characterization in real time. With the combination of discrete tomography and the recently developed statistical parameter estimation theory, a three-dimensional structure can be reconstructed by only two images with atomic resolution[142]. However, two main limitations should be taken into account prior to electron tomography, namely geometric and time. It still a fascinating and promising direction.

One of the most significant developments in the project has been use of machine learning to analyze HRTEM images, due to the excellent performance of convolutional neural networks (CNNs) in visual recognition tasks. The application of CNNs covers image classification, object detection, pixel level segmentation and more. In this project, a method using a CNN to detect the local structure in HRTEM images is proposed as shown in Chapter 5.

No convincing physical explanation of the observed behavior of the nanoparticles has been proposed until now. Results from other surface investigation techniques should also be combined to reach a comprehensive understanding of the various phenomena at work. It is an interdisciplinary task covering surface chemistry, thermal dynamics, and physics. Physical models should be developed in the future to help fully understand the fundamental properties of supported metal nanoparticle systems.

Bibliography

1. Haruta, M., Kobayashi, T., Sano, H. & Yamada, N. Novel gold catalysts for the oxidation of carbon monoxide at a temperature far below 0 °C. *Chem. Lett.* **16,** 405–408 (1987).

2. Knell, A., Barnickel, P., Baiker, A. & Wokaun, A. CO oxidation over Au/ZrO2 catalysts: Activity, deactivation behavior, and reaction mechanism. *J. Catal.* **137,** 306–321 (1992).

3. Lin, S. D., Bollinger, M. & Vannice, M. A. Low temperature CO oxidation over Au/TiO2 and Au/SiO2 catalysts. *Catal. Letters* **17,** 245–262 (1993).

4. Hammer, B. & Norskov, J. K. Theoretical surface science and catalysis - calculations and concepts. *Adv. Catal.* **45,** 71–129 (2000).

5. Nørskov, J. K., Abild-Pedersen, F., Studt, F. & Bligaard, T. Density functional theory in surface chemistry and catalysis. *Proc. Natl. Acad. Sci.* **108,** 937–943 (2011).

6. Nørskov, J. K. *et al.* The nature of the active site in heterogeneous metal catalysis. *Chem. Soc. Rev.* **37,** 2163–2171 (2008).

7. Jiang, T. *et al.* Trends in CO oxidation rates for metal nanoparticles and close-packed, stepped, and kinked surfaces. *J. Phys. Chem. C* **113,** 10548–10553 (2009).

8. Abild-Pedersen, F. *et al.* Scaling properties of adsorption energies for hydrogen-containing molecules on transition-metal surfaces. *Phys. Rev. Lett.* **99,** 4–7 (2007).

9. Imbihl, R. & Ertl, G. Oscillatory kinetics in heterogeneous catalysis. *Chem. Rev.* **95,** 697–733 (1995).

10. Imbihl, R. & Ertl, G. Oscillatory kinetics in a heterogeneous chemical reaction. *Chem. Rev.* **95,** 697–733 (1995).

11. Chávez, F., Vicente, L. & Perera, A. Kinetic oscillations in the catalytic CO oxidation on Pt(100) with adsorbed impurities. *J. Chem. Phys.* **113,** 10353–10360 (2000).

12. Vendelbo, S. B. *et al.* Visualization of oscillatory behaviour of Pt nanoparticles catalysing CO oxidation. *Nat. Mater.* **13,** 884–890 (2014).

13. Needs, R. J., Godfrey, M. J. & Mansfield, M. Theory of surface stress and surface reconstruction. *Surf. Sci.* **242,** 215–221 (1991).

14. Cammarata, R. C. Surface and interface stress effects in thin films. *Prog. Surf. Sci.* **46,** 1–38 (1994).

15. Cammarata, R. C. Continuum model for surface reconstructions in (111) and (100) oriented surfaces of fcc metals. *Surf. Sci.* **279,** 341–348 (1992).

16. Takeuchi, N., Chan, C. T. & Ho, K. M. Au(111): A theoretical study of the surface reconstruction and the surface electronic structure. *Phys. Rev. B* **43,** 13899–13906 (1991).

17. Lozovoi, A. Y. & Alavi, A. Reconstruction of charged surfaces: General trends and a case study of Pt(110) and Au(110). *Phys. Rev. B* **68,** 245416 (2003).

18. Crljen, Z., Lazic, P., Sokcevic, D. & Brako, R. Relaxation and reconstruction on (111) surfaces of Au, Pt, and Cu. *Phys. Rev. B* **68,** 1–8 (2003).

19. Martini, K. M. Double Sine Gordon Solitons: A Model for Misfit Dislocations on the Au (111) reconstructed surface. *Phys. Rev. Lett.* **58,** 2762–2765 (1987).

20. Hasegawa, Y. & Avouris, P. Manipulation of the Reconstruction of the Au (111) Surface with the STM. *Science (80-.).* **258,** 1763–1765 (2017).

21. Hiebel, F. *et al.* Self-assembly of acetate adsorbates drives atomic rearrangement on the Au(110) surface. *Nat. Commun.* **7,** 13139 (2016).

22. Sault, A. G., Madix, R. J. & Campbell, C. T. Adsorption of oxygen and hydrogen on Au(110)-(1x2). *Surf. Sci.* **169,** 347–356 (1986).

23. Meyer, R., Lemire, C., Shaikhutdinov, S. K. & Freund, H.-J. Surface chemistry of catalysis by gold. *Gold Bull.* **37,** 72–124 (2004).

24. Gottfried, J. M., Schmidt, K. J., Schroeder, S. L. M. & Christmann, K. Oxygen chemisorption on Au(110)-(1 x 2) II. Spectroscopic and reactive thermal desorption measurements. *Surf. Sci.* **525,** 197–206 (2003).

25. Piccolo, L. *et al.* The adsorption of CO on Au(1 1 1) at elevated pressures studied by STM, RAIRS and DFT calculations. *Surf. Sci.* **566–568,** 995–1000 (2004).

26. Baker, T. a., Friend, C. M. & Kaxiras, E. Atomic Oxygen Adsorption on Au(111) Surfaces with Defects. *J. Phys. Chem. C* **113,** 3232–3238 (2009).

27. Dumas, P., Tobin, R. G. & Richards, P. L. Study of adsorption states and interactions of CO on evaporated noble metal surfaces by infrared absorption spectroscopy. II. Gold and copper. *Surf. Sci.* **171,** 579–599 (1986).

28. Ruggiero, C. & Hollins, P. Adsorption of carbon monoxide on the gold (332) surface. *J. Chem. Soc. Faraday Trans.* **92,** 4829–4834 (1996).

29. Gottfried, J. M., Schmidt, K. J., Schroeder, S. L. M. & Christmann, K. Adsorption of carbon monoxide on Au(1 1 0)-(1×2). *Surf. Sci.* **536,** 206–224 (2003).

30. Canning, N. D. S., Outka, D. & Madix, R. J. The adsorption of oxygen on gold. *Surf. Sci.* **141,** 240–254 (1984).

31. Outka, D. A. & Madix, R. J. Acid-base and nucleophilic chemistry of atomic oxygen on the Au(110) surface: Reactions with formic acid and formaldehyde. *Surf. Sci.* **179,**

361–376 (1987).

32. Gottfried, J. ., Schmidt, K. ., Schroeder, S. L. . & Christmann, K. Oxygen chemisorption on Au(110)-(1×2) I. Thermal desorption measurements. *Surf. Sci.* **525,** 184–196 (2003).

33. Gottfried, J. M., Elghobashi, N., Schroeder, S. L. M. & Christmann, K. Oxidation of gold by oxygen-ion sputtering. *Surf. Sci.* **523,** 89–102 (2003).

34. Gottfried, J. ., Schmidt, K. ., Schroeder, S. L. . & Christmann, K. Spontaneous and electron-induced adsorption of oxygen on Au(110)-(1×2). *Surf. Sci.* **511,** 65–82 (2002).

35. Saliba, N., Parker, D. . & Koel, B. . Adsorption of oxygen on Au(111) by exposure to ozone. *Surf. Sci.* **410,** 270–282 (1998).

36. Davis, K. A. & Goodman, D. W. Propene Adsorption on Clean and Oxygen-Covered Au(111) and Au(100) Surfaces. *J. Phys. Chem. B* **104,** 8557–8562 (2000).

37. Stobiński, L. Molecular and atomic deuterium chemisorption on thin gold films at 78K an isotope effect. *Appl. Phys. Lett.* **103,** 503–508 (1996).

38. Stobiński, L., Zommer, L. & Duś, R. Molecular hydrogen interactions with discontinuous and continuous thin gold films. *Appl. Surf. Sci.* **141,** 319–325 (1999).

39. Barnard, A. S., Young, N. P., Kirkland, A. I., Van Huis, M. A. & Xu, H. Nanogold: A quantitative phase map. *ACS Nano* **3,** 1431–1436 (2009).

40. Wang, Z. W. & Palmer, R. E. Determination of the ground-state atomic structures of size-selected Au nanoclusters by electron-beam-induced transformation. *Phys. Rev. Lett.* **108,** 1–5 (2012).

41. Akita, T., Okumura, M., Tanaka, K. & Haruta, M. SEM and RHEED-REM study of Au particles deposited on rutile TiO2 (110) by deposition precipitation and gas-phase grafting methods. *J. Catal.* **212,** 119–123 (2002).

42. Akita, T., Tanaka, K., Tsubota, S. & Haruta, M. Analytical high–resolution TEM study of supported gold catalysts: orientation relationship between Au particles and Ti02 supports. *J. Electron Microsc. (Tokyo).* **49,** 657–662 (2000).

43. Akita, T., M., O., K., T., M., K. & M., H. TEM observation of gold nanoparticles deposited on cerium oxide. *J. Mater. Sci.* **40,** 3101–3106 (2005).

44. Majimel, J., Lamirand-Majimel, M., Moog, I., Feral-Martin, C. & Tréguer-Delapierre, M. Size-dependent stability of supported gold nanostructures onto ceria: An HRTEM study. *J. Phys. Chem. C* **113,** 9275–9283 (2009).

45. Lofton, C. & Sigmund, W. Mechanisms controlling crystal habits of gold and silver colloids. *Adv. Funct. Mater.* **15,** 1197–1208 (2005).

46. Elechiguerra, J. L., Reyes-Gasga, J. & Yacaman, M. J. The role of twinning in shape

evolution of anisotropic noble metal nanostructures. *J. Mater. Chem.* **16,** 3906 (2006).

47. Meyer, J. C., Girit, C. O., Crommie, M. F. & Zettl, A. Imaging and dynamics of light atoms and molecules on graphene. *Nature* **454,** 319–322 (2008).

48. Tan, Y. W. *et al.* Graphene at the edge: stability and dynamics. *Science (80-.).* **666,** 1705–1708 (2009).

49. Toney, M. F., Wang, L., Kisielowski, C. & Alivisatos, a P. Observation of transient structural-transformation dynamics in a Cu2S nanorod. *Science (80-.).* **1,** 206–209 (2011).

50. Surrey, A., Pohl, D., Schultz, L. & Rellinghaus, B. Quantitative measurement of the surface self-diffusion on Au nanoparticles by aberration-corrected transmission electron microscopy. *Nano Lett.* **12,** 6071–6077 (2012).

51. Schneider, S., Surrey, A., Pohl, D., Schultz, L. & Rellinghaus, B. Atomic surface diffusion on Pt nanoparticles quantified by high-resolution transmission electron microscopy. *Micron* **63,** 52–56 (2014).

52. Pennycook, T. J. *et al.* Atomic scale dynamics of a solid state chemical reaction directly determined by annular dark-field electron microscopy. *Sci. Rep.* **4,** 7555 (2014).

53. Bhatta, U. M. *et al.* Cationic surface reconstructions on cerium oxide nanocrystals: An aberration-corrected HRTEM study. *ACS Nano* **6,** 421–430 (2012).

54. Meyer, J. C., Kisielowski, C., Erin, R., Rossell, M. D. & Crommie, M. F. Direct imaging of lattice atoms and topological defects in graphene membranes. *Nano Lett.* **8,** 3582–3586 (2008).

55. Kotakoski, J. *et al.* Stone-Wales-type transformations in carbon nanostructures driven by electron irradiation. *Phys. Rev. B - Condens. Matter Mater. Phys.* **83,** 1–6 (2011).

56. Kisielowski, C. Observing atoms at work by controlling beam-aample interactions. *Adv. Mater.* **27,** 5838–5844 (2015).

57. Hosseinizadeh, A. *et al.* High-resolution structure of viruses from random diffraction snapshots. *Philos. Trans. R. Soc. B Biol. Sci.* **369,** 20130326–20130326 (2014).

58. Kisielowski, C. Observing Atoms at Work by Controlling Beam-Sample Interactions. *Adv. Mater.* **27,** 5838–5844 (2015).

59. Egerton, R. F., Li, P. & Malac, M. Radiation damage in the TEM and SEM. *Micron* **35,** 399–409 (2004).

60. Kisielowski, C. *et al.* Real-time sub-Ångstrom imaging of reversible and irreversible conformations in rhodium catalysts and graphene. *Phys. Rev. B - Condens. Matter Mater. Phys.* **88,** 1–12 (2013).

61. Takeda, S., Kuwauchi, Y. & Yoshida, H. Environmental transmission electron microscopy for catalyst materials using a spherical aberration corrector. *Ultramicroscopy* **151,** 178–190 (2015).

62. Uchiyama, T. *et al.* Systematic morphology changes of gold nanoparticles supported on CeO2 during CO oxidation. *Angew. Chemie* 10339–10342 (2011). doi:10.1002/ange.201102487

63. Yoshida, H. *et al.* Visualizing gas molecules interacting with supported nanoparticulate catalysts at reaction conditions. *Science (80-.).* **628,** (2011).

64. Uchiyama, T., Yoshida, H., Kamiuchi, N., Kohno, H. & Takeda, S. Revealing the heterogeneous contamination process in metal nanoparticulate catalysts in CO gas without purification by in situ environmental transmission electron microscopy. *Microscopy* **65,** 522–526 (2016).

65. Zhang, S. *et al.* Dynamic structural evolution of supported palladium–ceria core–shell catalysts revealed by in situ electron microscopy. *Nat. Commun.* **6,** 7778 (2015).

66. Dai, S. *et al.* Revealing surface elemental composition and dynamic processes involved in facet-dependent oxidation of Pt3Co nanoparticles via in situ transmission electron microscopy. *Nano Lett.* **17,** 4683–4688 (2017).

67. Zhang, S. *et al.* Dynamical observation and detailed description of catalysts under strong metal-support interaction. *Nano Lett.* acs.nanolett.6b01769 (2016). doi:10.1021/acs.nanolett.6b01769

68. Williams, D. B. & Carter, C. B. *Transmission Electron Microscopy*. *Transmission Electron Microscopy* (2009). doi:10.1007/978-0-387-76501-3_1

69. F.Krumeich. Mass-thickness and Bragg Contrast. (2015). at <http://www.microscopy.ethz.ch/mtc.htm>

70. Kirkland, J. E. *Advanced Computing in Electron Microscopy*. (1998).

71. Pierre Stadelmann. JEMS-SAAS. at <http://www.jems-saas.ch/>

72. Koch, C. QSTEM: Quantitative TEM/STEM Simulations. at <https://www.physics.hu-berlin.de/en/sem/software/software_qstem?page_id=28>

73. Jian-Min Zuo. EMAPS electron microscopy APplication. at <http://cbed.matse.illinois.edu/software_emaps.html>

74. Dr. Probe - High-resolution (S)TEM image simulation software. at <http://www.er-c.org/barthel/drprobe/>

75. Google's Python Class | Python Education | Google Developers. at <https://developers.google.com/edu/python/introduction>

76. Shein, E. Python for beginners. *Commun. ACM* **58,** 19–21 (2015).

77. Al, L. et. The Atomic Simulation Environment — A Python library for working with atoms. *J. Phys. Condens. Matter* (2017). doi:10.1088/1361-648X/aa680e

78. Creemer, J. F. *et al.* Atomic-scale electron microscopy at ambient pressure. *Ultramicroscopy* **108,** 993–998 (2008).

79. DENSsolution. DENSsolution wirdfire. at <httpwww.denssolutions.comproductsclimate>

80. DENSsolution Climate. Wildfire. *Wildfire in situ TEM heating* at <http://denssolutions.com/products/wildfire/>

81. Hansen, T. W. & Wagner, J. B. *Controlled Atmosphere Transmission Electron Microscopy*. (Springer International Publishing, 2016). doi:10.1007/978-3-319-22988-1

82. Bierwolf, R. *et al.* Direct measurement of local lattice distortions in strained layer structures by HREM. *Ultramicroscopy* **49,** 273–285 (1993).

83. Galindo, P. L. *et al.* The Peak Pairs algorithm for strain mapping from HRTEM images. *Ultramicroscopy* **107,** 1186–1193 (2007).

84. Zuo, J.-M. *et al.* Lattice and strain analysis of atomic resolution Z-contrast images based on template matching. *Ultramicroscopy* **136,** 50–60 (2014).

85. Hÿtch, M. J., Snoeck, E. & Kilaas, R. Quantitative measurement of displacement and strain fields from HREM micrographs. *Ultramicroscopy* **74,** 131–146 (1998).

86. Madsen, J., Liu, P., Wagner, J. B., Hansen, T. W. & Schiøz, J. Accuracy of surface strain measurements from transmission electron microscopy images of nanoparticles. *Adv. Struct. Chem. Imaging* **3,** 14 (2017).

87. Q150T Turbo-Pumped Sputter Coater/Carbon Coater | Quorum Technologies. at <https://www.quorumtech.com/quorum-product/q150t-turbo-pumped-sputter-coatercarbon-coater>

88. Miller, B. K. & Crozier, P. A. Analysis of catalytic gas products using electron energy-loss spectroscopy and residual gas analysis for operando transmission electron microscopy. *Microsc. Microanal.* **20,** 815–824 (2014).

89. Lee, Z., Rose, H., Lehtinen, O., Biskupek, J. & Kaiser, U. Electron dose dependence of signal-to-noise ratio , atom contrast and resolution in transmission electron microscope images. *Ultramicroscopy* **145,** 3–12 (2014).

90. Kim, K. *et al.* Atomically perfect torn graphene edges and their reversible reconstruction. *Nat. Commun.* **4,** 2723 (2013).

91. Van Dorp, W. F. *et al.* Molecule-by-molecule writing using a focused electron beam. *ACS Nano* **6,** 10076–10081 (2012).

92. Rose, A. & Biberman, L. *Vision: Human and Electronic*. *Phys. Today* **28,** 49–50 (1975).

93. Natusch, M. K. H., Humphreys, C. J., Menon, N. & Krivanek, O. L. Experimental and theoretical study of the detection limits in electron energy-loss spectroscopy. *Mater. Sci.* **30,** 173–183 (1999).

94. Jia, C. L. *et al.* Determination of the 3D shape of a nanoscale crystal with atomic resolution from a single image. *Nat. Mater.* **13,** 1044–9 (2014).

95. Wang, Z. W. & Palmer, R. E. Mass spectrometry and dynamics of gold adatoms observed on the surface of size-selected au nanoclusters. *Nano Lett.* **12,** 91–95 (2012).

96. Jones, L., Macarthur, K. E., Fauske, V. T., Helvoort, A. T. J. Van & Nellist, P. D. Rapid estimation of catalyst nanoparticle morphology and atomic- coordination by high-resolution Z‑contrast electron microscopy. *Nano Lett.* **14,** 6336–6341 (2014).

97. Pötting, K., Schmickler, W. & Jacob, T. Self-diffusion on Au(100): A density functional theory study. *ChemPhysChem* **11,** 1395–1404 (2010).

98. Ferrando, R. & Tréglia, G. Anisotropy of diffusion along steps on the (111) faces of gold and silver. *Phys. Rev. B* **50,** 12104–12117 (1994).

99. Liu, C. L., Cohen, J. M., Adams, J. B. & Voter, A. F. EAM study of surface self-diffusion of single adatoms of fcc metals Ni, Cu, Al, Ag, Au, Pd, and Pt. *Surf. Sci.* **253,** 334–344 (1991).

100. Zhu, B., Meng, J. & Gao, Y. Equilibrium shape of metal nanoparticles under reactive gas conditions. *J. Phys. Chem. C* 5629–5634 (2017). doi:10.1021/acs.jpcc.6b13021

101. Hugo, P. Stabilität und Zeitverhalten von Durchfluß-Kreislauf-Reaktoren. *Berichte der Bunsengesellschaft für Phys. Chemie* **74,** 121–127 (1970).

102. Imbihl, R., Cox, M. P. & Ertl, G. Kinetic oscillations in the catalytic CO oxidation on Pt (100): Experiments Kinetic osciUations in the catalytic CO oxidation on Pt (100): Experiments. *J. Chem. Phys.* **84,** 3519 (1986).

103. Nettesheim, S. *et al.* Reaction diffusion patterns in the catalytic CO-oxidation on Pt (110): Front propagation and spiral waves Reaction diffusion patterns in the catalytic CO-oxidation on Pt (110): Front propagation and spiral waves. **9977,** (2008).

104. Martin, D. *et al.* Reversible restructuring of supported Au nanoparticles during butadiene hydrogenation revealed by operando GISAXS/GIWAXS. *Chem. Commun.* **53,** 5159–5162 (2017).

105. Kuwauchi, Y. *et al.* Stepwise displacement of catalytically active gold nanoparticles on cerium oxide. *Nano Lett.* **13,** 3073–3077 (2013).

106. Tao, F. *et al.* Restructuring of hex-Pt(100) under CO gas environments: Formation of 2-D nanoclusters. *Nano Lett.* **9,** 2167–2171 (2009).

107. Thostrup, P. *et al.* Adsorption-induced step formation. *Phys. Rev. Lett.* **87,** 126102 (2001).

108. Bhatta, U. M. *et al.* Electron beam induced surface morphology changes of Ce02 nanocrystals : an in-situ aberration corrected TEM study. **3,** 0–3 (2012).

109. Lin, Y. *et al.* Adhesion and Atomic Structures of Gold on Ceria Nanostructures: The Role of Surface Structure and Oxidation State of Ceria Supports. *Nano Lett.* **15,** 5375–5381 (2015).

110. Kawasaki, T., Takai, Y. & Shimizu, R. Distorted surface and interface structures of catalytic gold nanoparticles observed by spherical aberration-free phase electron microscopy. *Appl. Phys. Lett.* **79,** 3509–3511 (2001).

111. Akita, T., Kohyama, M. & Haruta, M. Electron microscopy study of gold nanoparticles deposited on transition metal oxides. *Acc. Chem. Res.* **46,** 1773–1782 (2013).

112. Simonsen, S. B. *et al.* Direct observations of oxygen-induced platinum nanoparticle ripening studied by in situ TEM. *J. Am. Chem. Soc.* **132,** 7968–75 (2010).

113. Hansen, T. W., Delariva, A. T., Challa, S. R. & Datye, A. K. Sintering of catalytic nanoparticles: particle migration or ostwald ripening? *Acc. Chem. Res.* **46,** 1720–1730 (2013).

114. Goniakowski, J., Mottet, C. & Noguera, C. Non-reactive metal/oxide interfaces: From model calculations towards realistic simulations. *Phys. Status Solidi Basic Res.* **243,** 2516–2532 (2006).

115. Van Huis, M. A. *et al.* Atomic maging of phase transitions and morphology transformations in nanocrystals. *Adv. Mater.* **21,** 4992–4995 (2009).

116. Li, X. *et al.* Direct observation of the layer-by-layer growth of ZnO nanopillar by in situ high resolution transmission electron microscopy. *Sci. Rep.* **7,** 40911 (2017).

117. Zhang, Z. *et al.* Atomic-scale observation of vapor-solid nanowire growth via oscillatory mass transport. *ACS Nano* **10,** 763–769 (2016).

118. Ta, N. *et al.* Stabilized gold nanoparticles on ceria nanorods by strong interfacial anchoring. *J. Am. Chem. Soc.* **134,** 20585–20588 (2012).

119. Baron, M., Bondarchuk, O., Stacchiola, D., Shaikhutdinov, S. & Freund, H. Interaction of gold with cerium oxide supports : CeO 2 (111) thin films vs CeOx nanoparticles. **2,** 6042–6049 (2009).

120. Delgado, J. J. *et al.* Environment Dependent Structure of Catalyst Nanoparticles. *Chem. Lett.* **40,** 1–13 (2011).

121. Chen, M. S. & Goodman, D. W. The Structure of Catalytically Active Gold on Titania. *Science (80-.).* **306,** 252 LP-255 (2004).

122. Haruta, M. Size- and Support-Dependency in The Catalysis of Gold. *Catal. Today* **36,** 153–166 (1997).

123. Gao, W., Sivaramakrishnan, S., Wen, J. & Zuo, J.-M. Direct Observation of Interfacial Au Atoms on TiO2 in Three Dimensions. *Nano Lett.* 150317103032003 (2015). doi:10.1021/acs.nanolett.5b00682

124. Daniel, M. C. M. & Astruc, D. Gold Nanoparticles: Assembly, Supramolecular Chemistry, Quantum-Size Related Properties and Applications toward Biology, Catalysis and Nanotechnology. *Chem. Rev.* **104,** 293–346 (2004).

125. Marks, L. D. Experimental studies of small particle structures. *Reports Prog. Phys.* **57,** 603–649 (1999).

126. Young, N. P., van Huis, M. A., Zandbergen, H. W., Xu, H. & Kirkland, A. I. Transformations of gold nanoparticles investigated using variable temperature high-resolution transmission electron microscopy. *Ultramicroscopy* **110,** 506–516 (2010).

127. Doraiswamy, N. & Marks, L. D. Preferred structures in small particles. *Philos. Mag. B-Physics Condens. Matter Stat. Mech. Electron. Opt. Magn. Prop.* **71,** 291–310 (1995).

128. Gilles, B., Marty, A. & Eymery, J. Molecular beam epitaxial growth of Au(110) layers on MgO(110) substrates. *Appl. Surf. Sci.* **68,** 203–207 (1993).

129. Wallenberg, L. R., Smith, D. J., Petford-Long, A. K., Wallenberg, L. R. & Bovin, J. O. Dynamic atomic-level rearrangements in small gold particles. *Science (80-.).* **233,** 872–5 (1986).

130. Behrens, M. *et al.* The active site of methanol synthesis over Cu/ZnO/Al2O3 industrial catalysts. *Science (80-.).* **759,** 893–898 (2012).

131. Camellone, M. F. *et al.* Reaction mechanisms for the CO oxidation on Au/CeO_2 catalysts: Activity of substitutional Au^{3+}/Au^{+} cations and deactivation of supported Au^{+} adatoms. *J. Am. Chem. Soc.* **131,** 10473–10483 (2009).

132. Wardenga, H. F. & Klein, A. Surface potentials of (111), (110) and (100) oriented CeO2-x thin films. *Appl. Surf. Sci.* **377,** 1–8 (2016).

133. Hernández, N. C., Grau-Crespo, R., de Leeuw, N. H. & Sanz, J. F. Electronic charge transfer between ceria surfaces and gold adatoms: a GGA+U investigation. *Phys. Chem. Chem. Phys.* **11,** 5246–5252 (2009).

134. Buffat, P. & Borel, J. P. Size effect on the melting temperature of gold particles. *Phys. Rev. A* **13,** 2287–2298 (1976).

135. Lee, J., Tanaka, T., Lee, J. & Mori, H. Effect of substrates on the melting temperature of gold nanoparticles. *Calphad Comput. Coupling Phase Diagrams Thermochem.* **31,** 105–111 (2007).

136. Vesborg, P. C. K. *et al.* Transient behavior of Cu/ZnO-based methanol synthesis

catalysts. *J. Catal.* **262,** 65–72 (2009).

137. Le, P. H. & Luo, C. W. in *Applications of Laser Ablation - Thin Film Deposition, Nanomaterial Synthesis and Surface Modification* (2016). doi:10.5772/65898

138. Ringe, E., Van Duyne, R. P. & Marks, L. D. Wulff construction for alloy nanoparticles. *Nano Lett.* **11,** 3399–3403 (2011).

139. Winterbottom, W. . Equilibrium shape of a small particle in contact with a foreign substrate. *Acta Metall.* **15,** 303–310 (1967).

140. Kuwauchi, Y., Yoshida, H., Akita, T., Haruta, M. & Takeda, S. Intrinsic catalytic structure of gold nanoparticles supported on TiO 2. *Angew. Chemie - Int. Ed.* **51,** 7729–7733 (2012).

141. Yoshida, H., Omote, H. & Takeda, S. Oxidation and reduction processes of platinum nanoparticles observed at the atomic scale by environmental transmission electron microscopy. *Nanoscale* 13113–13118 (2014). doi:10.1039/c4nr04352a

142. Van Aert, S., Batenburg, K. J., Rossell, M. D., Erni, R. & Van Tendeloo, G. Three-dimensional atomic imaging of crystalline nanoparticles. *Nature* **470,** 374–377 (2011).

Appendix A- HRTEM image simulation

Appendix A demonstrate an example of image simulation procedure on Jupyter Notebook dependency. The simulation is use PyQSTEM benchmark, it is open source and can be found on github: https://github.com/jacobjma/PyQSTEM. The image simulation procedure is follow the steps described in Chapter 2.

1 Import python packages

```
In [1]: %matplotlib inline
        import numpy as np
        import matplotlib.pyplot as plt
        from matplotlib import gridspec
        from ase.cluster.wulff import wulff_construction
        from qstem import Multislice, CTF
        from qstem.util import atoms_plot
```

2 set up a model of a gold nanoparticles with a Wulff shape and rotate it into [110] zone axis Output results and images display below the script area

```
In [2]: N = 500# Target number of atoms
        surfaces = [(1, 0, 0), (1, 1, 0), (1, 1, 1)] # Surface directions
        esurf = [1198, 1278, 979]
        #Corresponding surface energies mJ/m^2 (DFT values using the PBEsol functional)
        atoms = wulff_construction('Au', surfaces, esurf, N, 'fcc', rounding='closest', latticeconstant=4.078)
        atoms.rotate('y',a=np.pi/4.)
        atoms.rotate('z',a=np.arctan(np.sqrt(2.)))
        atoms.center(vacuum=5)
        pos=atoms.get_positions()
        x=pos[:,0]
        y=pos[:,1]
        atoms_plot(atoms,direction=2)

        print('Actual number of atoms:',len(atoms))

        Actual number of atoms: 459
```

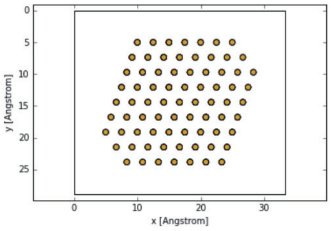

3 set up microscope and simulation parameters

```
In [3]: energy=300 # Beam energy keV
        sampling=0.1 # Angstrom/pixel
        slice_thickness=1 # Angstrom
        wave=Multislice(atoms,energy=energy,sampling=sampling,slice_thickness=slice_thickness).run()
```

4 display the ‘real’ part of the exit wave function

```
In [4]: wave.view(method='real')
```

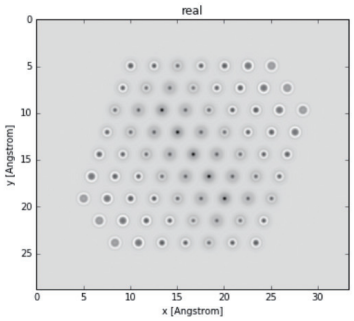

5 set up the contrast transfer function

The wavefunction is propagated to the imageplane using the contrast transfer function (CTF). In this example we simulate an aberration corrected microscope with a spherical aberration (Cs) of 5 microns. Partial spatial and temporal coherence is included by applying an envelope to the wavefunction (quasi-coherent approximation). The envelope is controlled by the focal spread and convergence angle.

```
In [5]: ctf=CTF(defocus=50,Cs=5*10**4,focal_spread=30)
        img_wave=wave.apply_ctf(ctf) # returns a new wave object
```

6 display the contrast transfer function

```
In [6]: ctf.radial_plot()
```

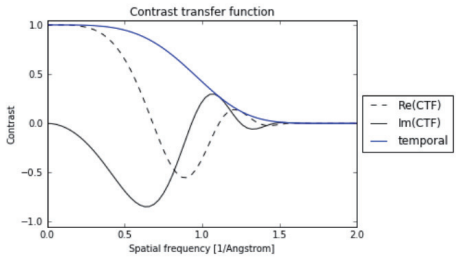

7 display the magnitude of the new wave function

```
In [7]: img_wave.view(method='amplitude')
```

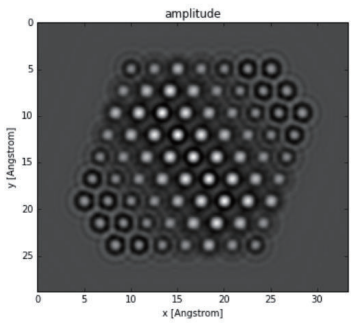

8 set up the detector information. The detected image is simply the absolute square of the wavefunction at the image plane. Detector resolutions are typically worse than what is required by the multislice algorithm, hence the image needs to be downsampled to the correct resolution.

```
In [8]: resample=.18 # Angstrom/pixel
        dose=5*10**6 #electrons/Angstrom squared
        img=img_wave.detect(dose=10**3,resample=resample) # returns a numpy array
```

Optionally, shot noise can be is simulated by specifying a finite electron dose. The mean of the Poisson distribution is given by

$$N^{-} = D\delta 2\, I$$

where D is the dose in electrons per Angstrom, $\delta 2$ is the pixel area and I is absolute square of the wavefunction. The simulation does not include other sources of noise e.g. thermal noise.

9 display the final simulated image

```
In [9]: img=img.astype(np.float32)
        plt.imshow(img.T,extent=img_wave.get_extent(),cmap='gray')
        plt.xlabel('x [Anstrom]')
        plt.ylabel('y [Anstrom]')
        plt.show()
```

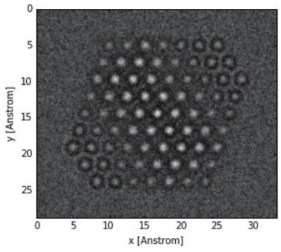

Appendix B Particle morphology

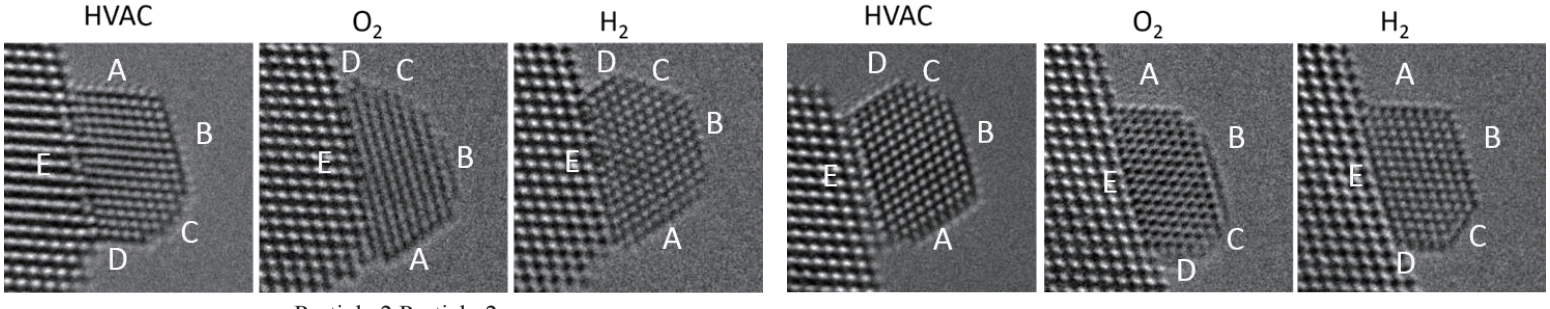

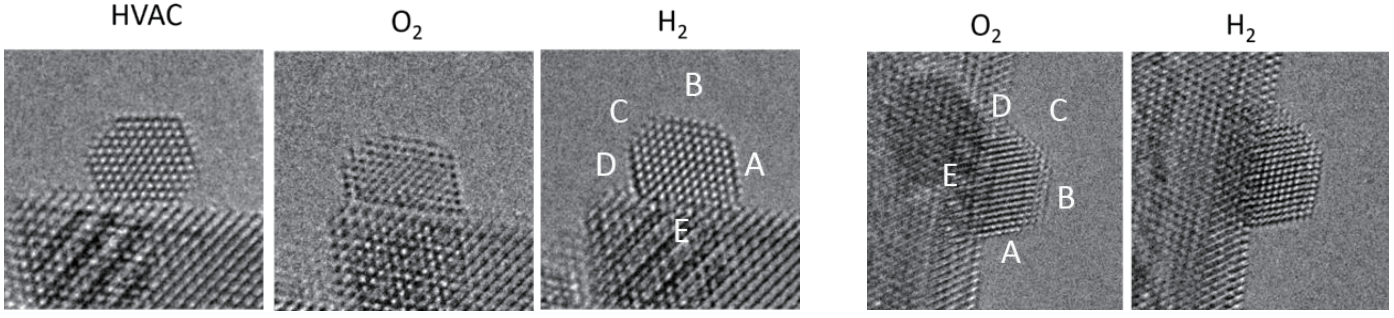
HVAC
O_2
H_2
B
C
D
A
E
O_2
H_2
D
C
E
B
A

Particle No.	O2	H2	O2	H2	O2	H2	O2	H2	O2	H2	O2	H2
	A	A	B	B	C	C	D	D	E	E	A/E	A/E
1	7	9	12	10	3	4	6	5	15	14	0.466667	0.642857
2	7	11	9	9	6	6	2	5	16	15	0.4375	0.733333
3	9	10	10	9	3	5	7	5	15	13	0.6	0.769231
4	12	13	10	15	10	7	5	5	25	22	0.48	0.590909
5	8	9	12	10	7	4	2	7	16	15	0.5	0.6
6	11	13							38	36	0.289474	0.361111
7	8	10	10	8	5	4	4	7	14	12	0.571429	0.833333

Paper List

Papers of the Ph.D. project

Madsen, J., **Liu, P.,** Wagner, J. B., Hansen, T. W. & Schiøz, J. Accuracy of surface strain measurements from transmission electron microscopy images of nanoparticles. Adv. Struct. Chem. Imaging 3, 14 (2017).

Madsen, J., **Liu, P.,** Kling, J.,Wagner, J. B., Hansen, T. W., Winther, O. & Schiøz, J. A deep learning approach to identify local structures in atomic-resolution transmission electron microscopy images. In preparation.

Other papers

Shkondin, E.; Takayama, O.; Panah, M. E. A.; **Liu, P.**; Larsen, P. V; Mar, M. D.; Jensen, F.; Lavrinenko, A. V. Large-Scale High Aspect Ratio Al-Doped ZnO Nanopillars Arrays as Anisotropic Metamaterials. *Opt. Mater. Express* **2017**, *7* (5), 1606.

Tiddi, W.; Elsukova, A.; Le, H. T.; **Liu, P.**; Beleggia, M. ; Han, A. P. Organnic ice resists. *Submitted to Nano Letters.*

Madsen *et al. Adv Struct Chem Imag (2017) 3:14*
DOI 10.1186/s40679-017-0047-0

Advanced Structural and Chemical Imaging

RESEARCH Open Access

Accuracy of surface strain measurements from transmission electron microscopy images of nanoparticles

Jacob Madsen[1*], Pei Liu[2], Jakob B. Wagner[2], Thomas W. Hansen[2] and Jakob Schiøz[1]

Abstract

Strain analysis from high-resolution transmission electron microscopy (HRTEM) images offers a convenient tool for measuring strain in materials at the atomic scale. In this paper we present a theoretical study of the precision and accuracy of surface strain measurements directly from aberration-corrected HRTEM images. We examine the influence of defocus, crystal tilt and noise, and find that absolute errors of at least 1–2% strain should be expected. The model structures include surface relaxations determined using molecular dynamics, and we show that this is important for correctly evaluating the errors introduced by image aberrations.

Keywords: High-resolution transmission electron microscopy, Strain mapping, Nanoparticles, Surface strain

Background

The surface lattice strain in nanostructures as a topic of research has gained increased interest in recent years due to its significant impact on many material properties. As an example, surface strain is a possible tunable parameter that can be used to optimize the adsorption energies of surfaces for a particular catalytic reaction [1]. Platinum-based oxygen reduction catalysis is improved by weakening the binding of adsorbed oxygen intermediates by 0.1 eV, this can be achieved by a 2% compressive strain [2]. Strain in nanoparticles can be generated by a variety of sources: particle size, shape, twinning, by the lattice mismatch between metals in multimetallic core–shell nanoparticles or it can be induced by the supporting substrate [3]. Characterizing the influence of these effects requires a technique capable of measuring structural information at atomic resolution.

High-resolution transmission electron microscopy (HRTEM) has become a routine tool for determining the structure of materials at an atomic scale [4]. TEM is particularly attractive due to the ability to map local strain. However, TEM images are the result of a complex diffraction and aberration-limited imaging process, and hence considerable care needs to be shown when extracting quantitative information.

An approach to overcome this is to iteratively compare experimental images with simulations [5, 6]; imaging parameters and model structure of the sample are refined until the simulated and experimental image match. This method has been successfully applied to determine various structures including surfaces. Another solution is to reconstruct the exit wave from a focal series, to eliminate the effect of aberrations [7]. However, the additional complexity added by such methods has limited their use. Instead an often used approach is to obtain the atomic positions directly from the experimental images. The positions of the intensity extrema within the image depend on imaging conditions, orientation and sample thickness, hence they do not necessarily coincide with the atomic positions. However, in the periodic part of a solid, a constant spatial relationship can still be assumed between the image and the atomic positions. This assumption breaks in areas with thickness variations, defects and in particular in the vicinity of surfaces and interfaces [8] and thus a systematic assessment of the accuracy is needed for these cases.

*Correspondence: jamad@fysik.dtu.dk
[1] Department of Physics, Technical University of Denmark, Fysikvej, Building 311, 2800 Kongens Lyngby, Denmark
Full list of author information is available at the end of the article

A first investigation to determine the accuracy with which surface strain could be determined was undertaken by Marks [9]. Image simulations were used to compare actual relaxations, in the input structural models, with apparent relaxations, measured from the corresponding simulated images. He found that there was a linear relationship between apparent and real strain, with a constant outward shift of about 5%. He also demonstrated that the true positions of atomic columns at the surface could be determined within 0.2 Å, corresponding to 5% of the lattice parameter of gold. This investigation was done before the invention of the spherical aberration corrector, which today has made it feasible to measure surface relaxations on the order of a few percent.

Newer investigations on the accuracy of strain analysis directly from HRTEM images have focused on interfaces in heterostructures [8, 10–12]. The error in such cases was found to be as low as 0.5% [13, 14]. Using a new technique based on Fourier transforming several overlapping sliding windows, it has been demonstrated that picometric precision and accuracy of interatomic distances can be achieved for measurements inside periodic solids [15]. However, these studies do not investigate surfaces and generally assume a uniform thickness. Moreover, in all these cases the strain distributions were fundamentally 2D, i.e. the atomic columns were mainly displaced in the plane perpendicular to the zone axis. This is different from nanoparticles where the true 3D strain is projected as a 2D image.

The literature has several examples of studies using aberration-corrected microscopy that includes measurements of strain in nanoparticles, and in the vicinity of surfaces, these measurements are often backed by comparison with a simulation that approximates the experimental structure and microscope conditions [16–19]. The general conclusion is that the erroneous surface strain due to imaging aberrations is much smaller in aberration-corrected images than the 5% found by Marks. However, these studies lack a systematic analysis of the sensitivity to experimental variables.

In the present work, we evaluate the accuracy of strain analysis directly from simulations of aberration-corrected HRTEM images focusing on surfaces of nanoparticles. The simulated objects are gold nanoparticles, which in addition to being a topic of research in their own right, provides a model structure that has different exposed surfaces and a linear thickness gradient. We examine the influence of four different effects: defocus, particle size, crystal tilt and noise, and we investigate what accuracy can be expected under which imaging and sample conditions.

Methods

Image simulation

Model and temperature effects

The overall shape of the model clusters was determined using Wulff constructions. The models were placed in a computational cell with 5 Å vacuum on all sides of the particle, see Fig. 1. Real metal surfaces are not simply ideally truncated crystals; experimental studies have demonstrated that the surface layer of many clean transition metals relaxes inward [20], while expansion of the top layer has been found for some surfaces of noble metals [21], including the {111} facets of gold. It has been proposed that expansive surface strains in small decahedral gold nanoparticles are a contributor to their catalytic activity [22].

In this study the ideal crystals were relaxed using molecular dynamics (MD) with an empirical potential. The interactions between the atoms were calculated with the charge-optimized many body (COMB) potential [23]. The potential parameters were fitted with a high priority for surfaces and nanoparticles, and hence reproduce the experimental surface relaxations of gold quite well. For an infinitely extended {111} surface, the potential predicts a 1.2% surface expansion of the top layer, which is close to the experimental value of 1.3% [24]. For {100} surfaces an

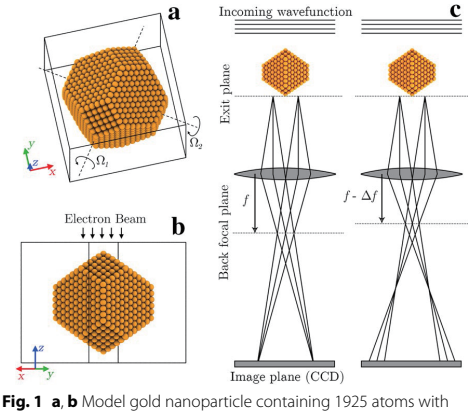

Fig. 1 **a**, **b** Model gold nanoparticle containing 1925 atoms with a diameter of 4 nm. The electron beam travels in the negative *z*-direction. The full lines indicate the computational cell and the dashed lines indicate the rotation axes denoted Ω_1 and Ω_2. **c** The HRTEM images are simulated by propagating the incoming plane wave through the sample potential using the multislice algorithm. The resulting wave at the exit plane is transferred through the objective lens to the detector using the CTF. Defocus is given relative to the bottom of the nanoparticle, with a positive defocus referring to propagation toward the detector

inward relaxation of 1.1% is predicted. There is no corresponding experimental value; however, the prediction is close to 1.2% [25] and 1.51% [26] calculated with density functional theory.

The effect of finite temperature is included using the frozen phonon approximation [27]. This is a semi-classical model based on the assumption that a single high-energy electron passing through the specimen at about half the speed of light can only probe a single frozen "snapshot" of the vibrating crystal. The image is produced by averaging incoherently over many snapshots where the atoms are slightly displaced from their equilibrium positions. The frozen phonon model has been shown to be numerically equivalent to the full quantum-mechanical treatment of the inelastic phonon scattering process [28]. The snapshots are typically determined using the Einstein approximation; however, we chose to use random steps from a constant temperature MD simulation using Langevin dynamics at 300 K [29]. We only used steps after the initial equilibration and the simulation was run for long enough to properly represent the thermal distribution of the atomic positions. We found that the simulated images are converged when ~ 40 snapshots are included in the averaging.

During a MD simulation the projected atomic positions follow a 2D normal distribution. The standard deviation of this distribution is around 0.05 Å or approximately 2% of the distance between the columns. The standard deviation of the distributions is not identical for all columns. It can be approximately 30–40% larger for some surface and corner atoms (see Additional file 1: Figure S3). We find that the difference between the mean relaxed positions and the mean positions obtained from a thermal average is just a constant thermal expansion of the entire crystal.

Diffraction and objective lens aberrations

The exit waves were simulated with the multislice algorithm [30] using the QSTEM code [31]. This code has been interfaced with Python and utilizes the atomic simulation environment [32] for setting up model structures, providing a single environment for building models, simulating and analysing images. The code is publicly available.[1] We have also made code available for directly recalculating and analysing a selection of the results from this paper.

The electrostatic potential of the sample was generated using the independent atom model with the parametrizations of Rez et al. [33]. The potential was generated on a 3D grid before slicing, allowing for accurate simulations of tilted samples. Aberrations due to the objective lens were included by Fourier space multiplication with the contrast transfer function (CTF). The effect of a finite source size and energy spread (i.e. partial spatial and temporal coherence) was included in the Quasi-coherent approximation where envelopes are applied to the wave function [34]. The imaging process is illustrated in Fig. 1c.

The microscope conditions were modelled after an image aberration-corrected FEI Titan microscope operated at 300 kV. Unless otherwise stated, the third-order spherical aberrations were set to $C_s = -10$ μm and all other aberrations except for defocus were set to zero. Other aberrations are generally not negligible in aberration-corrected microscopy; however, we chose to neglect them in order to keep the degrees of freedom limited. We tested the stability of our results to inclusion of additional aberrations, in particular twofold astigmatism on the order of 5–10 nm and 5th-order spherical aberrations on the order of 2.5 mm. While some results change slightly, we found that inclusion of additional aberrations does not change our conclusions in significant ways.

The focal spread was $\Delta = 2.9$ nm and the convergence angle was set to 15 mrad. The sampling used for the simulations was at least 0.05 Å/pixel, and when needed the large simulated images were downsampled using bilinear interpolation.

MTF and thermal magnetic noise

A single electron can cause a signal in more than one pixel of the CCD due to multiple scattering in the scintillator material. This effect can be described by the modulation-transfer function (MTF). A typical MTF can be parametrized as the sum of a Gaussian and an exponential [35]

$$\mathrm{MTF}(q) = a\exp(-bq) + (1-a)\exp(-c^2q^2), \qquad (1)$$

where q is the spatial frequency and the parameters are taken as $a = 0.58$, $b = 2.5$ Å and $c = 5.9$ Å.

An additional blurring can be caused by all kinds of noise that lead to a random deflection of the image relative to the detector. The origin of these aberrations are vibrations and drift of the stage, time-dependent fields resulting from instabilities of the lens currents and in particular thermal magnetic noise resulting from magnetic fields due to eddy currents in the material of the lenses [36]. The blurring is modelled by a Gaussian envelope on the intensity distribution [37]

$$\mathcal{N}(q) = \exp(-(2\pi\sigma)^2q^2), \qquad (2)$$

where σ denotes the standard deviation, and a value of $\sigma = 0.25$ Å has been assumed. It has been shown that including the MTF and a Gaussian blur can account for the so-called Stobbs factor [38], the ubiquitous contrast

[1] https://github.com/jacobjma/PyQSTEM.

mismatch between experimental and simulated images [39]. Since these effects can drastically reduce the contrast, they are important to include for accurately quantifying the influence of noise.

Finite electron dose

We assume that the noise is dominated by shot noise, and hence the measured electron count in each pixel can be modelled by a Poisson distribution [40]. The average number of electrons N collected by the ith detector pixel is given by

$$N_i = D\delta^2 I_i, \tag{3}$$

where D is the dose in electrons per area, δ is the sampling and I_i is the probability for an electron hitting the i'th pixel. The signal-to-noise ratio of the whole image is given by [41]

$$\mathrm{SNR} = \frac{\bar{N}}{\sigma(N)}, \tag{4}$$

where $\bar{N}$ is the average number of electrons per pixel and $\sigma(N)$ is the standard deviation of the number of electrons collected by each pixel. In the limit of low dose this can be reduced to [42]

$$\mathrm{SNR} = \sqrt{\bar{N}} = \sqrt{DI}\delta, \tag{5}$$

whereas in the limit of high dose other sources of noise are dominant (e.g. thermal noise) and the SNR becomes constant. We are only including shot noise in the simulations.

Strain analysis

There are several different approaches for obtaining strain directly from HRTEM images. The methods can broadly be classified into three different types: direct measurement of interatomic distances in real space [43, 44], extraction of the lattice by comparison to a template [45] and analysis in Fourier space [46]. The results of the different approaches are similar inside periodic structures, but can differ in the presence of defects [44]. In this paper the real space method is used, since it has the most straight forward interpretation for surfaces, where the results of Fourier space analysis are very opaque. A comparison between real and Fourier space analysis, using geometric phase analysis (GPA), is provided as supplementary information (see Additional file 1: Figure S4).

The most critical step in the real space approach is to determine the positions of the lattice points. There are several ways of defining these positions. However, the simplest way is to define them as the position of the intensity extrema, assumed to correspond with an atomic column. If the lattice points do not correspond to single intensity peaks, they can instead be found using a cross-correlation of the image with a template motif [8]. The intensity extrema are found at sub-pixel accuracy by fitting a 2D function, usually a polynomial or a Gaussian, to the neighbourhood of each peak and setting the derivatives to zero [44]. It is also possible to define the lattice positions from the centre of mass of the intensity distributions [47]. The methods agree if the intensity distributions are symmetric. However, this is not necessarily the case close to asymmetries in the lattice, such as an interface. A comparison of the two methods of measuring the atomic positions is included as supplementary information. The conclusion is that the methods lead to slightly different errors; however, the magnitude of the errors is essentially the same.

The peak pairs algorithm [44] is the most popular method for finding strain from a set of 2D lattice points from HRTEM images. For the calculation of strain at every lattice point, the peak pairs algorithm uses only two lattice vectors. We have found that an approach using a larger number of lattice vectors is significantly more stable in the presence of noise. For an fcc crystal in the [48] zone axis, this method uses the four nearest and two second nearest neighbours to find the strain at any lattice point in the bulk. Another advantage of this method is that it allows us to determine the strain for lattice points at all surfaces and corners, which is not possible with the standard implementation of the peak pairs algorithm. The routines used for strain analysis, including a rudimentary implementation of GPA, are implemented in Python and made available as open source.[2]

The strain is computed at each lattice point, by comparing the positions of the neighbouring lattice points in an ideal template lattice to the corresponding measured lattice points. In practice, this is done by finding the optimal affine transformation, $\mathbf{A}$, between the two sets of vectors, see Fig. 2. In general finding $\mathbf{A}$ is an overdetermined problem, hence it is found as the best fit to a least-squares fit of the form:

$$r = \min_{\mathbf{A}} \sum_{i}^{N} \|\mathbf{A}\mathbf{v}_i - \mathbf{w}_i\|, \tag{6}$$

where r is the residual term, v_i and w_i are vectors containing the ideal and actual lattice vectors, $\mathbf{A}$ is the affine transformation and $\|\cdot\|$ denotes the Euclidean norm. The orientation and elastic strain matrices can be extracted from $\mathbf{A}$ via a left-sided polar decomposition of the deformation gradient

$$\mathbf{P}\mathbf{U} = \mathbf{A}, \tag{7}$$

[2] https://github.com/jacobjma/structural-template-mapping.

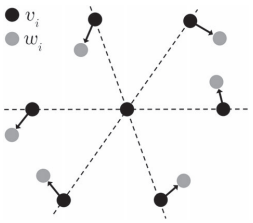

Fig. 2 The black points indicate the ideal lattice for an fcc crystal in the [48] zone axis. The grey points are the positions of slightly displaced lattice points for a strained crystal. The strain at the central lattice point is calculated by finding the optimal affine transformation between the black and grey points, denoted by *v* and *w*, respectively

where $\mathbf{U}$ is an orthogonal right-handed matrix (the rotation matrix), and $\mathbf{P}$ is a symmetric matrix (the elastic strain matrix). Finding the correspondence between $\boldsymbol{v}$ and $\boldsymbol{w}$ is done using a branch and bound search method. A similar 3D equivalent of the method is described by Larsen et al. [48].

To limit the amount of results that have to be shown, we will usually just show the planar strain, ϵ_{p}, calculated as the average of the normal strains in the x- and y-direction

$$\epsilon_{\mathrm{p}} = \frac{1}{2}(\epsilon_{xx} + \epsilon_{yy}). \tag{8}$$

Surface relaxations are the strain at the outermost atoms in the direction perpendicular to the same surface. Hence, the surface relaxation associated with an atom on a surface perpendicular to the unit vector $\hat{\boldsymbol{n}}$ is found as

$$\epsilon_{\hat{\boldsymbol{n}}} = \hat{\boldsymbol{n}}^{\mathrm{T}} \boldsymbol{\epsilon} \hat{\boldsymbol{n}}. \tag{9}$$

We are mainly interested in the strain measurement errors, but to define the errors, we first need to define the true strain. An image provides a single viewpoint of the structure, where each atomic column appears as a dot, hence we can only hope to measure an average column position for the atoms belonging to each column. Defining these averages to be the true column positions, the corresponding planar strain will be denoted as $\epsilon_{\mathrm{p,\,true}}$. The strain calculated from the positions of the maxima in the matching image will be denoted as $\epsilon_{\mathrm{p,\,measured}}$. From these definitions, we define the error of a strain measurement as

$$\mathrm{error}\,(\epsilon_{\mathrm{p}}) = \epsilon_{\mathrm{p,\,measured}} - \epsilon_{\mathrm{p,\,true}}. \tag{10}$$

Results

Influence of relaxations and temperature effects

When image simulations are used to estimate errors due to aberrations, it is a common practice to use a model of an unrelaxed crystal, under the assumption that the errors caused by these aberrations are insensitive to the small difference between the unrelaxed and relaxed crystal [16–19]. Our results demonstrate that this assumption is invalid in general.

The comparison in Fig. 3 shows the difference between results based on an ideal crystal, a relaxed crystal and an average over thermal vibrations. There is a substantial difference between the exit wave intensities. This difference is less obvious in the final images; however, it is large enough to have an impact on the measured strain and more notably on the measurement errors. This means that using the ideal particle to calibrate a strain measurement would lead to wrong conclusions about the measurement errors.

The origin of the errors is deviations from the constant spatial relationship between the image and the underlying projected potential. The peaks are generally more asymmetric for both the image resulting from a relaxed crystal and from a thermal average of crystals, and these small irregularities in the symmetry of adjacent intensity peaks can cause large measurement errors, as illustrated in Fig. 4. All results in the following sections will be based on simulations where temperature effects are included. We also note the $\sim 50\%$ reduction of the image contrast due to thermal vibrations, making the influence of temperature on the image contrast approximately as important as the MTF and thermal magnetic noise.

The strain calculated from the true average projected column positions is shown in Fig. 5a for three different particle diameters. The strain calculated from the projected positions seems to show a significant compressive strain in the bulk of the particle; however, this is misleading. Figure 5b shows the strain calculated directly from the full 3D model for a slice through the centre of the nanoparticle; comparing the strain in the 3D model to the projected strain reveals that the apparent bulk compressive strain is due to relaxations closer to the front and back surface. Hence, even disregarding image aberrations, comparing Fig. 5a, b shows that care has to be taken, when interpreting strain measurements from HRTEM images. The errors in the following sections are calculated with respect to the strain in the projected positions and are thus mainly due to image aberrations.

Influence of defocus

The top row of Fig. 6 shows simulated images at different defocus and the bottom row shows the error in the planar strain measured from these images. The smallest defocus shown is 4.5 nm since contrast inversion begins to take effect for a smaller defocus. We present results for only a positive defocus, which leads to images with bright spots at the positions of the atomic columns. We have

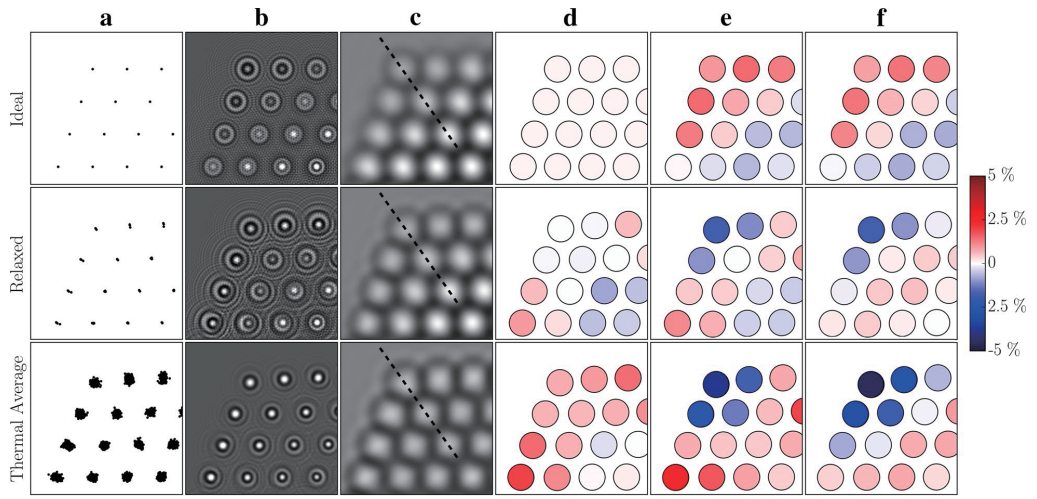

Fig. 3 From top to bottom, the rows contain results relating to an ideal crystal, a relaxed crystal and a thermal average of crystals. Each of the panels show a small section of the corner between two {111} facets. Along the columns we show: **a** the projected positions of the atoms, all the positions used in the thermal average are included. **b** Intensities of the exit waves. **c** Simulated images for a defocus $\Delta f = 14.5$ nm. **d** The true planar strain, $\epsilon_{p,\,true}$, i.e. the strain calculated directly from the projected positions of the model crystal. The colour coding shared by all the columns is shown to the right of the figure. **e** The measured planar strain, $\epsilon_{p,\,measured}$, i.e. strain calculated from the measured positions of the intensity maxima in simulated images. **f** The measurement error of the planar strain, error(ϵ_p), calculated as the difference between the strain shown in the two preceding columns

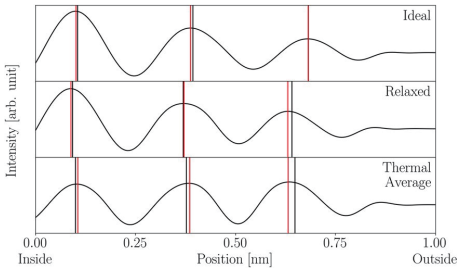

Fig. 4 Slices along the dashed lines in Fig. 3. The black vertical lines indicate the true atomic positions and the red vertical lines indicate the corresponding measured maxima positions. For the ideal model the measured distance between the outermost peaks is too large by 0.006 nm or 2% of the interatomic distance in the slice direction. For the images that include temperature effects, the same measurement is too small by 0.025 nm or 10% of the interatomic distance

obtained results for negative defocus as well, where the atoms appear as black spots on a lighter background. The results are shown in Additional file 1: Figure S5.

A defocus of 8.5 nm results in planar strain errors smaller than 1% everywhere, while a defocus of 12.5 nm causes significant errors at the {100} facets. Due to the sign and location of these errors, they could easily be mistaken for real surface relaxations. The errors generally stay small for columns not at the surface; however, at larger defocus some errors start to appear, generally following the thickness gradient.

The error in the measured surface relaxations averaged across the facets for the uppermost atomic layers is shown as a function of defocus in Fig. 7. Since this error can vary quite a bit across the {111} facets, we also show the corresponding standard deviation. Results for 3 different particle sizes are shown, from a diameter of ~ 2 nm to a diameter of ~ 6 nm.

For the {100} facet the error is almost zero up to a defocus of 8.5 nm, across all three particle sizes. Meanwhile the error for the {111} facet never becomes smaller than 1% for the 4 nm particle, which is approximately the same magnitude as the actual relaxations. For both facets and all sizes, the errors stay below 2% up to a defocus of ~ 11 nm, where the mean error increases sharply at the {100} facets. The mean error does not increase as drastically for the {111} facets. On the other hand, the standard deviation does increase. This is mainly due to the thickness variation along these facets.

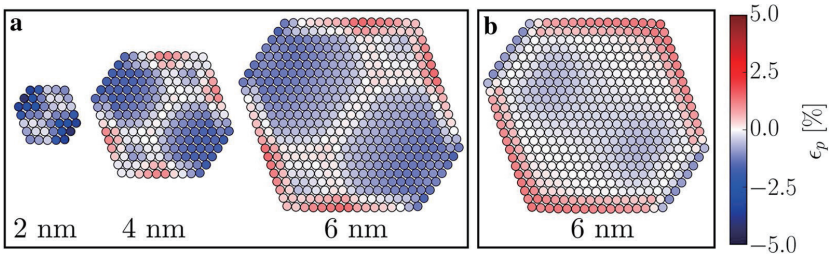

Fig. 5 **a** The "true" planar strain, $\epsilon_{p,\text{true}}$, calculated from the average projected column positions of the model, for three different nanoparticle diameters. **b** The actual planar strain for a slice through the 3D model

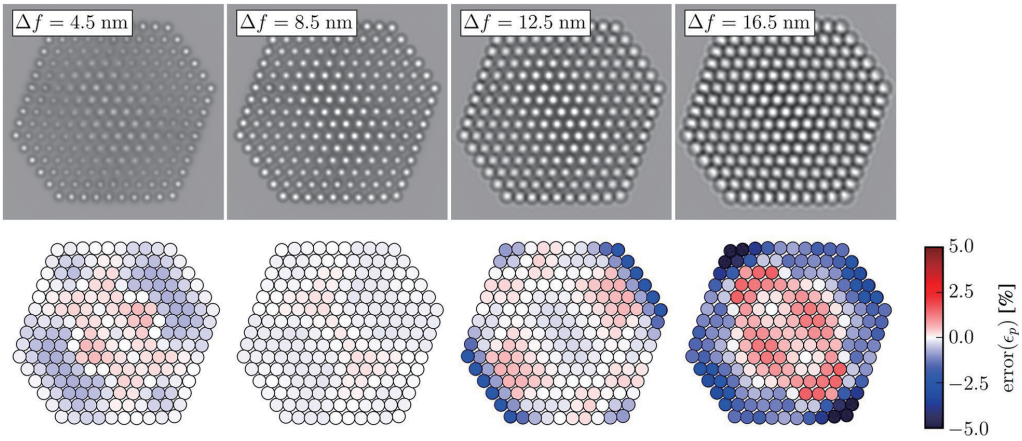

Fig. 6 The top row shows simulated images for a nanoparticle with a diameter of 4 nm. The bottom row shows the corresponding distribution of errors in the planar strain. The defocus is different in each column, as indicated in the figure

Influence of tilt

It is unavoidable that the sample will be slightly tilted relative to the ideal zone axis. Figure 8 shows the distribution of errors in the planar strain for increasing tilt, α, around the Ω_1-axis. At tilt $\alpha = 1.0°$, the errors have changed very little compared to the untilted crystal, though the appearance of the image have changed in the central part of particle, this is due to an effective diminishing of the projected potential, as have been reported elsewhere [49]. The errors stay small up to a tilt $\alpha = 2.0°$, but increase sharply in the centre of the nanoparticle between $\alpha = 2.0°$ and $\alpha = 3.0°$. The error introduced by tilt is very dependent on the height of the atomic columns, since the length of the footprint of the projection of a tilted column increases linearly with its height. Only one direction of tilt is shown; however, the trends are similar for other tilt directions. One other tilt directions is included as Additional file 1: Figure S6.

Figure 9 shows the effects of tilt on the errors in the measured surface relaxations for a defocus $\Delta f = 8.5$ nm. The tilt has a relatively limited impact on the measured surface relaxations. The mean and standard deviation of error changes by at most 1% over the entire tilt range. The effects of tilt on the strain measurements are very dependent on defocus. For example at a defocus $\Delta f = 14.5$ nm, the mean surface relaxation error changes by more than 6% at the {100} facets, a plot showing this is shown in Additional file 1: Figure S7.

Influence of noise

The evolution of the object visibility with respect to the sampling and dose is shown in Fig. 10a. At a dose of 10^2

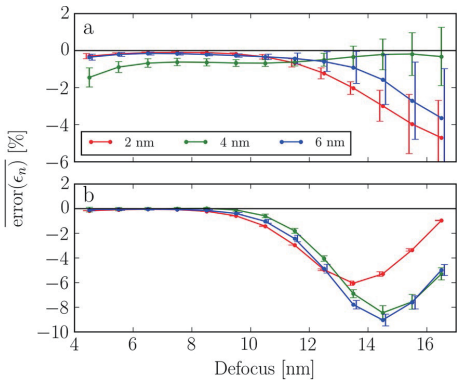

Fig. 7 The error in the measured surface relaxations averaged across the facets as a function of defocus, for the three particle sizes given in the legend, for: **a** the {111} facets and **b** the {100} facets. The bars indicate the standard deviation of the errors in the surface relaxation error across the facets. The bars are shifted slightly from the points for visual clarity

$e^-/\text{Å}^2$ the object is barely visible, while the images are essentially unaffected by noise at $10^5\, e^-/\text{Å}^2$.

Noise removal is essential to obtain the stable polynomial fits necessary for sub-pixel resolution; hence we show the same noisy images after application of a Wiener filter in Fig. 10b [50]. The regularization of the filter was chosen to be optimal for each of the different samplings, but was not changed with the amount of noise.

To determine the influence of dose on the errors in strain measurements, we simulate a statistically representative ensemble of images, $K = 300$, with different distributions of noise. The error due to noise is quantified using the mean absolute error, MAE, over the ensemble of images for each lattice point

$$\text{MAE}_i = \frac{1}{K}\sum_{k=0}^{K} \left|\epsilon_{k,i} - \epsilon_{\infty,i}\right|, \tag{11}$$

where $\epsilon_{k,i}$ is the planar strain at the i'th lattice point measured from the kth noisy image and $\epsilon_{\infty,i}$ is the corresponding measured strain without noise. Since the automatic polynomial fitting can fail at low doses, extreme outliers have been removed before taking the average. Figure 11 shows the distribution of the MAE across a nanoparticle, there is a fairly large difference between the MAE for different lattice points, varying by a factor of three between the centre of the particle and a corner. The reason for this is mainly that the strain at surfaces is determined on the basis of fewer surrounding lattice points. The strain at corner atoms is determined on the basis of just three neighbours, while the measurements in the centre rely on twice that number of neighbours.

The MAE at three chosen lattice sites as a function of dose is shown in Fig. 12. We find a simple approximate empirical relationship, assuming constant sampling, between the MAE and the dose

$$\text{MAE} \propto \frac{1}{\sqrt{D}} \propto \frac{1}{\text{SNR}}, \tag{12}$$

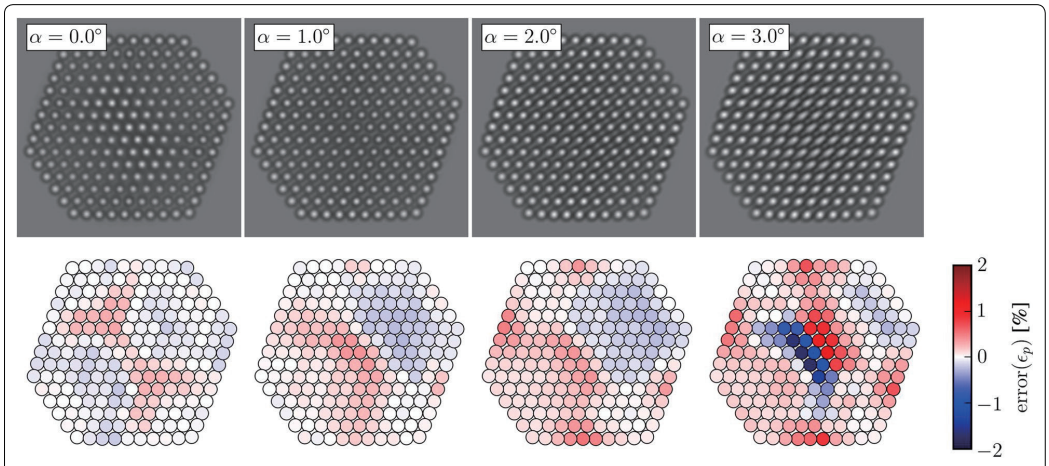

Fig. 8 The top row shows simulated images at increasing tilt around the Ω_T-axis for a defocus $\Delta f = 8.5$ nm. The bottom row shows the error in the planar strain at each lattice point measured from these images

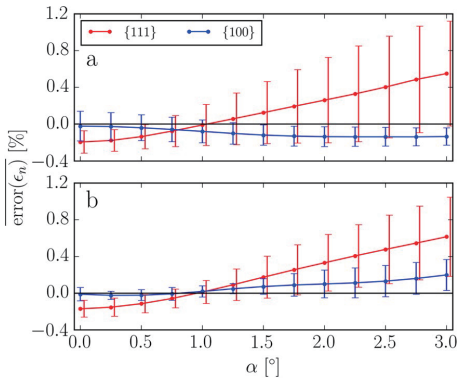

Fig. 9 The error in the measured surface relaxations averaged across the facets as a function of tilt, around the axes (**a**) Ω_1 and (**b**) Ω_2. The defocus was $\Delta f = 8.5$ nm. The curves are for the {100} and {111} facets, as indicated by the legend

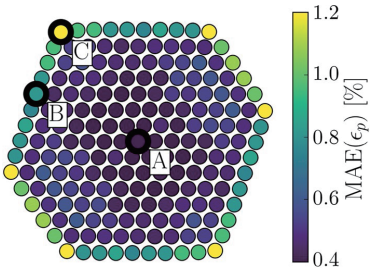

Fig. 11 The MAE of the planar strain due to noise at each lattice point for a Wiener filtered noisy image at a sampling of 0.2 Å/pixel, a dose of $10^3\, e^-/\text{Å}^2$ and a defocus $\Delta f = 8.5$ nm

where the constant of proportionality is determined by the number of neighbours, local image contrast and sampling. The second approximate proportionality assumes low dose and is due to Eq. (5).

Given that the SNR depends linearly on the sampling [see Eq. (5)], the expression above might lead one to expect that coarser sampling would give smaller MAE. This is however not the case, as shown in Fig. 13 where the MAE is plotted as a function of sampling for different doses. The relationship is fairly constant though a sampling of 0.2 Å/pixel is better than both a rougher or a finer sampling. The main reason that there is no decrease in the MAE as the sampling gets coarser is that the better SNR is compensated by a smaller number of pixels across each peak available for polynomial fitting.

In the previous sections, we saw that the defocus should be kept small to obtain strain measurements that are relatively unaffected by aberrations. The disadvantage of this is that phase contrast imaging relies on the additional phase added by the objective lens, and hence a too small defocus will negatively impact the image contrast. This effect is illustrated in Fig. 14 where the change in the visibility of the nanoparticle is shown with respect to

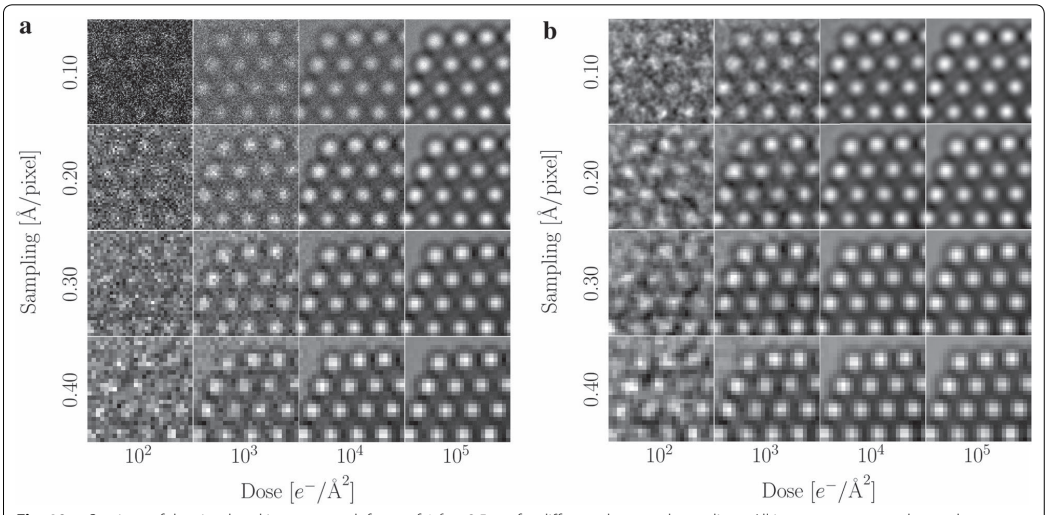

Fig. 10 **a** Sections of the simulated images at a defocus of $\Delta f = 8.5$ nm for different doses and samplings. All images are mapped onto the same range of grey levels. **b** The same images after applying a Wiener filter

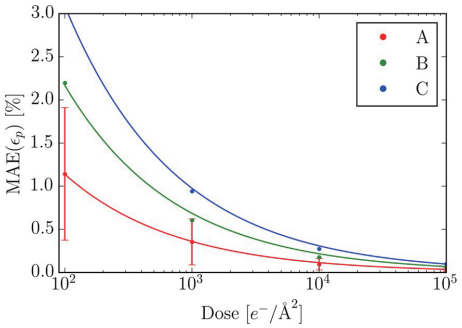

Fig. 12 The MAE as a function of the dose for the three lattice points, *A*, *B* and *C*, as indicated in Fig. 11. The dots show the MAE calculated from the simulated images and the full lines are curves of the form given by Eq. (12), where the constant of proportionality has been fitted to the dots. The bars indicate the standard deviations, which for visual clarity are shown only for lattice point *B*, proportionally the standard deviations are similar for the other lattice points

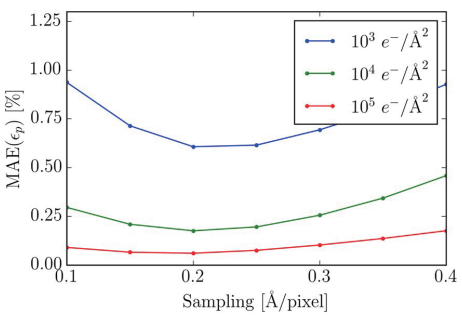

Fig. 13 The MAE as a function of the sampling for five different doses at the *B* lattice point (see Fig. 11). The defocus was $\Delta f = 8.5$ nm and the sampling was 0.2 Å/pixel

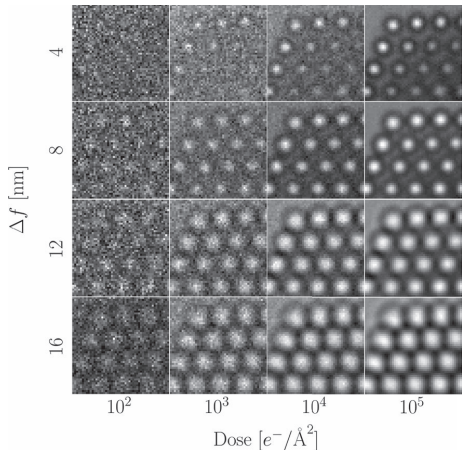

Fig. 14 Sections of simulated HRTEM images for different doses and defocus at a sampling of 0.2 Å/pixel. All images are mapped onto the same range of greys

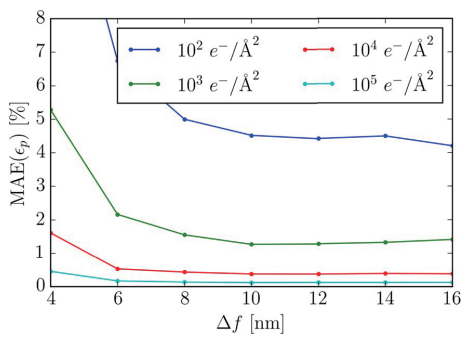

Fig. 15 The MAE as a function of defocus for four different doses at a sampling of 0.2 Å/pixel at the lattice point B

defocus and dose. The corresponding errors are quantified in Fig. 15. At a low dose, the errors grow very large when the defocus is small, but even at a higher dose, errors due to noise become present when the defocus is too small. When the defocus is increased the MAE becomes smaller, however saturation is reached relatively quickly, and additional defocus beyond $\Delta f = 8$ nm does not further improve the MAE.

Conclusion

We looked at the accuracy of surface strain measurements from HRTEM images of nanoparticles. We showed that the practice of using simulations based on ideal sample models to calibrate strain measurements is problematic, since the predicted errors from such simulations do

not in general reflect the errors for an identical model that includes relaxations.

In general, the impact of the interaction between tilt, thickness and defocus on the final strain measurement is very complicated. However, we observe that if the defocus is small enough, the errors in the measured surface relaxations due to image aberrations can be kept at less than 2%, even for visually obvious tilts. This is significantly larger than the 0.5% that have been found for strain measurements inside periodic solids [13]. The main reason for the larger error is the asymmetry in the peaks close to surfaces.

In order to obtain measurements with small errors, the defocus should not be chosen solely to maximize contrast, since this will also cause large errors due to aberrations. The choice of defocus has to balance delocalization and contrast; if the defocus is too small the contrast will suffer, while if defocus is too large the image aberrations will be the main source of error.

For a dose of $10^3\ e^-/\text{Å}^2$, the optimal defocus for the gold nanoparticles is somewhere around 8.5 nm; at this defocus the errors in the surface relaxations are below 2% and the expected noise error is 1.2% with a standard deviation 0.8%.

Additional file

Additional file 1. Section S1. Measuring the center of mass. **Figure S1.** Definition of integration regions for center of mass calculations. **Figure S2.** Comparison of center of mass positions with peak positions. **Figure S3.** Magnitudes of thermal vibrations. **Figure S4.** Comparison of our method with GPA. **Figure S5.** Negative defocus measurements. **Figure S6.** Planar strain errors for increasing tilt. **Figure S7.** Surface strain errors for increasing tilt.

Author's contributions

JM did the simulations. The data analysis was done by JM with inputs from the other authors. PL performed the experimental work that inspired this article. The manuscript was written by JM with contributions from the other authors. All authors read and approved the final manuscript.

Author details

[1] Department of Physics, Technical University of Denmark, Fysikvej, Building 311, 2800 Kongens Lyngby, Denmark. [2] Center for Electron Nanoscopy, Technical University of Denmark, Fysikvej, Building 311, 2800 Kongens Lyngby, Denmark.

Acknowledgements

Not applicable.

Competing interests

The authors declare that they have no competing interests.

Availability of data and materials section

The source code and algorithms used in this article are available in the repositories https://github.com/jacobjma/PyQSTEM and https://github.com/jacobjma/structural-template-mapping.

Ethics approval and consent to participate

Not applicable.

Funding

We gratefully acknowledge funding through Grant 1335-00027B from the Danish Council for Independent Research.

Publisher's Note

Received: 8 May 2017 Accepted: 5 October 2017
Published online: 25 October 2017

References

1. Mavrikakis, M., Hammer, B., Nørskov, J.K.: Effect of strain on the reactivity of metal surfaces. Phys. Rev. Lett. **81**(13), 2819–2822 (1998). doi:10.1103/PhysRevLett.81.2819
2. Hernandez-Fernandez, P., Masini, F., McCarthy, D.N., Strebel, C.E., Friebel, D., Deiana, D., Malacrida, P., Nierhoff, A., Bodin, A., Wise, A.M., Nielsen, J.H., Hansen, T.W., Nilsson, A., Stephens, I.E.L., Chorkendorff, I.: Mass-selected nanoparticles of PtxY as model catalysts for oxygen electroreduction. Nat. Chem. **6**(8), 732 (2014). doi:10.1038/nchem.2001
3. Sneed, B.T., Young, A.P., Tsung, C.-K., Romanov, A.E., Shalkovskii, A.G., Wang, J., Ma, Y., Xia, Y., Mao, S.X., Lee, B., Shevchenko, E.V., Liu, Z., Salmeron, M., Somorjai, G.A., Somorjai, G.A., Yang, P., Stamenkovic, V.R.: Building up strain in colloidal metal nanoparticle catalysts. Nanoscale **7**(29), 12248–12265 (2015). doi:10.1039/C5NR02529J
4. Smith, D.J.: Characterization of nanomaterials using transmission electron microscopy. In: Kirkland, A.I., Hutchison, J. (eds.) Nanocharacterization, 2nd edn, pp. 1–29. Royal Society of Chemistry, London (2015). doi:10.1039/9781782621867-00001
5. Möbus, G., Schweinfest, R., Gemming, T., Wagner, T., Ruhle, M.: Iterative structure retrieval techniques in HREM: a comparative study and a modular program package. J. Microsc. **190**(1–2), 109–130 (1998). doi:10.1046/j.1365-2818.1998.3120865.x
6. Van Aert, S., De Backer, A., Martinez, G.T., den Dekker, A.J., Van Dyck, D., Bals, S., Van Tendeloo, G.: Advanced electron crystallography through model-based imaging. IUCrJ **3**(Pt 1), 71–83 (2016). doi:10.1107/S2052252515019727
7. Bals, S., Aert, S.V., Tendeloo, G.V., Ávila-Brande, D.: Statistical estimation of atomic positions from exit wave reconstruction with a precision in the picometer range. Phys. Rev. Lett. **96**(9), 096106 (2006). doi:10.1103/PhysRevLett.96.096106
8. Du, K., Phillipp, F.: On the accuracy of lattice-distortion analysis directly from high-resolution transmission electron micrographs. J. Microsc. **221**(1), 63–71 (2006). doi:10.1111/j.1365-2818.2006.01536.x
9. Marks, L.D.: Direct atomic imaging of solid surfaces - 1. Image simulations and interpretation. Surf. Sci. **139**(1), 281–298 (1984)
10. Guerrero, E., Galindo, P., Yáñez, A., Ben, T., Molina, S.I.: Error quantification in strain mapping methods. Microsc. Microanal. **13**(05), 320–328 (2007). doi:10.1017/S1431927607070407
11. Tillmann, K., Lentzen, M., Rosenfeld, R., Peralta, P., McCartney, M.R., Drucker, J., Picraux, S.T.: Impact of column bending in high-resolution transmission electron microscopy on the strain evaluation of GaAs/InAs/GaAs heterostructures. Ultramicroscopy **83**(1–2), 111–128 (2000). doi:10.1016/S0304-3991(99)00175-8
12. Rosenauer, A., Gerthsen, D., Potin, V.: Strain state analysis of InGaN/GaN—sources of error and optimized imaging conditions. Phys. Status Solidi **203**(1), 176–184 (2006). doi:10.1002/pssa.200563519
13. Chung, J., Rabenberg, L.: Effects of strain gradients on strain measurements using geometrical phase analysis in the transmission electron microscope. Ultramicroscopy **108**(12), 1595–1602 (2008). doi:10.1016/j.ultramic.2008.05.010
14. Hÿtch, M.J., Plamann, T.: Imaging conditions for reliable measurement of displacement and strain in high-resolution electron microscopy. Ultramicroscopy **87**(4), 199–212 (2001). doi:10.1016/S0304-3991(00)00099-1

15. Klinger, M., Polívka, L., Jäger, A., Tyunina, M.: Quantitative analysis of structural inhomogeneity in nanomaterials using transmission electron microscopy. J. Appl. Crystallogr. **49**(3), 762–770 (2016). doi:10.1107/S1600576716003800
16. José Yacamán, M., Ascencio, J.A., Canizal, G.: Observation of surface relaxation surface steps and surface reconstruction in gold nanorods. Surf. Sci. **486**(1), L449–L453 (2001). doi:10.1016/S0039-6028(01)01048-2
17. Fujita, T., Guan, P., McKenna, K., Lang, X., Hirata, A., Zhang, L., Tokunaga, T., Arai, S., Yamamoto, Y., Tanaka, N., Ishikawa, Y., Asao, N., Yamamoto, Y., Erlebacher, J., Chen, M.: Atomic origins of the high catalytic activity of nanoporous gold. Nat. Mater. **11**(9), 775–780 (2012). doi:10.1038/nmat3391
18. López-Haro, M., Yoshida, K., del Río, E., Pérez-Omil, J.A., Boyes, E.D., Trasobares, S., Zuo, J.M., Gai, P.L., Calvino, J.J.: Strain field in ultrasmall gold nanoparticles supported on cerium-based mixed oxides. Key influence of the support redox state. Langmuir **32**(17), 4313–4322 (2016)
19. Du, K., Ernst, F., Pelsozy, M.C., Barthel, J., Tillmann, K.: Expansion of interatomic distances in platinum catalyst nanoparticles. Acta Mater. **58**(3), 836–845 (2010). doi:10.1016/j.actamat.2009.09.061
20. Martienssen, W., Warlimont, H.: Springer Handbook of Condensed Matter and Materials Data, 1st edn, p. 1119. Springer, Berlin (2005)
21. Nichols, R.J., Nouar, T., Lucas, C.A., Haiss, W., Hofer, W.A.: Surface relaxation and surface stress of Au(111). Surf. Sci. **513**(2), 263–271 (2002). doi:10.1016/S0039-6028(02)01510-8
22. Walsh, M.J., Yoshida, K., Kuwabara, A., Pay, M.L., Gai, P.L., Boyes, E.D.: On the structural origin of the catalytic properties of inherently strained ultrasmall decahedral gold nanoparticles. Nano Lett. **12**(4), 2027–2031 (2012). doi:10.1021/nl300067q
23. Liang, T., Shan, T.-R., Cheng, Y.-T., Devine, B.D., Noordhoek, M., Li, Y., Lu, Z., Phillpot, S.R., Sinnott, S.B.: Classical atomistic simulations of surfaces and heterogeneous interfaces with the charge-optimized many body (COMB) potentials. Mater. Sci. Eng. R Rep. **74**(9), 255–279 (2013). doi:10.1016/j.mser.2013.07.001
24. Vook, R.W., Ouyang, S., Otooni, M.A.: X-ray measurement of the (111) surface relaxation in gold. Surf. Sci. **29**(1), 277–290 (1972). doi:10.1016/0039-6028(72)90084-2
25. Yu, B.D., Scheffler, M.: Physical origin of exchange diffusion on fcc(100) metal surfaces. Phys. Rev. B **56**(24), 15569–15572 (1997). doi:10.1103/PhysRevB.56.R15569
26. Singh-Miller, N.E., Marzari, N.: Surface energies, work functions, and surface relaxations of low-index metallic surfaces from first principles. Phys. Rev. B **80**(23), 235407 (2009). doi:10.1103/PhysRevB.80.235407
27. Loane, R.F., Xu, P., Silcox, J.: IUCr: Thermal vibrations in convergent-beam electron diffraction. Acta Crystallogr. Sect. A Found. Crystallogr. **47**(3), 267–278 (1991). doi:10.1107/S0108767391000375
28. Van Dyck, D.: Is the frozen phonon model adequate to describe inelastic phonon scattering? Ultramicroscopy **109**(6), 677–682 (2009). doi:10.1016/j.ultramic.2009.01.001
29. Tadmor, E.B., Miller, R.E.: Modeling Materials : Continuum, Atomistic, and Multiscale Techniques, p. 759. Cambridge University Press, Cambridge (2011)
30. Goodman, P., Moodie, A.F.: Numerical evaluations of N-beam wave functions in electron scattering by the multi-slice method. Acta Crystallogr. Sect. A **30**(2), 280–290 (1974). doi:10.1107/S056773947400057X
31. Koch, C.: Determination of Core Structure Periodicity and Point Defect Density Along Dislocations. Arizona State University, Phd (2002)
32. Bahn, S.R., Jacobsen, K.W.: An object-oriented scripting interface to a legacy electronic structure code. Comput. Sci. Eng. **4**(3), 56–66 (2002). doi:10.1109/5992.998641
33. Rez, D., Rez, P., Grant, I.: IUCr: Dirac-Fock calculations of X-ray scattering factors and contributions to the mean inner potential for electron scattering. Acta Crystallogr. Sect. A Found. Crystallogr. **50**(4), 481–497 (1994). doi:10.1107/S0108767393013200
34. Kirkland, E.J.: Advanced Computing in Electron Microscopy. Springer, Boston (2010). doi:10.1007/978-1-4419-6533-2
35. Van den Broek, W., Van Aert, S., Van Dyck, D.: Fully automated measurement of the modulation transfer function of charge-coupled devices above the nyquist frequency. Microsc. Microanal. **18**(02), 336–342 (2012). doi:10.1017/S1431927611012633
36. Uhlemann, S., Müller, H., Hartel, P., Zach, J., Haider, M.: Thermal magnetic field noise limits resolution in transmission electron microscopy. Phys. Rev. Lett. **111**(4), 046101 (2013). doi:10.1103/PhysRevLett.111.046101
37. Haider, M., Hartel, P., Müller, H., Uhlemann, S., Zach, J.: Information transfer in a TEM corrected for spherical and chromatic aberration. Microsc. Microanal. **16**(04), 393–408 (2010). doi:10.1017/S1431927610013498
38. Hÿtch, M.J., Stobbs, W.M.: Quantitative comparison of high resolution TEM images with image simulations. Ultramicroscopy **53**(3), 191–203 (1994). doi:10.1016/0304-3991(94)90034-5
39. Thust, A.: High-resolution transmission electron microscopy on an absolute contrast scale. Phys. Rev. Lett. **102**(22), 220801 (2009). doi:10.1103/PhysRevLett.102.220801
40. Lee, Z., Meyer, J.C., Rose, H., Kaiser, U.: Optimum HRTEM image contrast at 20 kV and 80 kV-Exemplified by graphene. Ultramicroscopy **112**, 39–46 (2011). doi:10.1016/j.ultramic.2011.10.009
41. De Graef, M.: Introduction to Conventional Transmission Electron Microscopy, p. 718. Cambridge University Press, Cambridge (2003)
42. Lee, Z., Rose, H., Lehtinen, O., Biskupek, J., Kaiser, U.: Electron dose dependence of signal-to-noise ratio, atom contrast and resolution in transmission electron microscope images. Ultramicroscopy **145**, 3–12 (2014). doi:10.1016/j.ultramic.2014.01.010
43. Bierwolf, R., Hohenstein, M., Phillipp, F., Brandt, O., Crook, G.E., Ploog, K.: Direct measurement of local lattice distortions in strained layer structures by HREM. Ultramicroscopy **49**(1), 273–285 (1993). doi:10.1016/0304-3991(93)90234-O
44. Galindo, P.L., Kret, S., Sanchez, A.M., Laval, J.-Y., Yáñez, A., Pizarro, J., Guerrero, E., Ben, T., Molina, S.I.: The Peak Pairs algorithm for strain mapping from HRTEM images. Ultramicroscopy **107**(12), 1186–93 (2007). doi:10.1016/j.ultramic.2007.01.019
45. Zuo, J.-M., Shah, A.B., Kim, H., Meng, Y., Gao, W., Rouviére, J.-L.: Lattice and strain analysis of atomic resolution Z-contrast images based on template matching. Ultramicroscopy **136**, 50–60 (2014). doi:10.1016/j.ultramic.2013.07.018
46. Hÿtch, M.J., Snoeck, E., Kilaas, R.: Quantitative measurement of displacement and strain fields from HREM micrographs. Ultramicroscopy **74**(3), 131–146 (1998). doi:10.1016/S0304-3991(98)00035-7
47. Huang, P.Y., Kurasch, S., Alden, J.S., Shekhawat, A., Alemi, A.A., McEuen, P.L., Sethna, J.P., Kaiser, U., Muller, D.A.: Imaging atomic rearrangements in two-dimensional silica glass: watching silica's dance. Science **342**(6155), 224–247 (2013)
48. Larsen, P.M., Schmidt, S., Schiøtz, J.: Robust structural identification via polyhedral template matching. Model. Simul. Mater. Sci. Eng. **24**(5), 055007 (2016). doi:10.1088/0965-0393/24/5/055007
49. Van Dyck, D.: Does crystal tilt enhance the electron interaction? Microsc. Microanal. **4**(4), 428–434 (1998). doi:10.1017/S1431927698980412
50. Gonzalez, R.C., Woods, R.E.R.E., Eddins, S.L.: Digital Image Processing Using MATLAB®, 2nd edn. Prentice Hall, New Jersey (2009)

A deep learning approach to identify local structures in atomic-resolution transmission electron microscopy images

Jacob Madsen,[†] Pei Liu,[‡] Jens Kling,[‡] Jakob Birkedal Wagner,[‡] Thomas Willum Hansen,[‡] Ole Winther,[¶] and Jakob Schiøtz[*,†]

[†]*Center for Atomic-scale Materials Design (CAMD), Department of Physics, Technical University of Denmark, 2800 Kgs. Lyngby, Denmark*
[‡]*Center for Electron Nanoscopy (CEN), Technical University of Denmark, 2800 Kgs. Lyngby, Denmark*
[¶]*Department of Applied Mathematics and Computer Science, Technical University of Denmark, 2800 Kgs. Lyngby, Denmark*

E-mail: schiotz@fysik.dtu.dk

Abstract

Recording atomic-resolution transmission electron microscopy (TEM) images is becoming increasingly routine. A new bottleneck is then analyzing this information, which often involves time-consuming manual structural identification. We have developed a deep learning-based algorithm for recognition of the local structure in TEM images, which is stable to microscope parameters and noise. The neural network is trained entirely from simulation, but is capable of making correct predictions on experimental images. We apply the method to single sheets of defected graphene, and to metallic nanoparticles on an oxide support.

Introduction

With the development in transmission electron microscopes that has occurred over the last decade, it has become increasingly common to record and store large amounts of TEM data, often in the form of TEM videos. This development has been accelerated by the advent of faster and more sensitive detectors such as the Direct Detection Camera;[1] but also by the development of the Environmental TEM, where it becomes possible to study how e.g. nanoparticles respond to reaction gasses in real time.[2]

As large amounts of TEM data becomes available, it becomes increasingly important to have efficient and automated analysis tools. In many applications, accurate identification and classification of local structure is a crucial first step in deriving

useful information from atomic-resolution images and video. Examples include characterizing the distribution of dopants[3] and defects,[4] *in situ* imaging of phase transformations,[5] structural reordering during materials growth[6,7] and dynamic surface phenomena.[8]

Analysis methods such as the Geometric Phase Analysis (GPA)[9] are based on the local symmetry and periodicity, and has been very successful at extracting structural information in many regular structures, including identifying defects, strain and phase boundaries.[10] However, GPA typically has difficulties analyzing e.g. surfaces, where the periodicity changes rapidly.[11]

Real space approaches typically either rely on direct identification of atomic positions by fitting local parts of the image to e.g. Gaussian intensity profiles,[12,13] or on direct comparison with a template.[14] However, these methods are in general not able to compete with a trained human expert. The difficulties arise in part due to the phase contrast nature of TEM, which makes the image extremely sensitive to small changes in the defocus, necessitating human intervention in the image analysis. When analyzing time sequences (video), it may even be necessary to adjust the image analysis tools to each frame, as small rotations, vibrations and thermal drift can modify the appearance from one frame to another. These difficulties are compounded by the low signal-to-noise ratio resulting from using the smallest possible electron dose to minimize beam damage to the sample.

Recently, convolutional neural networks and related deep-learning methods have demonstrated excellent performance in visual recognition tasks, including particle detection[15] and automatic segmentation of brain images from cryo-electron microscopy images.[16] Kirschner and Hillebrand have published a method for predicting defocus and sample thickness,[17] and Meyer and Heindl have used neural networks to reconstruct the exit wave function from off-axis electron holograms.[18]

Deep learning methods have, however, to our knowledge not yet been used to analyze the atomic structure in TEM images. In this article, we describe a CNN based method for classifying atomic structures in TEM, and demonstrate that it can be applied to single layers of graphene, as well as to supported metallic nanoparticles. Under good circumstances, the method can be generalized to identify chemical species and to identify the height of atomic columns.

Methods

The task of identifying atoms in atomically resolved TEM images is a special case of a general problem in image analysis. The task is to identify instances of a set of structures, and assigning class labels $\{c_n\}$ and Cartesian coordinates $\{(x_n, y_n)\}$ to each of them. In the simplest case, there is only one class ("atom"), but the analysis can be extended to identify specific structures of atoms; atom columns of various sizes; vacancies; etc. The neural network will be looking for a predefined set of N_c labels, $C = \{c_0, c_1, \ldots, c_{N_c}\}$ and will initially assign a probability for each possible label. The choice of how to categorize the structures is problem specific, and typically depends on how the researcher derives meaning from the image.

An example is shown in Fig. 1, where one or more images of a structure is mapped onto a set of probability maps, from which

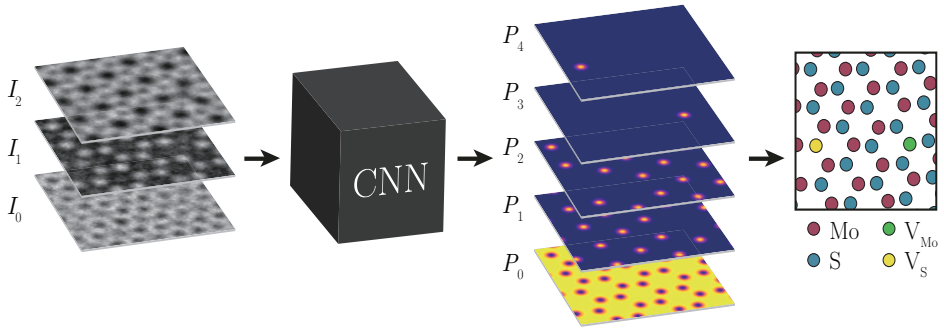

Figure 1: The classification method illustrated on images of single sheets of molybdenum disulphide, MoS_2. The convolutional neural net is fed one or more TEM images of the same sample with varying microscope parameters. The task of the CNN is to classify each pixel as belonging to one of five categories: {background, Mo atom, S atom, Mo vacancy, S vacancy}; where a vacancy is defined as a missing atom where there would be an atom in a perfect lattice. The output of the CNN is thus five probability maps, which are converted into an interpretation of the structure

the interpreted structure can be depicted. The input will typically be a single grey-scale image of size $N_x \times N_y$, but it is possible to use multiple images of the same spatial region, for example a focal series where the microscope focus is varied systematically. Thus in general the neural network maps image data $I_{x,y,k}$ of shape $N_x \times N_y \times N_f$ (where N_f is often 1) to probability maps $P_{x,y,k}$ of shape $N_x \times N_y \times N_c$, where N_c is the number of classes *including a background class*. Including the background class makes it easy to enforce normalization of the probabilities,

$$\forall x, y: \qquad \sum_k P_{x,y,k} = 1. \qquad (1)$$

With such a classification scheme, it is important that structures do not overlap, and overlapping structures should be handled by defining new classes. An example is columns of atoms, which can be handled by making classes for a single atom, a column of two atoms, etc.

Preprocessing

Contrast and illumination may vary significantly across experimentally obtained TEM images, in particular if images contain local structures that are not relevant for the problem being analyzed. This is handled by a combination of subtractive and divisive normalization. First, a local average of the intensity is subtracted from the image

$$G_{ijk} = I_{ijk} - \frac{1}{N_f} \sum_{pqk'} w_{pq} I_{i+p,j+q,k'} \qquad (2)$$

where w_{pq} is a Gaussian weighting window normalized so $\sum_{pq} w_{pq} = 1$. The decay length of the Gaussian weighting window must be chosen to be significantly longer than the length scales of the features the net should detect, to avoid washing them out.

Finally, the contrast is normalized with a divisive normalization using the same Gaussian weighting window

$$H_{ijk} = \frac{G_{ijk}}{\frac{1}{N_f}\sqrt{\sum_{pqk'} w_{pq} G^2_{i+p,j+q,k'}}} \qquad (3)$$

Neural net architecture

The neural network needs to be able to combine information on multiple length scales. Locally, the atoms are identified as local peaks or valleys, but estimating what an atom should look like requires contextual information since it depends on e.g. the defocus of the microscope. In some images the atoms may be bright spots, in other they are dark spots, and the contrast may even invert within different regions of the same image.

The network architecture is based on fully convolutional networks (FCN) for pixel-wise segmentation.[19] Following the FusionNet structure proposed by Quan *et al.*[16] we use additive skips and residual blocks to prevent vanishing gradients and to allow for training of deeper neural nets. Multi-level up-sampling and skip connections combine global abstract information from deep coarse paths with local spatially resolved information from shallow paths.

The network has a single pipeline with additive skip connections to preserve spatial information at each resolution. The lowest resolution is one eighths of the full resolution, this allows for spatial filters to be applied that compare features across the entire image. The shape of the network is chosen to be symmetric, so for every layer present in the part where resolution is reduced, there is a corresponding layer in the part where resolution is increased again. The chosen architecture is shown in Fig. 2

At each resolution on the down-sampling and up-sampling paths, the network consists of five convolutional layers, with a skip connection bypassing the middle three layers using elementwise addition (shown as a *residual block* in Fig. 2). Every convolutional layer except the last employ a 3×3 convolutional kernel, followed by an element-wise rectified linear activation, $h(x) = \max\{0, x\}$, which are then batch normalized following eq. (2–3).[20]

Feature compression is done in the down-sampling path using a max pooling layer down-sampling by a factor two in both spatial direction, while doubling the number of feature maps. Conversely, in the up-sampling path the features are up-sampled using a transpose convolutional block[19] doubling the spatial resolution while halving the number of feature maps, followed by an element-wise addition from same level of the encoding path, forming a long skip connection.

The final scoring consists of a convolutional layer with a 1×1 kernel followed by a softmax non-linearity

$$\sigma(P_k) = \frac{\exp(P_k)}{\sum_{k=1}^{m_f} \exp(P_k)}\,. \qquad (4)$$

The transpose convolutional layers are initialized as bilinear interpolation and all other layers use random weight initialization.

The network is implemented with TensorFlow using the Python API,[21] chosen due to the wide range of functions already made available, as well as the community support. All models are trained and tested with TensorFlow on a single NVIDIA GTX 1080 Ti. Our models and code are publicly available.[22]

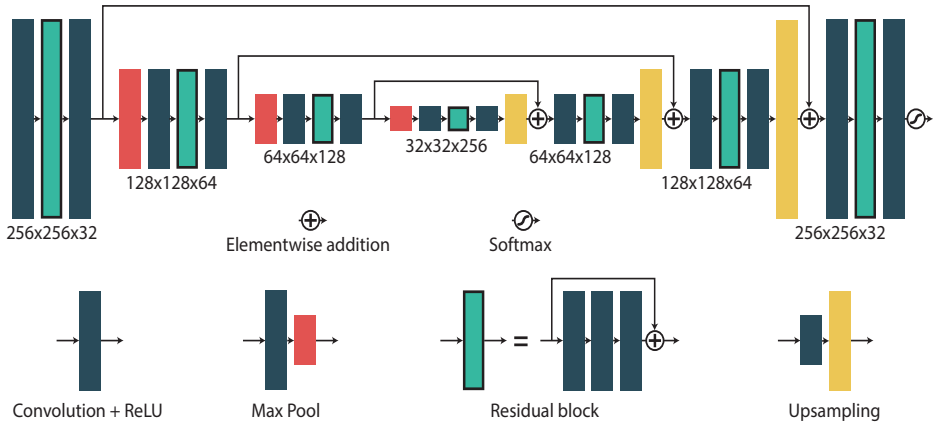

Figure 2: The architecture of the neural network. Information flows from left to right. The features are down-sampled in an encoding path and up-sampled through a decoding path, in addition several skip connections ensure that it is possible to retain fine spatial information.

Generation of training data

A particular challenge is to generate the training data for the neural net, since on one hand these data should include the kind of structures the net should be able to recognize, but on the other hand should not bias the network towards a specific interpretation of the images. This makes it particularly difficult to use real experimental data as training data, since the network would be trained to reproduce any subconscious bias of the scientists generating the interpretations to which the net is trained.

Instead, we train the network to a large set of simulated data. It is important to be aware that this does not preclude biasing the training set, since such a bias will always be present in the selection criteria generating the structures that form the basis for the image simulations, but at least the true positions of all atoms are known for the simulated images.

We try to minimize the bias of the models by generating a training set with a rather large random component while still maintaining realistic atomic positions, but without resorting to e.g. thermodynamical modelling of the systems; this will be discussed further in the sections describing applications of the method.

The training set consists of a collection of computer generated systems (e.g. nanoparticles, if the neural net is to be applied to such), generated using the Atomic Simulation Environment (ASE).[23] Simulated images are generated using the Multislice Algorithm,[24] which has been shown to provide contrast matching with experiment.[25] Simulation is done using the publicly available QSTEM code,[26] through a Python interface to ASE developed by the authors.[11] The exit wave functions for each system in the training set is precomputed, but during training simple symmetry operations (translation, rotation by 90° and mirroring) can easily be applied in each training step.

Table 1: Randomized parameters for generating training examples of graphene for a 80 kV microscope.

parameters	lower bound	upper bound	distribution
defocus (Δf)	-200 Å	200 Å	uniform
3rd order spherical (C_s)	-20 μm	20 μm	uniform
5th order spherical (C_5)	0	5 mm	uniform
1st order astigmatism magnitude	0	100 Å	uniform
1st order astigmatism angle	0	2π	uniform
deflection	0	25 Å	uniform
focal spread	20 Å	40 Å	uniform
dose	10^1 $e^-/\text{Å}^2$	10^4 $e^-/\text{Å}^2$	exponential
c_1 (MTF)	0	0.1	uniform
c_2 (MTF)	0.4	0.6	uniform
c_3 (MTF)	2	3	uniform

For each training iteration, a Contrast Transfer Function (CTF) is generated with randomly chosen parameters for the electron microscope taken from a distribution; Table 1 shows an example of parameters used for graphene. The CTF is then applied to the precomputed exit wave function. The effect of energy spread (i.e. temporal coherence) is included in the quasi-coherent approximation,[27] and temperature effects are included by blurring the atomic potentials. The images are resampled to a random sampling rate, a technique sometimes referred to as *scale-jittering*. It is essential to include a reasonable model of noise in the images, this is done by modelling the finite electron dose with a Poisson distribution, and including the modulation transfer function (MTF) of the detector in the image simulation. The latter is essential as it has a strong influence on the spectral properties of the noise, and prevents that the network incorrectly is trained to detect atoms by the absence of pure white noise. The MTF is modelled a sum of a Gaussian and an exponential:[28]

$$M(q) = c_1 \exp\left(-c_2 q\right) + (1 - c_1) \exp\left(-c_3^2 q^2\right) \tag{5}$$

The ground truth for the training data is generated as a superposition of Gaussians with an amplitude of one, centered at the positions of the atoms (or the mean of the positions for atomic columns). The background class is then assigning the remaining probability, such that the sum of probabilities is one; this is possible since the overlap between any pair of Gaussians is negligible. The width, σ, of the Gaussians is an important parameter, since it strongly influences the penalty of wrongly assigning a region of the inferred confidence map to the background. We found that a too small value of σ would lead to a network with a strong tendency to assign any region that is difficult to analyze (e.g. due to noise) to the background class. In a similar way, we found that a common local minimum at training would be to assign anything to the background class, this is also exacerbated by a low value of σ. We found that a width

of $\sigma = 1$Å, corresponding to 8–10 pixels at typical resolutions, worked well for the cases we have considered.

Training

The CNN is trained using a mean squared difference loss function, regularized with a penalty on the size of the l_2 norm of the weights

$$L = \sum_{ijk} \|\tilde{P}_{ijk} - P_{ijk}\|^2 + \frac{1}{2}\lambda \sum_i W_i^2 \quad (6)$$

where $\tilde{P}$ is the output and P is the ground truth. The main way the network is regularized is through the large variability of the training image data, since a new training image is simulated for every training iteration. Nevertheless, we found that performance on actual experimental data is improved by adding moderate l_2 regularization (also known as weight decay), since this causes any weight not being used by the network to produce meaningful output to become negligible rather than to persist for no reason. Such weights may deteriorate performance on actual experimental data although they do not negatively impact the performance on the training data.

Post-processing and interpretation

While the interpretation of the confidence maps is simplest if there is only a single class, we here illustrate how it can be done even in the case of multiple classes.

The first step is finding the regions where a signal is found. This is done by finding all minima in the confidence map for the background class. Only minima that dip below $\varepsilon = 0.995$ on a scale from 0 – 1 are included, this prevents spending time on analyzing regions that are obviously background. The local minima are then used as seeds for basins created using the watershed principle for image segmentation using Meyer's algorithm.[29] We avoid including long tails in segments by setting a hard upper limit for each segment at ε.

Each segment is then assigned a probability for belonging to each non-background class as

$$p_n(c_k) \propto \sum_{i,j \in \mathcal{S}_n} P_{ijk} \quad k > 0 \quad , \quad (7)$$

where the sum is over all pixels belonging to the n'th image segment. The coordinate of the atomic structure is calculated as the center-of-mass of the image segment. Finally, segments are discarded if

$$\sum_{k>0} p_n(c_k) < t p_n(c_0) \quad (8)$$

The value chosen for t is normally uncritical, but values near 0.5 is recommended. It should be noted that in most cases there is only a single class (c_1), "an atom". The process is illustrated in Fig. 3.

Application to graphene

High resolution TEM has been used extensively to study graphene, and several automatic algorithms for extracting quantitative information have been proposed. Of particular interest is the ability to identify defects, both localized (vacancies, dislocations etc) and extended (grain boundaries).

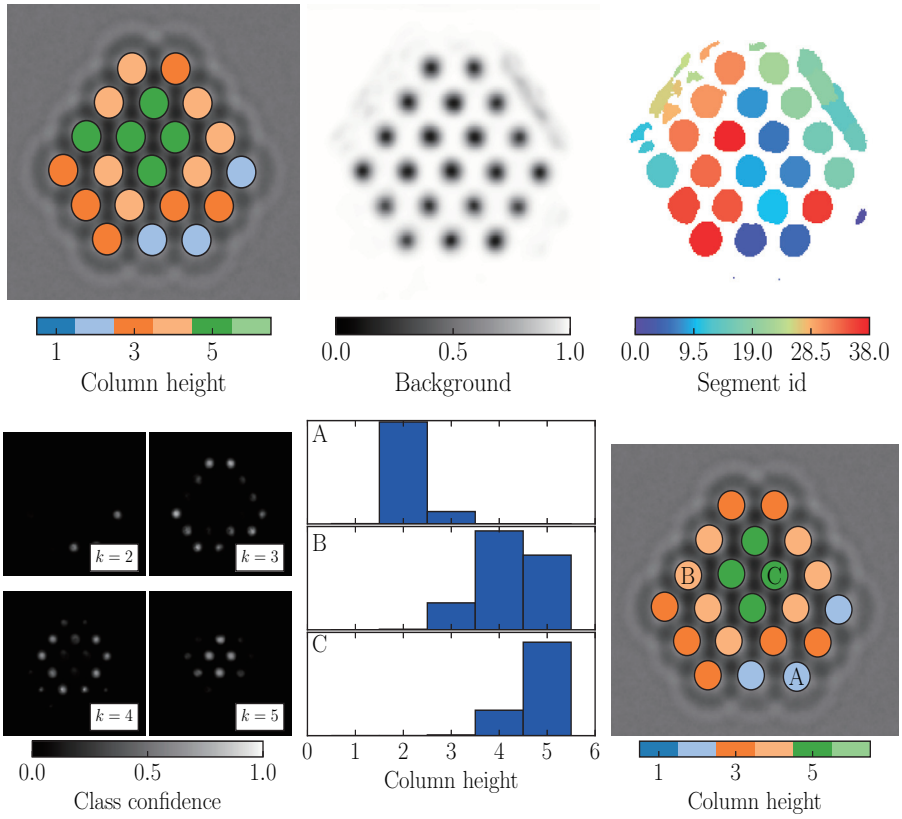

Figure 3: **(a)** The input to the network is three images of a small nanoparticle, recorded (or simulated) with different defocus; here is shown a single simulated image with the ground truth thickness of the individual columns marked with colors. **(b)** The background confidence map; we se that the network correctly identifies that there is something at each atomic column, but also thinks there may be something outside the nanoparticle. **(c)** A segmentation of the background map into several distinct objects. **(d)** Confidence maps for the classes corresponding to columns containing two to five atoms. **(e)** Each object is assigned a probability of belonging to each of the five classes. **(f)** The final classification of the atomic columns. The labels A–C mark the three columns examined in panel (e). In this case, most atomic columns are correctly assigned to their classes. Column B which is has five atoms is incorrectly identified as having only four atoms; however the network is clearly in doubt as seen in the probability distribution. One other column is misassigned, in both cases the network has probably learned that columns at edges and corners are likely to contain fewer atoms, which is not the case for these two columns.

Training

It is an easy task for a CNN to recognize the regular hexagonal lattice of graphene. However, we want the network to be able to correctly localize the atomic positions also in situations where they are not at or near their ideal positions. Thus, the atomic models used to generate the training images cannot simply be ideal sheets of graphene, nor can they be sheets of graphene with added defects.

The opposite extreme, that of generating purely random atomic positions would result in inefficient networks, as the vast majority of the training data would be very different from the experimentally interesting situations. Instead, we generate atomic positions that lie somewhere between these two extremes.

The algorithm is based on the observation that a Voronoi tessellation of a 2D set of points mainly consists of hexagons, and is illustrated in Fig. 4. First, an area is filled with randomly distributed points under the constraint of a minimal distance between the points, i.e. a Poisson disc distribution. These points form the generating centers of a Voronoi tessellation; the vertices of the tessellation will become the carbon atoms. The tessellation is optimized by a few steps of Lloyd's algorithm:[30] the centers of the Voronoi tessellation are moved to the center of mass of their respective Voronoi cell. This makes the Voronoi polyhedra more regular, and in particular it moves closely placed vertices apart, preventing atoms from being placed unrealistically close. Finally, from zero to four holes are cut randomly in the structure.

The resulting structures form a structure which is very suitable for our purpose. The distribution of bond lengths is quite narrow, and the mean can be controlled by choosing the initial number of points. The structure contains a large number of polygons with five to eight sides, similar to what is observed in graphene grain boundaries. A typical training structure is shown in Fig. 5.

We generated 500 random structures with a size of 43.2×43.2 Å, or 360×360 pixels at a sampling rate of 0.12 Å/pixel. All the simulations were done at an acceleration voltage of 80 kV. While the microscope parameters are uniquely generated at each training step, the same structure is utilized multiple times. This have little consequence since most of the variability is in microscope parameters.

Analyzing experimental images

An example of how the network performs on experimental data is given in Fig. 6. When given an experimental TEM image of the edge of a graphene sheet, the neural network has no problems identifying the atoms inside the graphene sheet. At the edge of the sheet, there are positions where the network assigns a small but nonzero probability for the presence of atoms, but using a reasonable cutoff of $t = 0.5$ gives a result in agreement with a manual analysis of the image, and without any high-energy atomic configurations at the edges.

We apply the trained neural net on a number of graphene images that have previously been published by some of us.[31,32] The experimental graphene images were measured using a FEI Titan 80-300 Environmental TEM equipped with a monochromator at the electron gun and spherical aberration (C_s) corrector at the objective lens. The acceleration voltage of the microscope were 80 kV which is

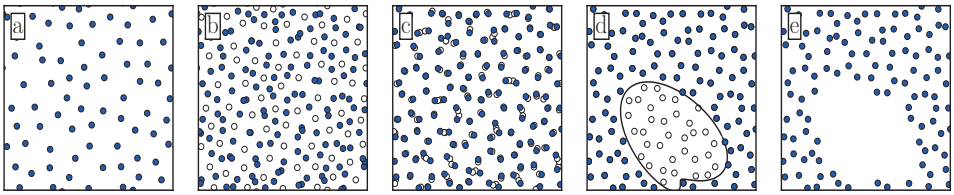

Figure 4: Procedure for generating training structures for graphene. **(a)** A square in 2D space is filled with randomly distributed seed points under the constraint of a minimum separation in terms of euclidean distance. **(b)** Next, the Voronoi tessellation is generated from the seed points, the vertices of the diagram will become atomic positions while the original positions are discarded. **(c)** To avoid overlapping atoms, the positions of the Voronoi vertices are relaxed using Lloyd's algorithm. **(d)** Lastly, zero to four holes of varying size and shape are introduced in the structure.

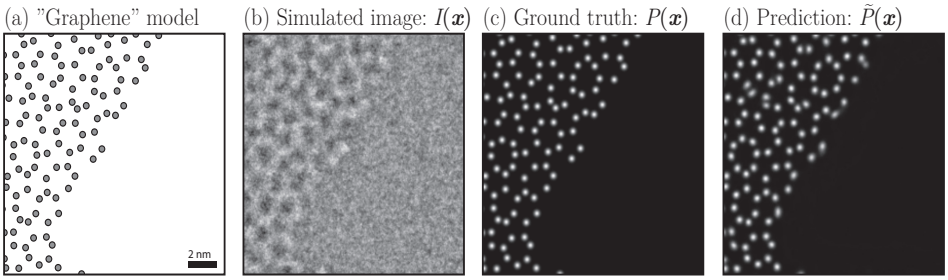

Figure 5: The CNN is trained on simulated images of graphene-like structures, generated by the algorithm in Fig. 4. **(a)** A quasi-random graphene-like structure. **(b)** Simulated image based on the atomic positions. **(c)** The corresponding ground truth calculated from the atomic positions. The network is trained on a series of matching images and ground truth maps. **(d)** The output prediction of the trained neural network given the simulated image in (b).

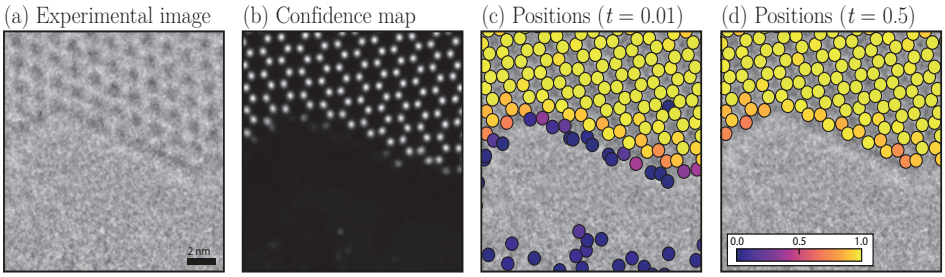

Figure 6: A neural network trained exclusively on simulated data is capable of generalizing to experimental images. **(a)** Single suspended graphene sheet with a hole formed under the influence of the electron beam. **(b)** The regressed probability distribution predicted by the neural network for the image in (a). **(c)** The local peak positions of the probability map is overlayed on the image. The peaks are color-coded according to their maximum value. Peaks with a maximum value less than 0.01 are excluded. (**d**) A higher tolerance for exclusion is used to remove peaks with a maximum value less than 0.5.

below the knock-on threshold for carbon atoms in pristine graphene.[33] The electron beam energy spread was below 0.3 eV, while the C_s-corrector was aligned to minimize the spherical aberration. The images were recorded using a Gatan US1000 CCD camera with an exposure time of 1 s.

Fig. 7 shows a TEM images of pristine graphene, and of graphene with a hole. The negative C_s imaging results in images where the carbon atoms are bright spots, with the centers of the hexagons appearing dark. The output of the neural network is shown in the central column. The neural network detects all atomic positions in the pristine sheet, this is accomplished without having regular hexagonal lattices in the training set. Additionally, the neural network automatically recognizes that the atoms appear bright, which is only the case for half of the training images. Finally, we show the strain calculated from the atomic positions, using a structural template with the two nearest neighbour shells (i.e. the 9 nearest neighbours), as described previously.[11]

Application to metallic nanoparticles

Metallic nanoparticles on oxide support is a very active research topic, mainly due to the applications within heterogeneous catalysis. Often, the detailed atomic structure is important for the catalytic process, as the active size depending on the process may be e.g. step sites,[34] corner atoms[35] or strained facets.[36,37]

For example, although gold is normally chemically inert, nanoparticles of gold have been shown to catalyse the oxidation of CO.[38] It is also a system where significant atomic rearrangement is observed in the presence of gasses, both involving overall shape changes of the nanoparticles[39] and changes in the local surface structure We here use supported gold nanoparticles to illustrate the application of neural nets to the analysis of supported nanoparticles.

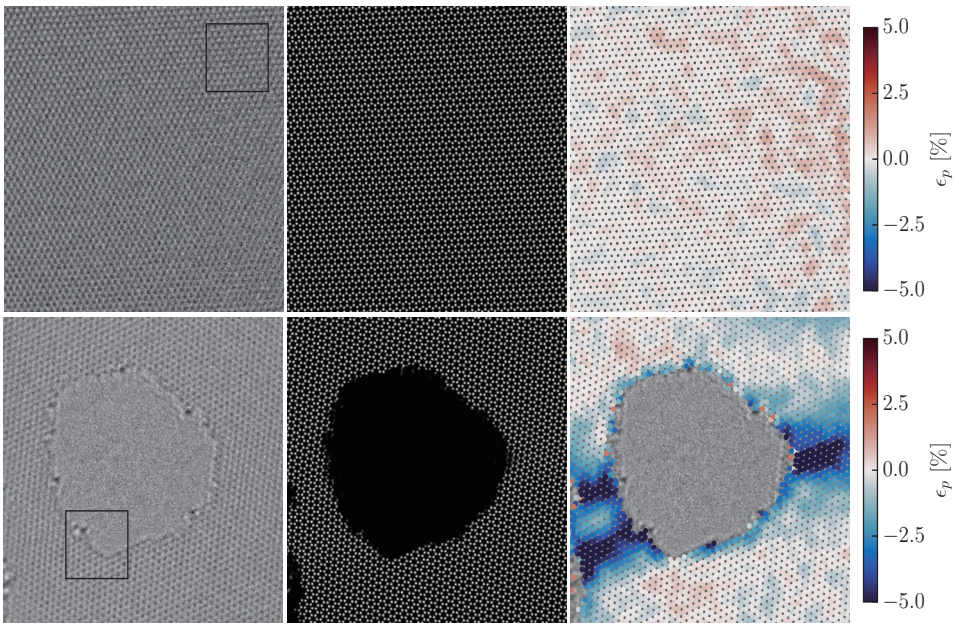

Figure 7: Experimental images of graphene, and their interpretation by the neural net. The first row shows a pristine sheet of graphene, the second a sheet with a hole. The left column shows the original TEM images. The center column shows the output of the neural net. The rightmost column shows the planar strain calculated from the atomic positions, as identified by the neural net.

Training

We have trained the network on simulated gold nanoparticles. As the network should be able to recognize both atomically flat and rough surfaces, the training set includes both kinds of nanoparticles. Initially, nanoparticles are cut from a regular crystal, keeping a random number of layers in directions with low Miller indices (the $\langle 100 \rangle$, $\langle 110 \rangle$ and $\langle 111 \rangle$ directions). To roughen the particles, a random number of additional atoms are added to the particle. The atoms are added at allowed crystal positions at the surface of the nanoparticles, in such a way that highly coordinated surface sites are most likely to be picked. If the coordination number (i.e. the number of occupied neighbor sites) of site i is n_i, then the probability of placing the next atom at site i is chosen as

$$p(n_i) = \frac{\exp(n_i/T)}{\sum_j \exp(n_j/T)} \qquad (9)$$

where the sum is over all sites j where $n_j \geq 1$ and T is a temperature-like parameter that can be chosen differently for each nanoparticle to generate particles with different roughness.

Each particle is then rotated into the $\langle 110 \rangle$ or $\langle 111 \rangle$ zone axis, and is rotated a random amount around the axis. It is finally tilted 0–5° away from the zone axis.

As was the case for the graphene simulations, 500 of nanoparticles were generated, but during the training new microscope parameters were picked for each iteration, and the nanoparticles were randomly translated, mirrored and rotated by a multiple of 90° (operations that can cheaply be performed on the precomputed wavefunctions). Figure 8 shows a sample of generated nanoparticles, and their corresponding images.

Analyzing nanoparticle images and videos

We applied the resulting network to gold nanoparticles on a ceria substrate. Figure 9 shows a TEM image of such a particle, and the corresponding analysis by the neural net. It is seen that the network confidently identifies the atoms in the nanoparticle, but does a much less impressive job in the substrate; this is partly due to the network not being trained on ceria's crystal structure, partly because the substrate is not in a prominent zone-axis orientation.

In the microscope, a video sequence of this nanoparticle was recorded, Fig. 9 shows four snapshots of this video, clearly showing the atomic diffusion processes.

We used the neural network to analyze TEM movies showing surface diffusion on gold nanoparticle in various gasses. Figure 10 shows the same ceria-supported gold nanoparticle in high vacuum and in an oxygen atmosphere. The neural network is applied to each frame in the video sequence, and used to identify the presence (and position) of the atomic columns. Since the network was not trained on substrates, and since atomic resolution is often not obtainable simultaneously in the substrate and the nanoparticle, we only use the network to analyze the metallic nanoparticle and mask out the output of the network corresponding to the substrate.

During the video sequence, atoms at the surfaces and in particular at the corners of the nanoparticle are clearly seen to appear and disappear again, as the surface atoms diffuse on the particle. We illustrate this in the figure in two different ways. In the middle column, atomic columns are colored according to the fraction of time they are present in the image. It is clearly seen that in the presence of oxygen, many of the surface and corner atoms are only present part of the time, indicating surface diffusion. In the rightmost columns, "events" are counted. It is considered an "event" if an atomic column is present in one frame, but absent in the next, or *vice versa*; this cause the diffusing atoms to light up on the figure. Together, this analysis shows that the presence of oxygen clearly enhances the surface diffusion. This will be the topic of a separate publication.

Other applications

We envision that the main application of this technique will be to identify atoms or columns of atoms, as demonstrated in the two afore-mentioned examples. For this kind of applications, it is relatively straight-forward to train a neural net on sets of simulated images, such that the net becomes able to identify the positions of the atoms or atomic columns also in experimentally obtained images.

A far more demanding task is to identify the chemical species of single atoms in 2D materials, or to count the number of atoms in atomic columns in nanoparticles. It does

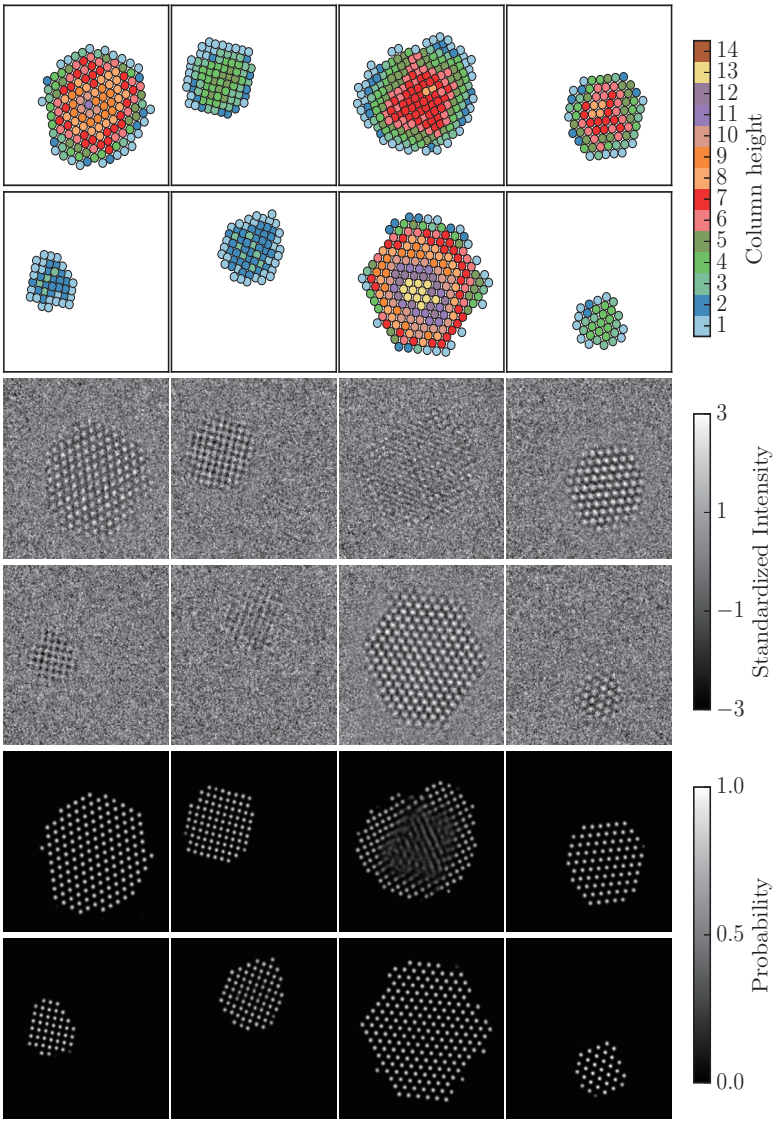

Figure 8: **Top rows:** Examples of nanoparticles generated using the algorithm we have proposed. The height of the atomic columns of the nanoparticles are indicated with a color-coding. **Middle rows:** Simulated images given the atomic models above. **Bottom rows:** Output from our neural network method given the simulated images. As can be seen, in one of the images the network is not able to identify the atomic columns in the thickest part of the nanoparticle, this is due to a combination of low signal-to-noise ratio in the image, and a significant off-axis tilt smearing out the highest atomic columns.

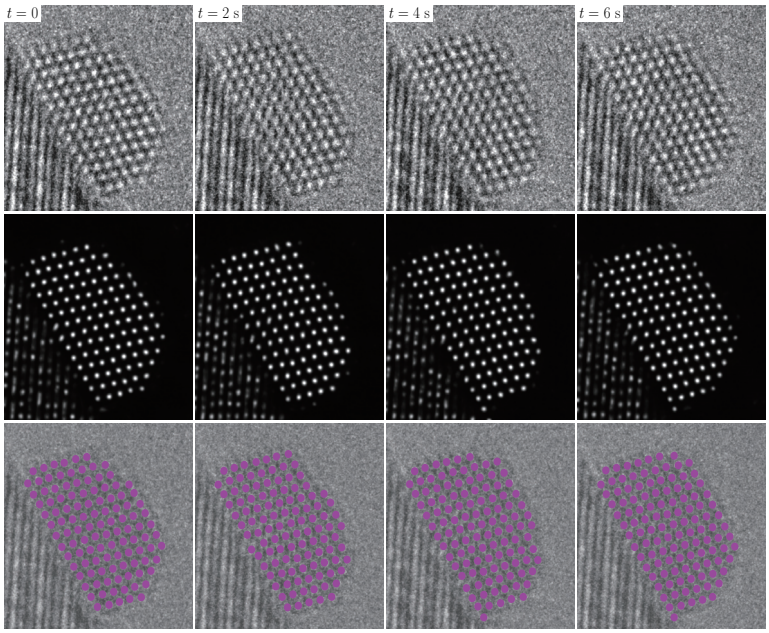

Figure 9: **top row:** Experimental high resolution TEM image of gold on ceria in an oxygen atmosphere. The pressure was 4.5 Pa and the electron dose per image was 3.1×10^2 e$^-$/Å^2 (dose rate 1.56×10^3 e$^-$/Å^2/s at an exposure time of 0.2 s). **Middle row:** Output from the neural network given the images above. **Bottom row:** The atoms identified by the neural net are marked as purple circles overlaid on the original image. The experimental images were measured using a FEI Titan 80-300 Environmental TEM operated at 300 keV.

not appear to be possible to train a network that solves this kind of tasks based on a single image. However, if one is willing to use a series of images taken with varying focus settings, it appears to be possible to train such networks to identify multiple mutually exclusive atomic objects. The reliability does, however, not seem to be on par with the reliability of identifying a single atom or column. Figures from our attempts to build these more advanced networks have been used to illustrate the general principles (Figures 1 and 3). Since we have not yet been able to demonstrate the useful of such networks on experimental images, we will defer further discussions on the subject to future publications.

Conclusion

We have demonstrated that deep convolutional neural networks can be trained to recognize the local atomic structure in High Resolution Transmission Electron Microscopy images. The network can be trained entirely on simulated data, but is capable of giving interpretations of experimental images that match those of a trained microscopist. We have demonstrated the method both on single layers

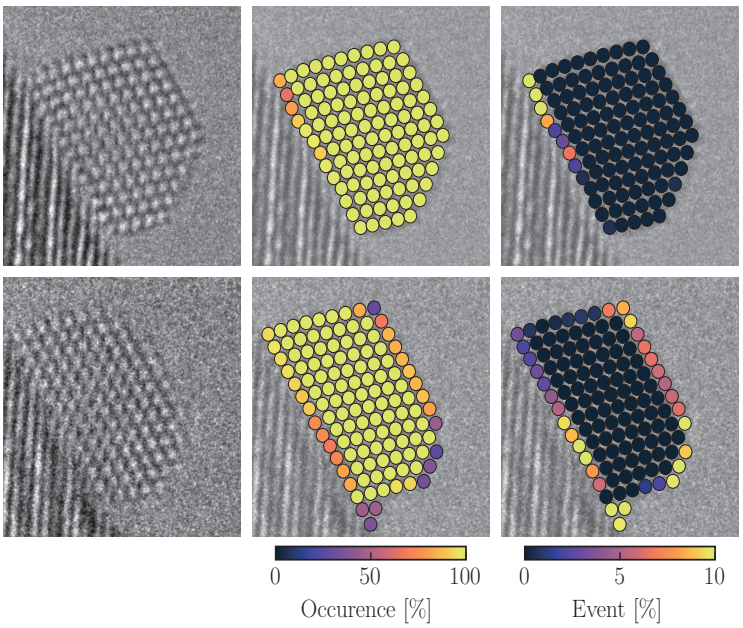

Figure 10: The surface dynamics of gold nanoparticles is influenced by the gaseous atmosphere. The occurence is the percentage of frames where the neural network identified an atomic column at a possible site. And the events are the percentage of frames where a site was previously occupied, but is unoccupied in the frame immediately after.

of defected graphene, and on nanoparticles of gold on a cerium oxide substrate.

References

(1) McMullan, G.; Faruqi, A. R.; Clare, D.; Henderson, R. *Ultramicroscopy* **2014**, *147*, 156–163.

(2) Wagner, J. B.; Cavalca, F.; Damsgaard, C. D.; Duchstein, L. D. L.; Hansen, T. W. *Micron* **2012**, *43*, 1169–1175.

(3) Meyer, J. C.; Kurasch, S.; Park, H. J.; Skakalova, V.; Künzel, D.; Gross, A.; Chuvilin, A.; Algara-Siller, G.; Roth, S.; Iwasaki, T.; Starke, U.; Smet, J. H.; Kaiser, U. *Nat. Mater.* **2011**, *10*, 209–215.

(4) Meyer, J. C.; Kisielowski, C.; Erni, R.; Rossell, M. D.; Crommie, M. F.; Zettl, A. *Nano Lett.* **2008**, *8*, 3582–3586.

(5) He, X.; Xu, T.; Xu, X.; Zeng, Y.; Xu, J.; Sun, L.; Wang, C.; Xing, H.; Wu, B.; Lu, A.; Liu, D.; Chen, X.; Chu, J. *Nature Publishing Group* **2014**, *4*, 6544.

(6) Nagao, K.; Inuzuka, T.; Nishimoto, K.; Edagawa, K. *Phys. Rev. Lett.* **2015**, *115*, 075501.

(7) Li, X.; Cheng, S.; Deng, S.; Wei, X.; Zhu, J.; Chen, Q. *Nature Publishing Group* **2017**, *7*, 40911.

(8) Schneider, S.; Surrey, A.; Pohl, D.; Schultz, L.; Rellinghaus, B. *Micron* **2014**, *63*, 52–56.

(9) Hÿtch, M. J.; Snoeck, E.; Kilaas, R. *Ultramicroscopy* **1998**, *74*, 131–146.

(10) Zhu, Y.; Ophus, C.; Ciston, J.; Wang, H. *Acta Mater.* **2013**, *61*, 5646–5663.

(11) Madsen, J.; Liu, P.; Wagner, J. B.; Hansen, T. W.; Schiøtz, J. *Adv. Struct. Chem. Imag.* **2017**, 1–12.

(12) Bierwolf, R.; Hohenstein, M.; Phillipp, F.; Brandt, O.; Crook, G. E.; Ploog, K. *Ultramicroscopy* **1993**, *49*, 273–285.

(13) Galindo, P. L.; Kret, S.; Sanchez, A. M.; Laval, J.-Y.; Yáñez, A.; Pizarro, J.; Guerrero, E.; Ben, T.; Molina, S. I. *Ultramicroscopy* **2007**, *107*, 1186–1193.

(14) Zuo, J.-M.; Shah, A. B.; Kim, H.; Meng, Y.; Gao, W.; Rouviére, J.-L. *Ultramicroscopy* **2014**, *136*, 50–60.

(15) Zhu, Y.; Ouyang, Q.; Mao, Y. *BMC Bioinformatics* **2017**, *18*, 348.

(16) Quan, T. M.; Hildebrand, D. G. C.; Jeong, W.-K. *arXiv* **2016**, 1612.05360.

(17) Kirschner, H.; Hillebrand, R. *Information Sciences* **2000**, *129*, 31–44.

(18) Meyer,; Heindl, *J. Microsc.* **2008**, *191*, 52–59.

(19) Shelhamer, E.; Long, J.; Darrell, T. *IEEE Trans Pattern Anal Mach Intell* **2017**, *39*, 640–651.

(20) Ioffe, S.; Szegedy, C. *arXiv* **2015**, 1502.03167.

(21) Abadi, M. et al. TensorFlow: A System for Large-Scale Machine Learning. Proceedings of the 12th USENIX Symposium on Operating Systems Design and Implementation (OSDI '16). 2016.

(22) https://github.com/jacobjma.

(23) Hjorth Larsen, A. et al. *J Phys Condens Matter* **2017**, *29*, 273002.

(24) Goodman, P.; Moodie, A. F. *Acta Crystallographica Section A: Crystal Physics* **1974**, *30*, 280–290.

(25) Thust, A. *Phys. Rev. Lett.* **2009**, *102*, 220801.

(26) Koch, C. Determination of core structure periodicity and point defect density along dislocations. Ph.D. thesis, Arizona State University, 2002.

(27) Kirkland, E. J. *Advanced Computing in Electron Microscopy*, 2nd ed.; Springer US: 978-1-4419-6532-5, 2010.

(28) Van den Broek, W.; Van Aert, S.; Van Dyck, D. *Microsc. Microanal.* **2012**, *18*, 336–342.

(29) Dougherty, E. R. *Mathematical morphology in image processing*; M. Dekker, 1993.

(30) Lloyd, S. P. *Ieee Transactions on Information Theory* **1982**, *28*, 129–137.

(31) Vestergaard, J. S.; Kling, J.; Dahl, A. B.; Hansen, T. W.; Wagner, J. B.; Larsen, R. *Microsc. Microanal.* **2014**, *20*, 1772–1781.

(32) Kling, J.; Vestergaard, J. S.; Dahl, A. B.; Stenger, N.; Booth, T. J.; Bøggild, P.; Larsen, R.; Wagner, J. B.; Hansen, T. W. *Carbon* **2014**, *74*, 363–366.

(33) Zobelli, A.; Gloter, A.; Ewels, C. P.; Seifert, G.; Colliex, C. *Phys. Rev. B* **2007**, *75*, 245402.

(34) Honkala, K.; Hellman, A.; Remediakis, I. N.; Logadottir, A.; Carlsson, A.; Dahl, S.; Christensen, C. H.; Norskov, J. K. *Science* **2005**, *307*, 555–558.

(35) Brodersen, S. H.; Grønbjerg, U.; Hvolbæk, B.; Schiøtz, J. *J Catal* **2011**, *284*, 34–41.

(36) Stephens, I. E. L.; Bondarenko, A. S.; Grønbjerg, U.; Rossmeisl, J.; Chorkendorff, I. *Energy Environ. Sci.* **2012**, *5*, 6744.

(37) Escudero-Escribano, M.; Malacrida, P.; Hansen, M. H.; Vej-Hansen, U. G.; Velazquez-Palenzuela, A.; Tripkovic, V.; Schiøtz, J.; Rossmeisl, J.; Stephens, I. E. L.; Chorkendorff, I. *Science* **2016**, *352*, 73–76.

(38) Haruta, M.; Kobayashi, T.; Sano, H.; Yamada, N. *Chemistry Letters* **1987**, *16*, 405–408.

(39) Uchiyama, T.; Yoshida, H.; Kuwauchi, Y.; Ichikawa, S.; Shimada, S.; Haruta, M.; Takeda, S. *Angew. Chem. Int. Ed. Engl.* **2011**, *50*, 10157–10160.